

Mid- and far-infrared properties of Spitzer Galactic bubbles revealed by the AKARI all-sky surveys

Yasuki HATTORI^{1,*}, Hidehiro KANEDA^{1,*}, Daisuke ISHIHARA¹, Yasuo FUKUI¹,
Kazufumi TORII¹, Misaki HANAOKA¹, Takuma KOKUSHO¹, Akino KONDO¹,
Kazuyuki SHICHI¹, Sota UKAI¹, Mitsuyoshi YAMAGISHI¹ and Yuta
YAMAGUCHI¹

¹Graduate School of Science, Nagoya University, Furo-cho, Chikusa-ku, Nagoya 464-8602,
Japan

*E-mail: hattori@u.phys.nagoya-u.ac.jp, kaneda@u.phys.nagoya-u.ac.jp

Received ; Accepted

Abstract

We have carried out a statistical study on the mid- and far-infrared (IR) properties of Galactic IR bubbles observed by Spitzer. Using the Spitzer 8 μm images, we estimated the radii and covering fractions of their shells, and categorized them into closed, broken and unclassified bubbles with our data analysis method. Then, using the AKARI all-sky images at wavelengths of 9, 18, 65, 90, 140 and 160 μm , we obtained the spatial distributions and the luminosities of polycyclic aromatic hydrocarbon (PAH), warm and cold dust components by decomposing 6-band spectral energy distributions with model fitting. As a result, 180 sample bubbles show a wide range of the total IR luminosities corresponding to the bolometric luminosities of a single B-type star to many O-type stars. For all the bubbles, we investigated relationships between the radius, luminosities and luminosity ratios, and found that there are overall similarities in the IR properties among the bubbles regardless of their morphological types. In particular, they follow a power-law relation with an index of ~ 3 between the total IR luminosity and radius, as expected from the conventional picture of the Strömgren sphere. The exceptions are large broken bubbles; they indicate higher total IR luminosities, lower fractional luminosities of the PAH

emission, and dust heating sources located nearer to the shells. We discuss the implications of those differences for a massive star-formation scenario.

Key words: infrared: ISM — ISM: bubbles — stars: massive — stars: formation

1 Introduction

Galactic infrared (IR) bubbles were first detected and cataloged in Churchwell et al. (2006) and (2007), using the $8\ \mu\text{m}$ band images of the Galactic Legacy Infrared Mid-plane Survey Extraordinaire (GLIMPSE; Benjamin et al. 2003) program with the Spitzer satellite (Werner et al. 2004). The IR bubbles are observed toward the Galactic plane, which show shell or broken shell structures in the $8\ \mu\text{m}$ images. In this catalogue, difference in the morphology of the bubbles was distinguished by visual classification. Closed bubbles have well-defined shell structures in the $8\ \mu\text{m}$ images, while broken bubbles have incomplete shell structures, which do not cover the whole direction. Figure 1 shows examples of the cataloged bubbles. The $8\ \mu\text{m}$ band intensity is dominated by the emission of polycyclic aromatic hydrocarbons (PAHs), which are mainly distributed in photodissociation regions (PDRs).

Deharveng et al. (2010) investigated 102 Galactic IR bubbles, using radio-continuum observational data by the Multi-Array Galactic Plane Imaging Survey (MAGPIS; Helfand et al. 2006) at 20 cm and the VLA Galactic Plane Survey (VGPS; Stil et al. 2006) at 21 cm. They examined spatial correlation between the Spitzer $8\ \mu\text{m}$ and radio continuum data, which trace PAH shells and HII regions, respectively, and found that 86% of the bubbles enclose HII regions. They also found that 98% of the sample show the $24\ \mu\text{m}$ emission associated with the shells, which traces warm dust. These facts strongly suggest that most of the Galactic IR bubbles contain massive young stars which heat the interstellar medium (ISM) such as PAH, dust grains and gas by strong ultraviolet (UV) radiation.

Massive stars severely affect the ambient ISM. Intense UV radiation changes ISM conditions through photo-ionization of gas, photo-dissociation of molecules, and heating and photo-evaporation of dust grains. Although a lot of studies on interaction between massive stars and ambient ISM have been carried out, the formation process of a massive star itself is not well understood. One of the biggest problems in massive star formation is radiation feedback of a central star to accreting matters. Wolfire & Cassinelli (1987) calculated the relation between the mass and the mass accretion rate of a massive star and concluded that a massive star is difficult to be formed with the accretion rate of $\sim 10^{-5}\ M_{\odot}\ \text{yr}^{-1}$, which is a typical value expected from the isothermal collapse of a gaseous sphere

(Stahler et al. 1980), because of intense radiation pressure. Therefore very efficient mass accretion is indispensable to form massive stars.

Elmegreen (1998) suggested three major processes for massive star formation, which are “globule squeezing”, “collect and collapse” and “cloud-cloud collision”. All the processes create dense molecular cores through gas compression and trigger massive star formation as a result of the self-gravitational collapses of the cores. Deharveng et al. (2010) suggested the observational evidence for the “globule squeezing” process by investigating spatial correlation between the pre-existing dust condensations observed by the APEX Telescope Large Area Survey of the Galactic plane (ATLASGAL; Schuller et al. 2009) at $870\ \mu\text{m}$ and the ionization front of HII regions traced by the Spitzer 8 and $24\ \mu\text{m}$ images of Galactic IR bubbles. They found that 28% of 65 spatially resolved bubbles include dust condensations associated with bright rims, which indicates the compression of pre-existing dense gas by the expanding HII regions. They also showed that other 40% of the spatially resolved bubbles are surrounded by cold dust emission, which implies that these bubbles are candidates of massive star-forming regions triggered by the “collect and collapse” process. Ishihara et al. (2007) studied IC4954 and IC4955 using the AKARI mid- and far-IR data, and found that young stellar objects are located on the $9\ \mu\text{m}$ emission arc created by the central source indicating star formation in the ambient ISM compressed by the central source. This is also observational evidence for “collect and collapse”.

Observational evidence for “cloud-cloud collision” was first reported by Loren (1976) using the velocity information of two clouds in NGC1333. Habe & Ohta (1992) carried out the simulation of head-on collisions and suggested that collision between two molecular clouds generates strong bow shocks which compress parental molecular clouds and create gravitationally unstable cores. Massive stars can be formed by self-gravitational collapse of the compressed unstable cores (e.g., Takahira et al. 2014). Recent observations of Galactic massive star-forming regions such as RCW49, Westerlund2, M20, NGC3603 and RCW120 with the NANTEN/NANTEN2 radio telescopes indicated several pieces of observational evidence for the “cloud-cloud collision” scenario (Furukawa et al. 2009; Ohama et al. 2010; Torii et al. 2011; Fukui et al. 2014; Torii et al. 2015). They found that two molecular clouds possessing different radial velocities are associated with the star-forming regions; large velocity difference (about $15\ \text{km s}^{-1}$) between two clouds indicates that the clouds cannot be bound gravitationally by the observed cloud masses. These facts suggest a possibility that the massive star formation in these regions may have been triggered by cloud-cloud collisions. Thus a lot of studies for the “cloud-cloud collision” process have been carried out, emphasizing the importance of the process in massive star formation. It is notable that the resultant structure of the colliding clouds is similar to the structure of the Galactic IR bubbles, especially for the broken bubbles.

Mid- and far-IR observations of massive star-forming regions are essential to obtain information on PAHs and dust grains, which surround exciting sources. PAH emission traces the morphology of the surfaces of PDRs which are located on the borders of HII regions and molecular clouds. Warm dust emission with a typical temperature of about 60 K traces the morphology of HII regions, while cold dust emission with a typical temperature of about 20 K traces that of cold gas regions. Therefore, using these IR dust emissions, we can investigate the complicated geometry of HII regions and PDRs in star-forming regions with respect to the positions of massive stars, revealing the interaction of each component. In addition, and more importantly, we can estimate the total energy of exciting sources from the total IR dust emission because these embedded dust components receive a dominant fraction of UV photons from young massive stars and re-radiate the absorbed energy at mid- and far-IR wavelengths. Hence IR observations provide many pieces of information on the Galactic IR bubbles; nevertheless, a systematic study using both mid- and far-IR data has not been carried out yet.

In this paper, we investigate the mid- and far-IR properties of the Spitzer Galactic IR bubbles using the AKARI all-sky survey data. The AKARI all-sky surveys cover a wide IR wavelength range with the 6 photometric bands at wavelengths of 9, 18, 65, 90, 140 and 160 μm so that we can estimate the total IR flux of each bubble. We obtained the central position and the radius of each bubble by fitting a circle to its image. We also estimated the covering fractions of bubbles on the basis of our quantitative criteria to classify them into closed and broken bubbles. We created a local spectral energy distribution (SED) from the 6 photometric bands with a 15'' spatial grid and fitted the SED by the model consisting of PAHs, warm dust and cold dust components. Then for each dust component, we created a distribution map with a 15'' grid.

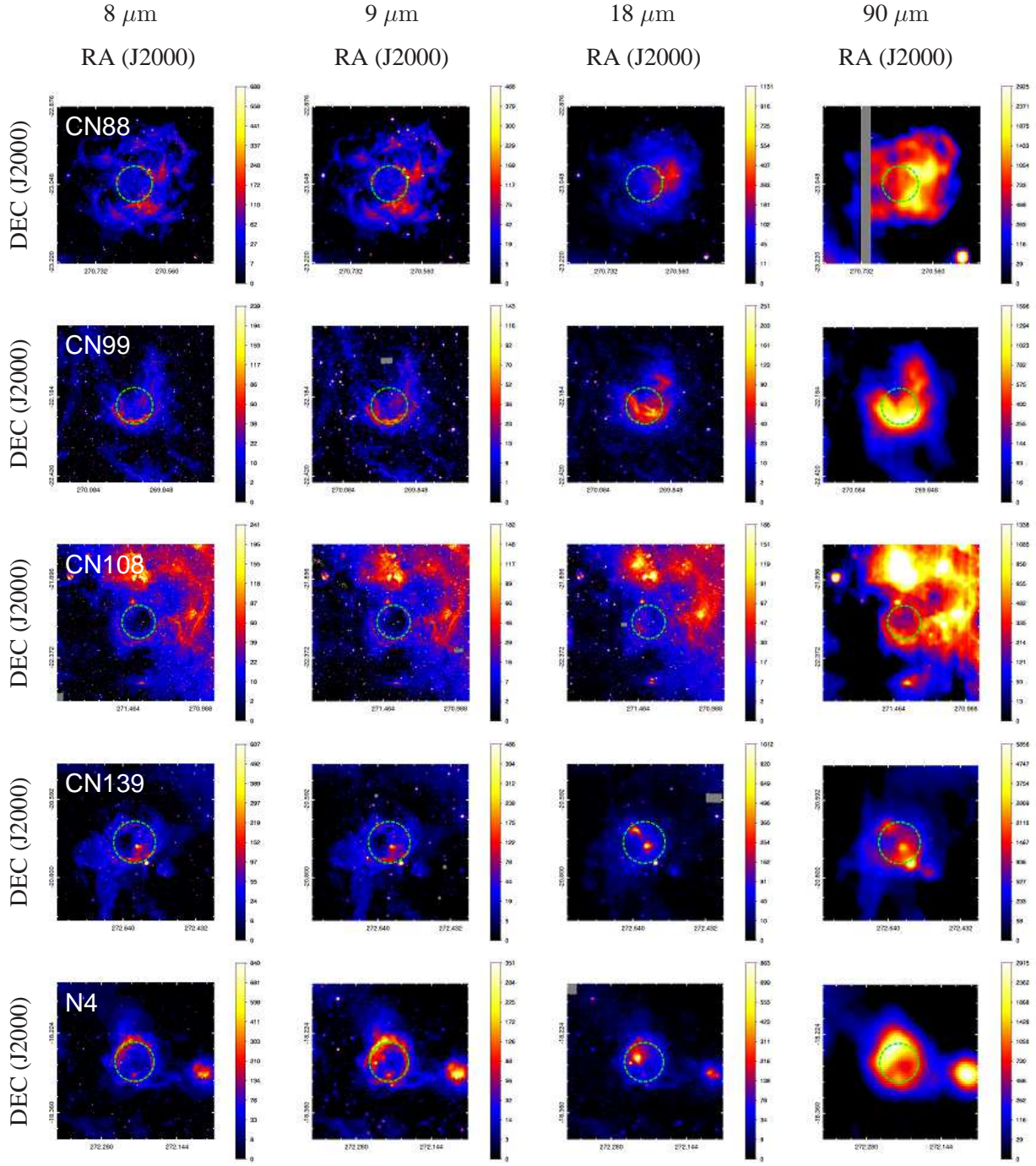


Fig. 1. Examples of the Spitzer 8 μm band and the AKARI 9, 18 and 90 μm band images of the Spitzer Galactic IR bubbles cataloged in Churchwell et al. (2006) and (2007). For each row, the name of the bubble is given in the left panel, and the 8, 9, 18 and 90 μm images are arrayed from left to right. The green dashed circles are drawn with the central positions and radii of the bubbles given in Churchwell et al. (2006) and (2007). The color levels are given in units of MJy sr^{-1} . The angular size of each panel is $4R \times 4R$, where R is the bubble radius estimated with our circular fitting (see section 2).

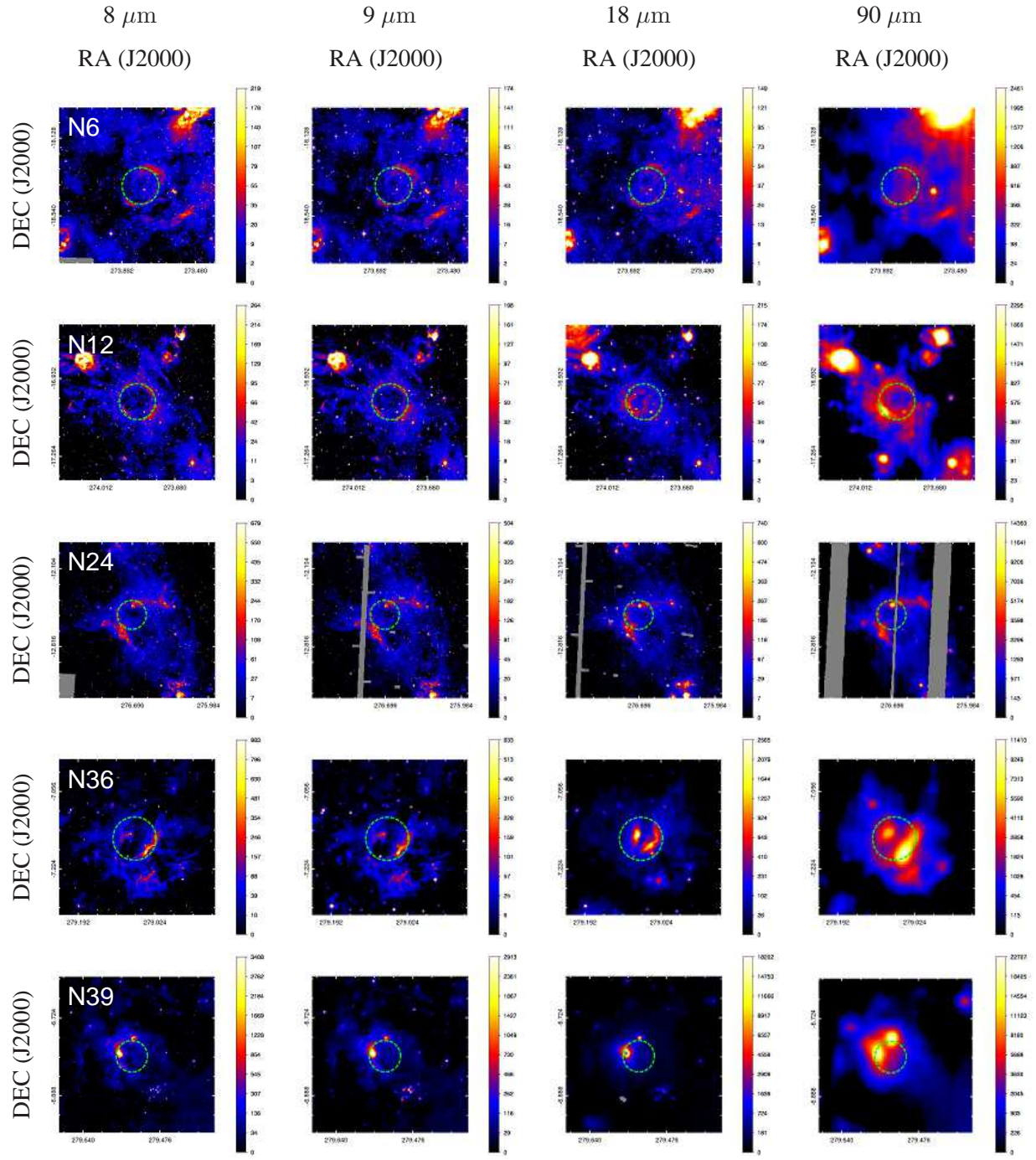


Fig. 1. Continued.

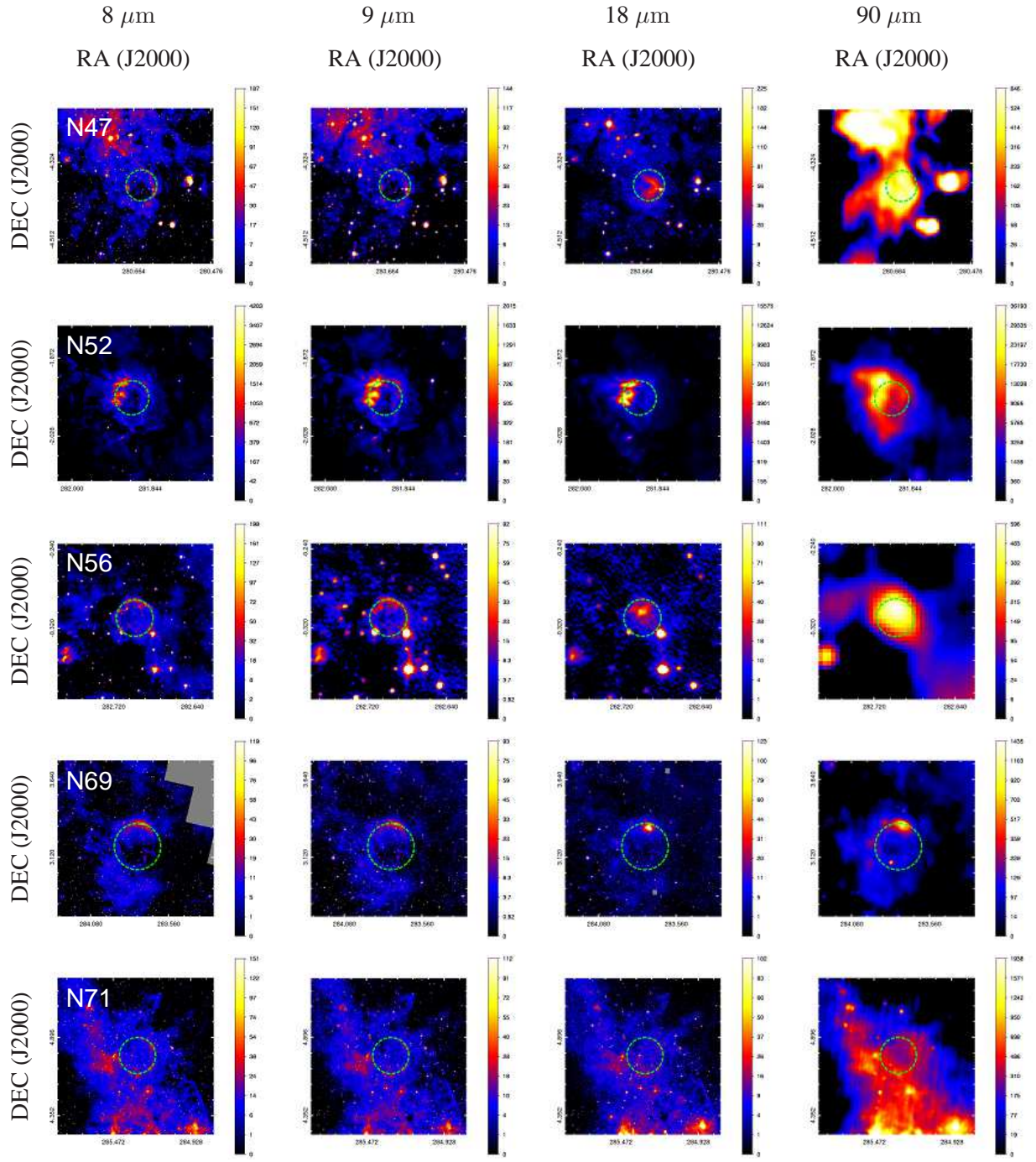


Fig. 1. Continued.

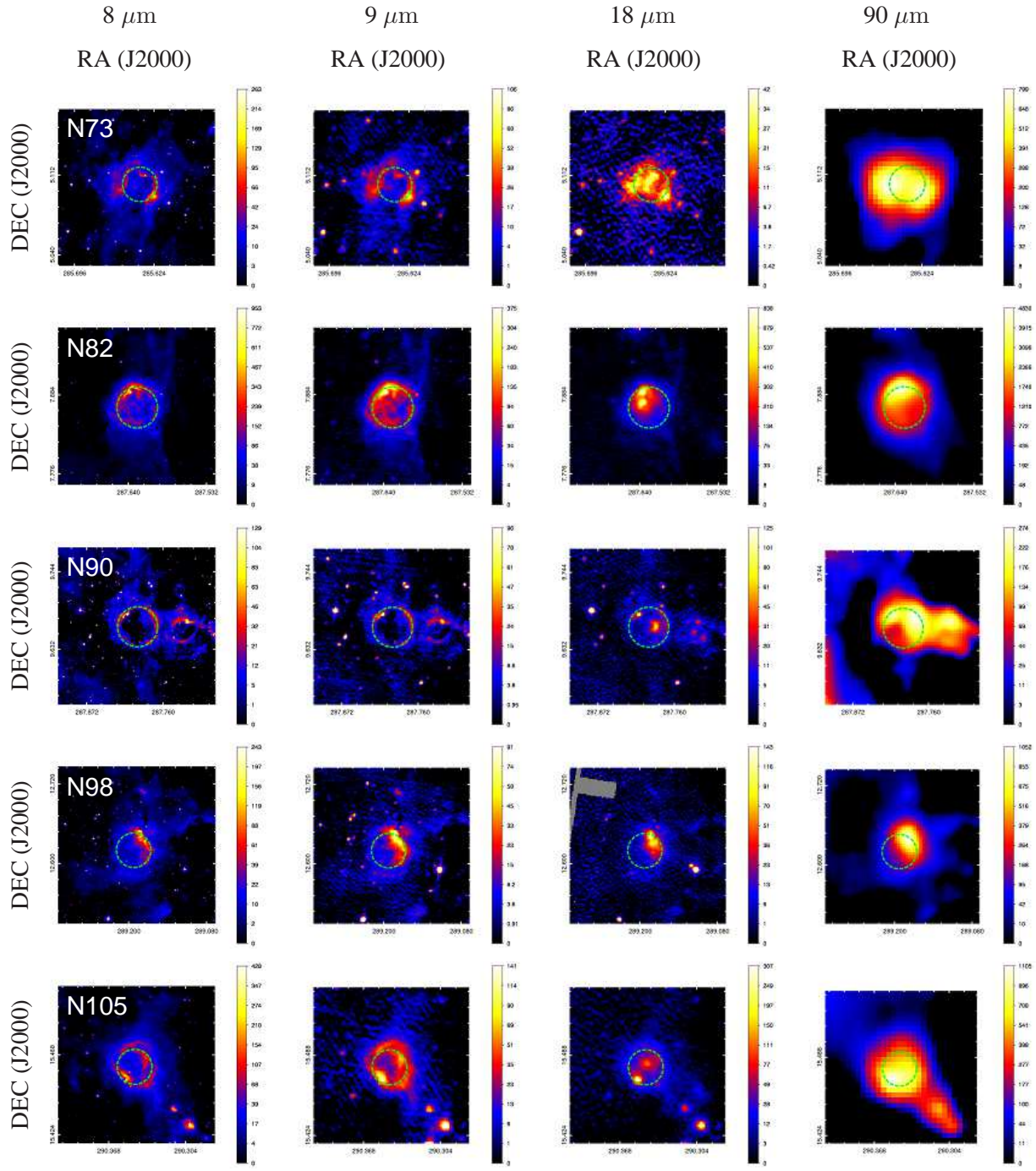


Fig. 1. Continued.

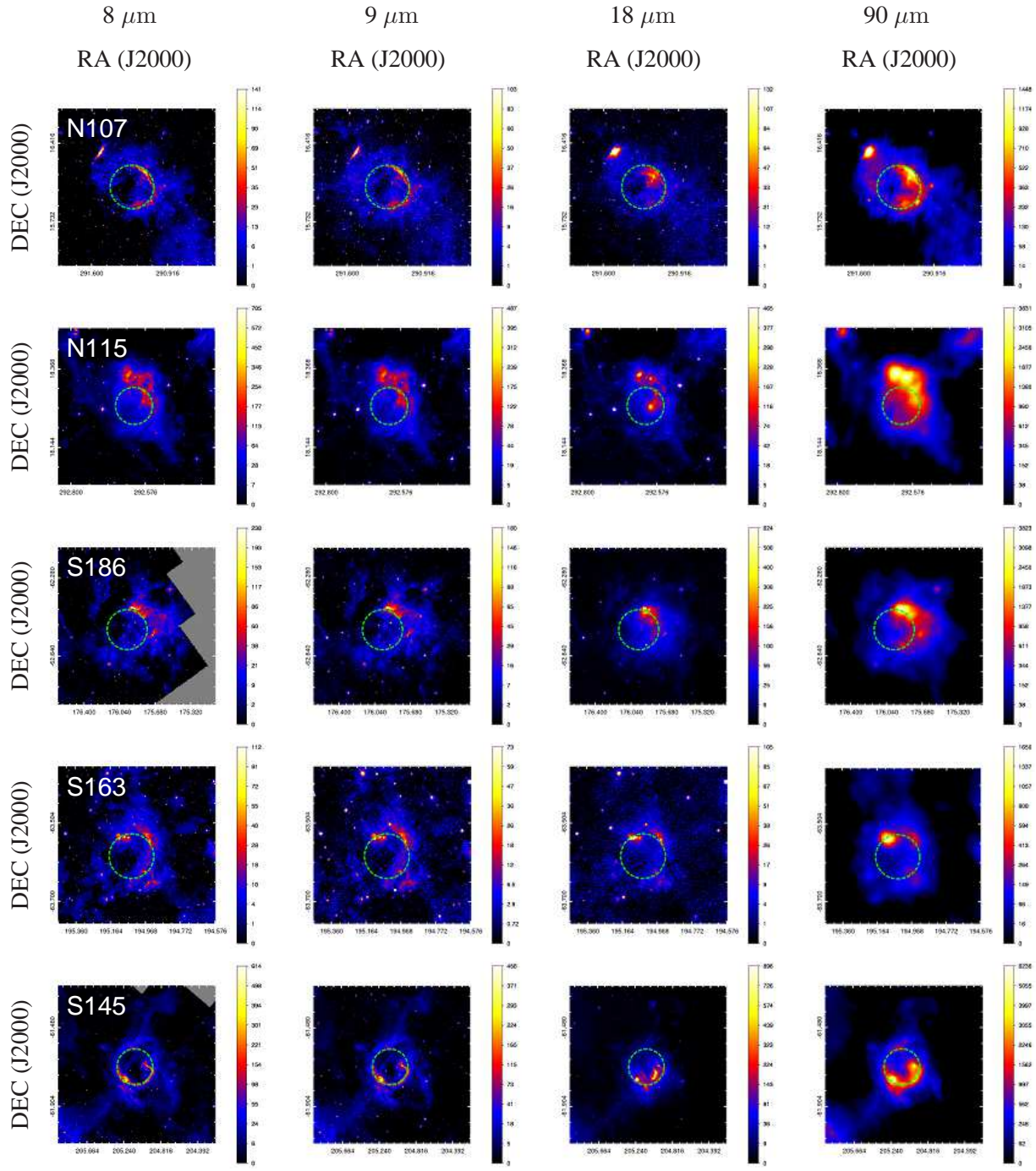


Fig. 1. Continued.

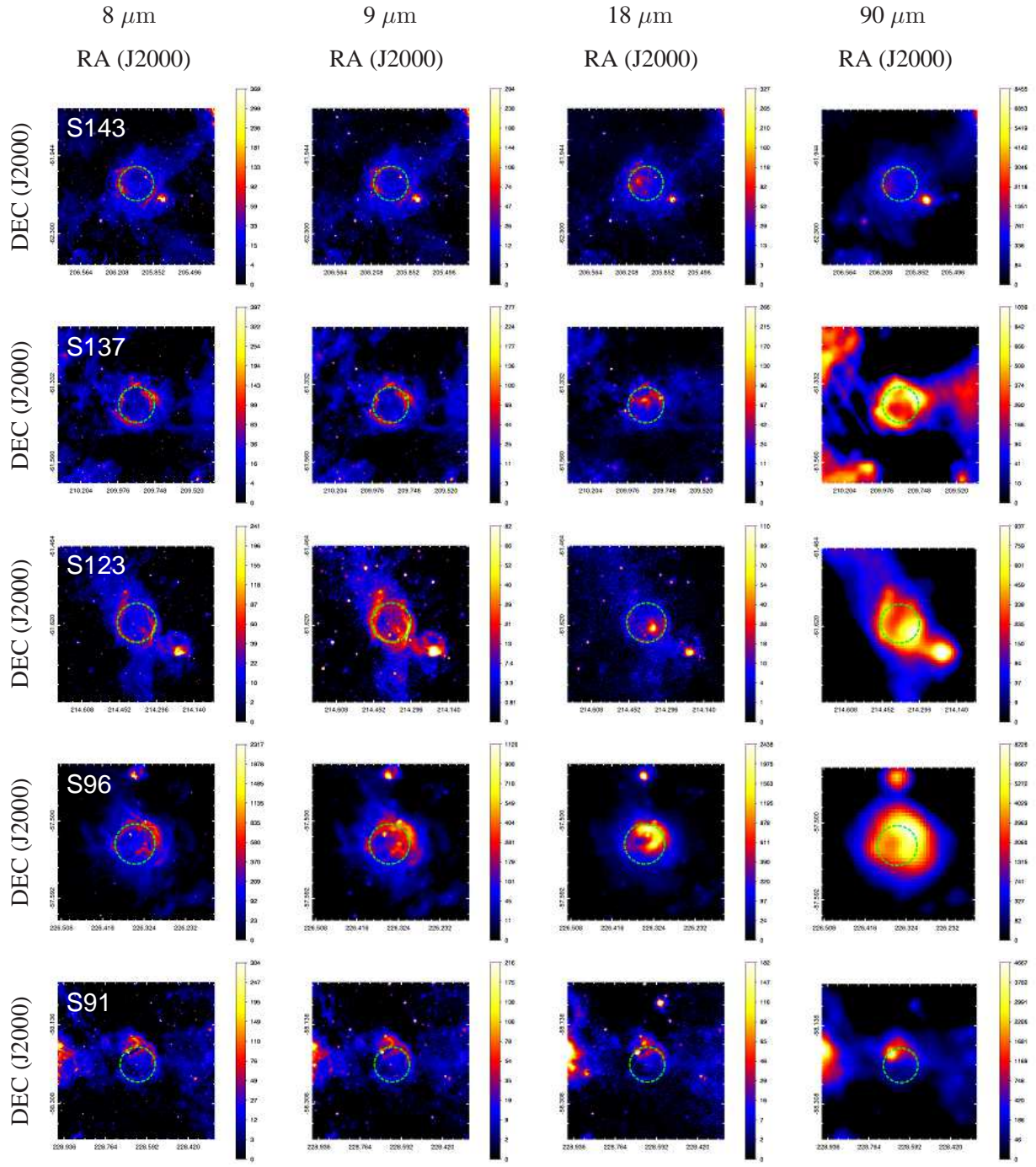


Fig. 1. Continued.

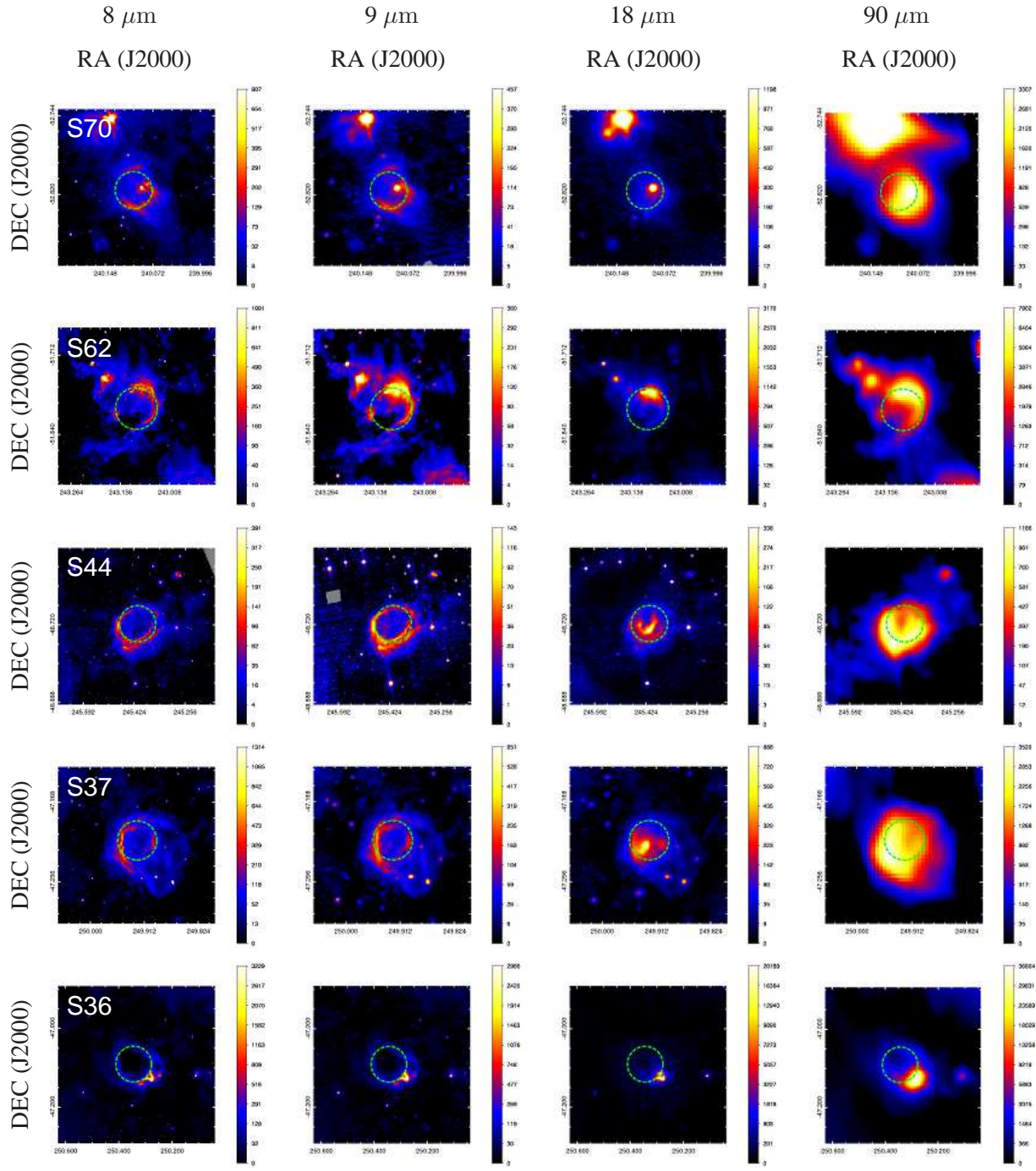


Fig. 1. Continued.

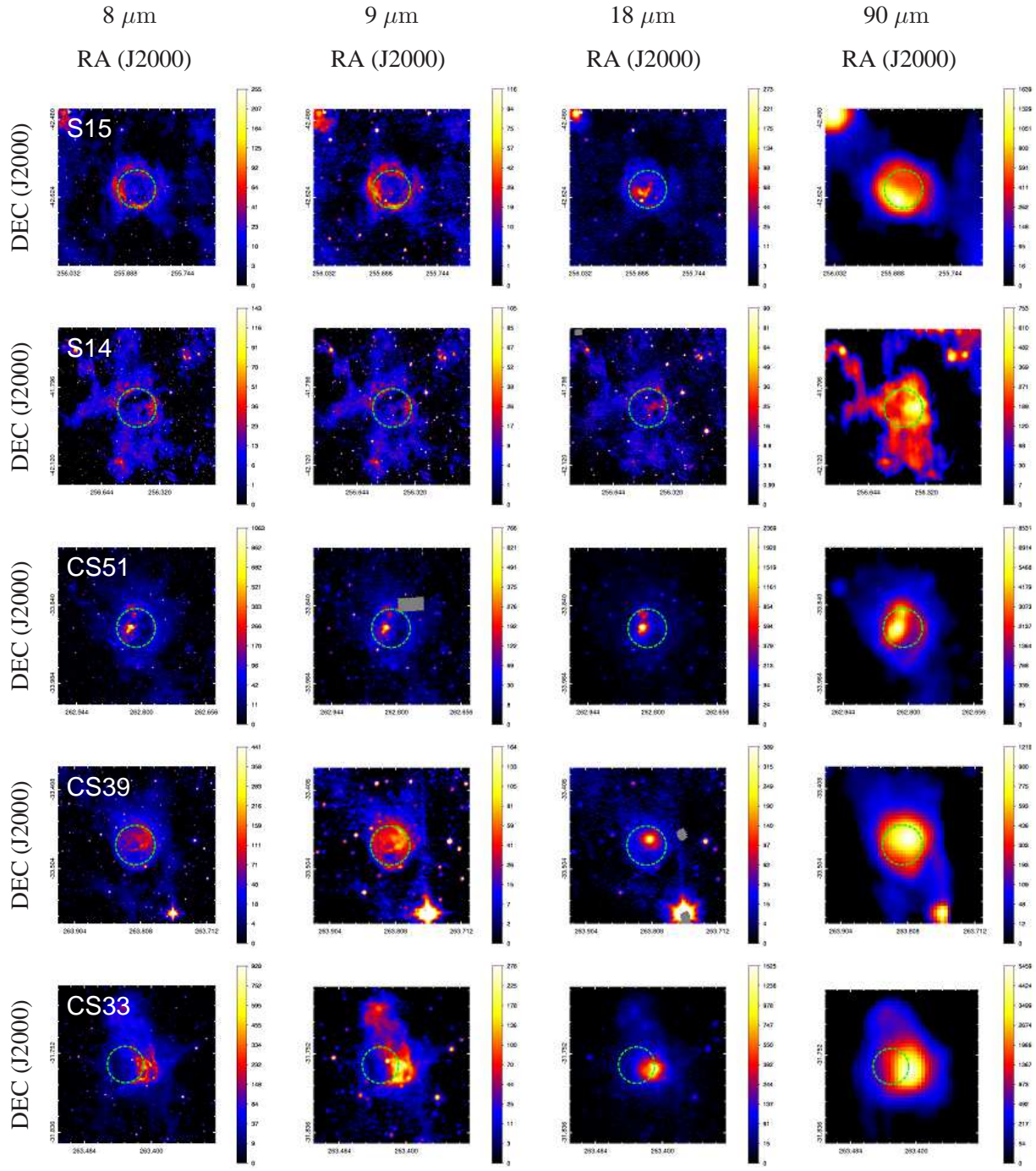


Fig. 1. Continued.

2 Observations and data analyses

The AKARI satellite (Murakami et al. 2007) performed all-sky surveys in the 6 photometric bands at the central wavelengths of 9, 18, 65, 90, 140 and 160 μm and provided the all-sky maps with better spatial resolutions and a wider spectral range than IRAS. We used the mid-IR data (Ishihara et al. in preparation) and the far-IR archive data¹ publicly released in 2015 (Doi et al. 2015). The full widths at half maxima (FWHMs) of the beam sizes in the 9, 18, 65, 90, 140 and 160 μm bands are $5''.5$, $5''.7$, $63''.4$, $77''.8$, $88''.3$ and $88''.3$, respectively, and the pixel scales of the mid-IR (9 and 18 μm) and far-IR (65, 90, 140 and 160 μm) all-sky images are $4''.68$ and $15''$, respectively (Onaka et al. 2007; Takita et al. 2015; Ishihara et al. in preparation).

Among the Galactic IR bubbles cataloged in Churchwell et al. (2006) and (2007), we selected the 223 bubbles for which the distances were measured in the previous works (Beaumont & Williams 2010; Cappa et al. 2014; Churchwell et al. 2006; Churchwell et al. 2007; Deharveng et al. 2009; Deharveng et al. 2010; Dewangan et al. 2015; Gennaro et al. 2012; Hou & Gao 2014; Pavel & Clemens 2012; Rahman & Murray 2010; Rodríguez-Esnard et al. 2012; Watson et al. 2009; Watson et al. 2010; Zhang et al. 2013). The distances and the references are summarized in columns 5 and 6 of table 1, respectively. In some cases, the kinematic distances which are determined from the Galactic rotational model and the radial velocities of the objects have distance ambiguity problems, as discussed in Roman-Duval et al. (2009). If there was ambiguity in the kinematic distance, we adopted shorter distances since nearer bubbles are more likely to be detected (Churchwell et al. 2006). For the bubbles with no distance errors given in table 1, we adopted the typical distance error of 13%, which is the median for the bubbles with known distance errors. Among the 223 bubbles, we found that 23 bubbles severely suffer source confusion and thus removed them from our sample. Hence we selected 200 bubbles in total as our initial sample.

Then we performed circular fitting to the selected sample to determine the central position and the radius of each bubble, using the Spitzer 8 μm images². For initial conditions of the fitting procedure, we considered the central positions (l_{Ch} , b_{Ch}) and radii (R_{Ch}) provided by Churchwell et al. (2006) and (2007) based on their visual inspection. We estimated the background brightness level from the annular region at $(2-4) \times R_{\text{Ch}}$ and subtracted it from the image of each bubble. Among the pixels contained in the area of $< 2R_{\text{Ch}}$, we selected the higher-brightness pixels which occupy 20% of the total. We carried out circular fitting to those pixels, where free parameters are the central position and the radius of a bubble. We used a least-square method to determine the best-fit parameters,

¹ Taken from <http://www.ir.isas.jaxa.jp/AKARI/Archive/Images/FISMAP/>.

² Taken from <http://irsa.ipac.caltech.edu/data/SPITZER/GLIMPSE/>.

calculating the following value:

$$\Delta^2 = \frac{\sum_i^n (\sqrt{(x_i - l)^2 + (y_i - b)^2} - R)^2}{n}, \quad (1)$$

where (x_i, y_i) is the coordinates of the i -th pixel, (l, b) and R are the central position and the radius of a fitting circle, respectively, and n is the number of the pixels. Churchwell et al. (2006) investigated the relation between the shell thicknesses and the outer bubble radii, R_{out} , for all the cataloged bubbles and found that almost every bubble has the thickness of $< 0.4R_{\text{out}}$. Therefore in the case that $|\Delta|$ is larger than $0.2R$, we considered that the bubble is likely to contain unrelated objects and removed pixels with larger deviations from the fitted circle. We iterated the fitting procedure until $|\Delta|$ becomes $< 0.2R$. The result is summarized in columns 7 to 9 of table 1. We compared the best-fit R , l and b with R_{Ch} , l_{Ch} and b_{Ch} in figure 2. The figure shows that the standard deviations of the differences are $\delta(|R - R_{\text{Ch}}|) = 0.11R$, $\delta(|l - l_{\text{Ch}}|) = 0.17R$ and $\delta(|b - b_{\text{Ch}}|) = 0.17R$. Thus we below consider potential systematic uncertainties of 11% and 17% of the radii and the central positions, respectively.

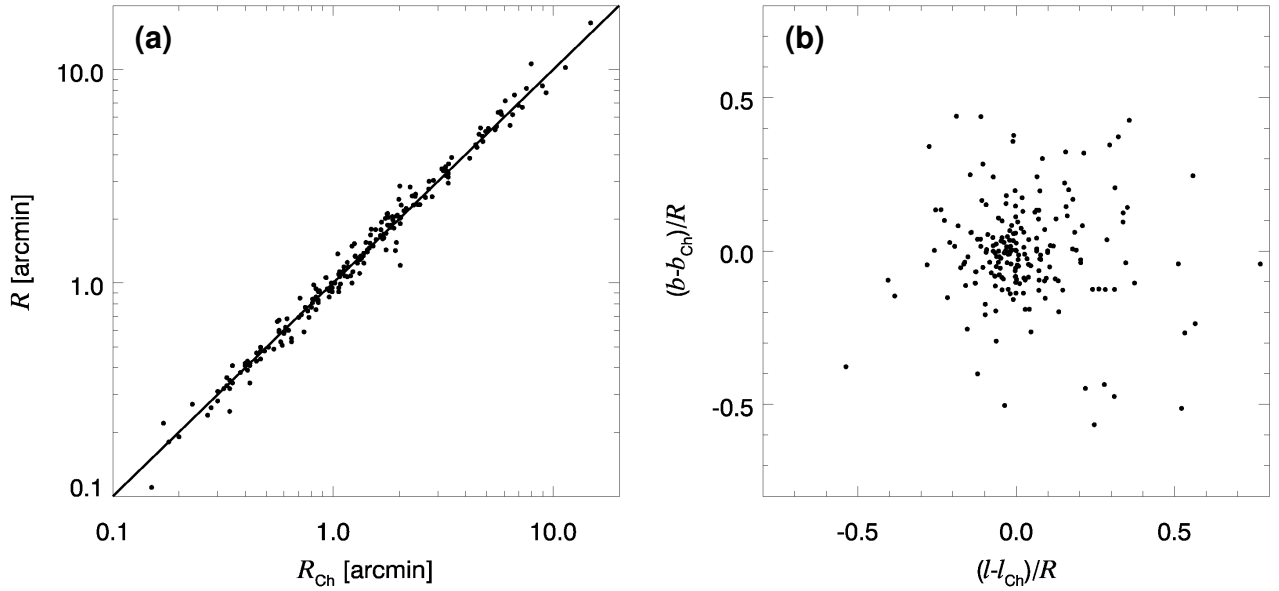


Fig. 2. Scatter plots of (a) R_{Ch} versus R and (b) $(l - l_{\text{Ch}})/R$ versus $(b - b_{\text{Ch}})/R$ for our sample of the Galactic IR bubbles. The line in panel (a) indicates $R = R_{\text{Ch}}$.

Now that the radii and the central positions are determined, we classify our sample into two types of morphologies (i.e., closed or broken). We estimated the covering fraction which represents the covering rate of the Spitzer $8 \mu\text{m}$ shell for the whole direction viewed from the bubble center. We again considered the annular region centered at (l, b) with $\pm 0.2R$ in radial thickness and divided it into 40 sectors equally (i.e., each subtended by 9°). For each sector, we counted the number of pixels which have brightness higher than 20% of the brightness averaged over the annular region. If the

filling factor, the ratio of those pixels to the total in a sector, was $< 20\%$, we regarded the sector as broken. Hence we classified the bubbles where at least one sector was missing into broken bubbles and the others into closed bubbles. To secure reliable classification, we used two thresholds for the brightness level, 20% and 30%, to identify a broken sector. Closed bubbles were identified on the basis of the higher threshold (30%) for a broken sector, while broken bubbles were identified on the basis of the lower threshold (20%) for a broken sector. As a result, the 200 sample bubbles are categorized into 81 closed, 58 broken and 61 unclassified bubbles, as summarized in column 10 of table 1. In comparison with Churchwell et al. (2006) and (2007), their 8 closed bubbles are categorized into broken bubbles and their 1 broken bubble is into a closed bubble by our classification.

Next, we estimated the flux densities of each bubble in the AKARI 6 bands through aperture photometry of a circular region of $< 2R$ centered at (l, b) . The result is summarized in table 2. We created a global SED from those flux densities. In order to create a local SED, we smoothed the 6-band images with a common Gaussian kernel of $90''$, which approximately corresponds to the FWHMs of the beam sizes of the 140 and $160\ \mu\text{m}$ all-sky images, and set a common pixel scale of $15''$ among the images. We subtracted the background levels estimated from the annular regions at $(2-4) \times R$ for each bubble. Flux uncertainties contain both random and systematic errors; the random errors were calculated from the background fluctuation, while the systematic errors were 10% (originating in the data processing such as corrections for the non-linearity of detector photoresponse; Ishihara et al. in preparation) for the 9 and $18\ \mu\text{m}$ bands and 15% for the 65, 90, 140 and $160\ \mu\text{m}$ bands. For the far-IR bands, we adopted 15% rather than 10% given by Takita et al. (2015), considering residual striping patterns along the scan direction which were recognized for about 40 bubbles in our sample.

The local SEDs created for every $15'' \times 15''$ pixel of the AKARI 6-band images were decomposed into PAH, warm and cold dust components by model fitting as was performed in Suzuki et al. (2013) and Kaneda et al. (2013). In the fitting, we adopted the PAH model spectrum in Draine & Li (2007) assuming the PAH size distribution and ionizing fraction typical of the diffuse ISM, and modified blackbody spectra with the emissivity power-law index β of 2 for warm and cold dust components. Free parameters were the amplitudes of the dust components and the temperature of warm dust. We fixed the temperature of cold dust at 18 K, because the temperature could not be confined well for the local SEDs. The temperature of 18 K was estimated from the fitting to the SED averaged over all the bubbles. It should be noted that the three components are just representative ones to reproduce the observed SEDs as good as possible and the selection of the model components does not essentially affect the following results. To determine the initial parameters of the local SED fitting, we first carried out fitting to the global SED described above. Since 20 bubbles were not acceptable with a 90% confidence level, we excluded these bubbles from our sample. Thus our sample finally

contains 74 closed, 49 broken and 57 unclassified bubbles. Among them, relatively large 20 closed and 20 broken bubbles are shown in figure 1 in increasing order of the Galactic longitude.

We obtained the brightness distributions of the PAH, warm and cold dust components, I_{PAH} , I_{warm} and I_{cold} , respectively, integrating each component over the wavelength range of 5–1000 μm . Figure 3 shows examples of the I_{PAH} , I_{warm} and I_{cold} maps thus obtained, which are the same bubbles as shown in figure 1. We estimated the fluxes of each dust component, using the same aperture as used in creating the global SEDs (i.e., $< 2R$). Using the fluxes and the distance, we obtained the luminosity of each component (L_{PAH} , L_{warm} and L_{cold}) and added them to obtain the total IR luminosity, L_{TIR} ($= L_{\text{PAH}} + L_{\text{warm}} + L_{\text{cold}}$). The luminosities are summarized in table 3.

To evaluate the effects of a rather small number of the AKARI SED data points in obtaining the luminosities, we overplotted the Spitzer 5.8, 8.0, Herschel 70, 160, 250, 350 and 500 μm photometric data points³ in the global SEDs of two typical examples in figure 4. We confirm that our estimates are consistent with the photometric data points except those in the submillimeter region. The result of the SED fitting to all the data points, with warm and cold dust temperatures allowed to vary, shows that L_{PAH} , L_{warm} and L_{cold} change by about -3% , -30% and $+20\%$, respectively. Hence the effects on L_{PAH} are likely to be negligible, whereas the effects on L_{warm} and L_{cold} are not. In table 3, we included 30% and 20% for the uncertainties of L_{warm} and L_{cold} in addition to the fitting and distance errors.

³ Taken from <http://www.cosmos.esa.int/web/herschel/science-archive/>.

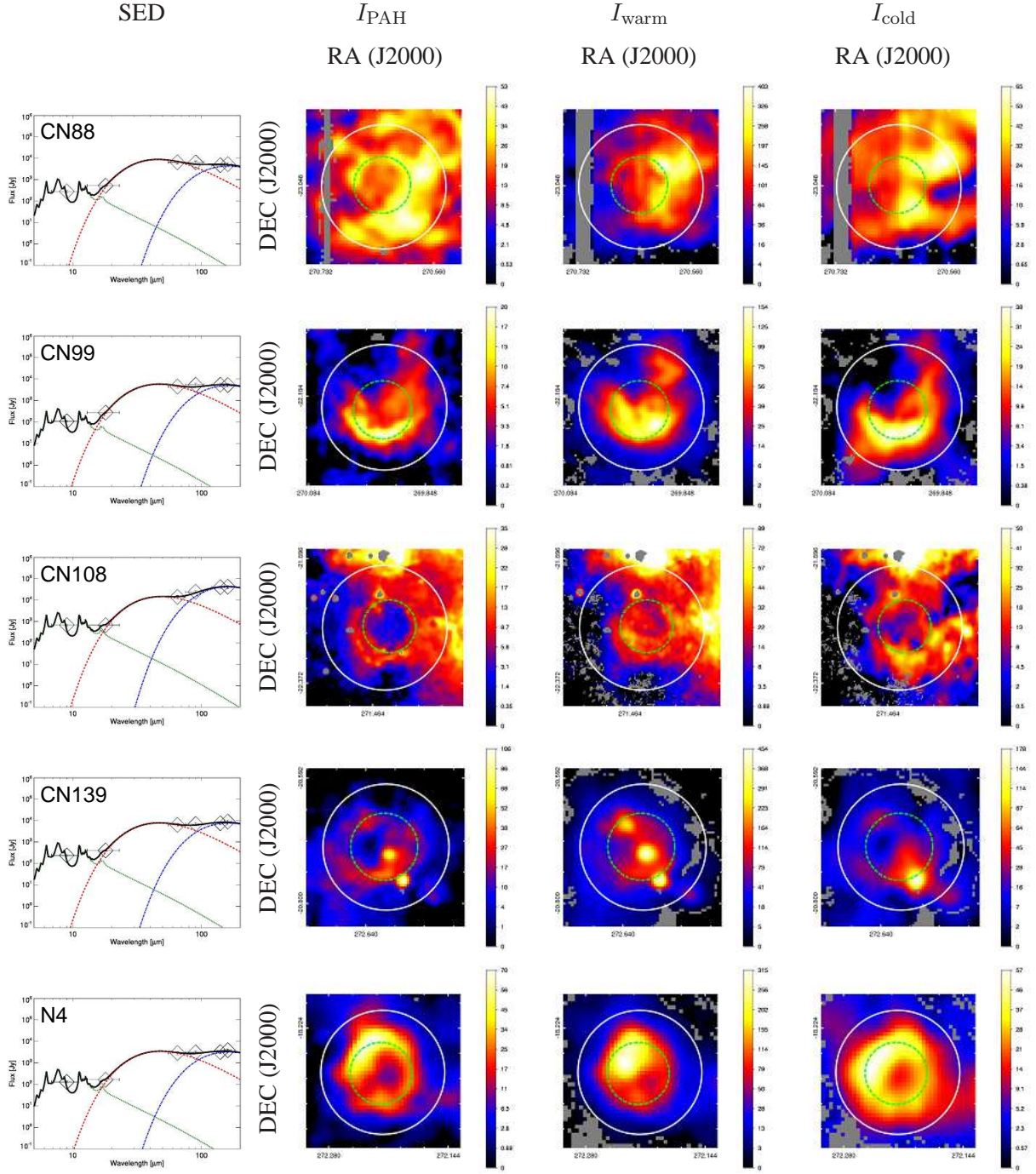


Fig. 3. From left to right, the global SED of the AKARI 6 photometric data points fitted by the dust model, the brightness maps of the PAH, warm and cold dust components for the sample bubbles shown in figures 1. In the SED plot, diamonds represent the photometric data points and the black solid curve indicates the best-fit result. The green dotted, red dashed and blue dashed-dotted curves indicate the best-fit PAH, warm and cold dust components, respectively. In the brightness maps, the green dashed circles are the same as those in figure 1, while the white solid circles are drawn with (l, b) and $2R$ from our fitting result. The color levels in the maps are given in units of $\mu\text{W m}^{-2} \text{sr}^{-1}$.

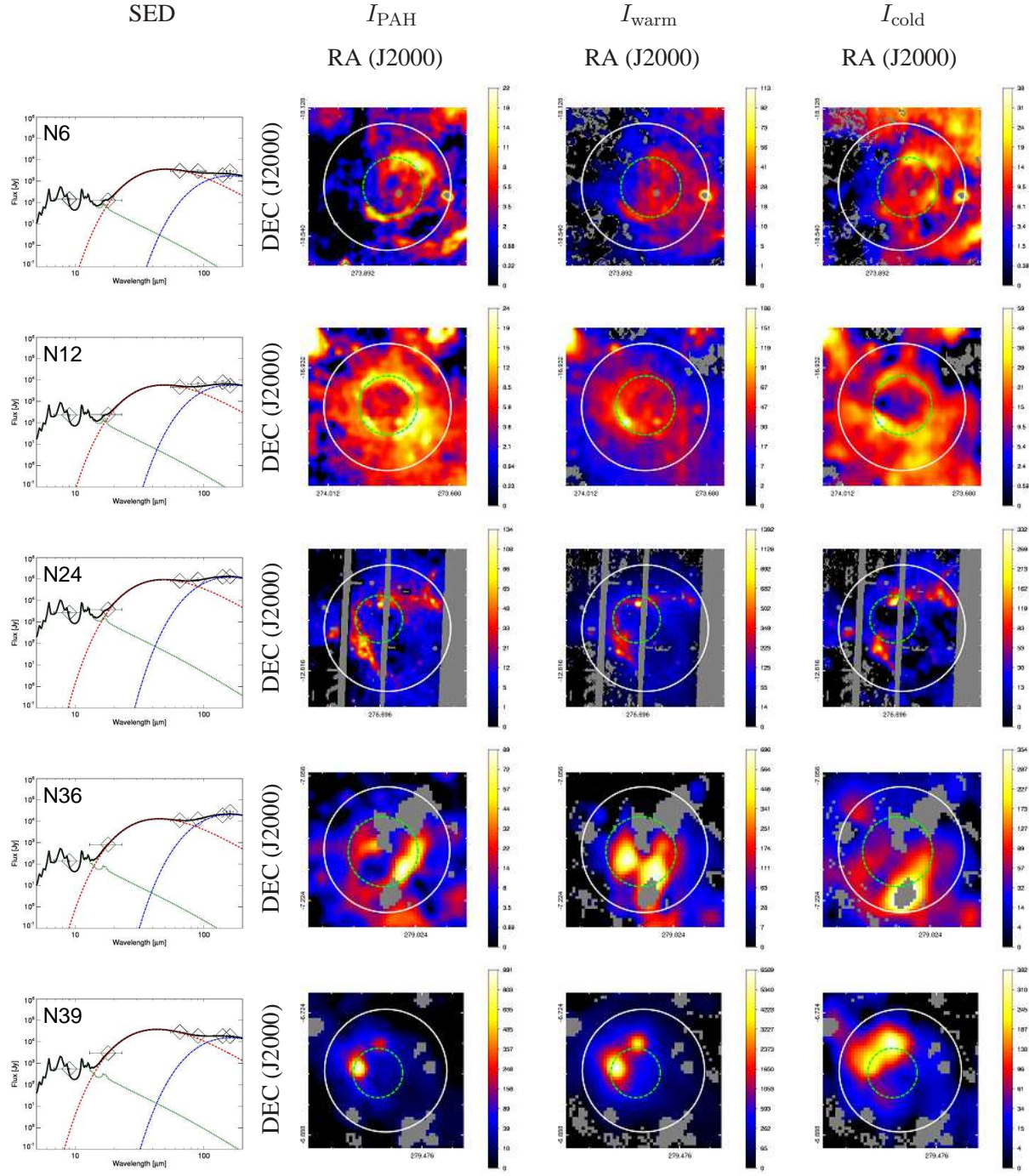


Fig. 3. Continued.

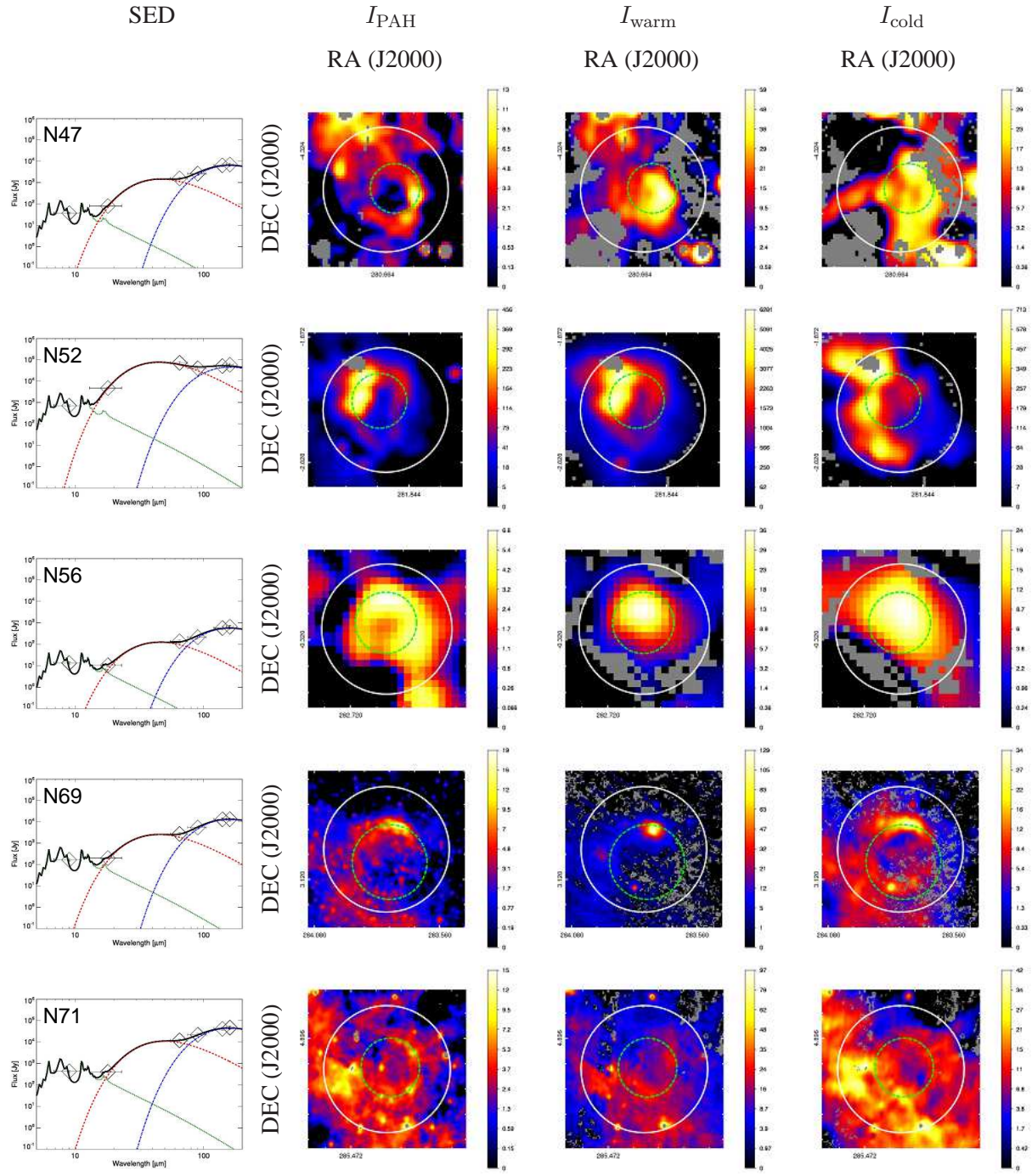


Fig. 3. Continued.

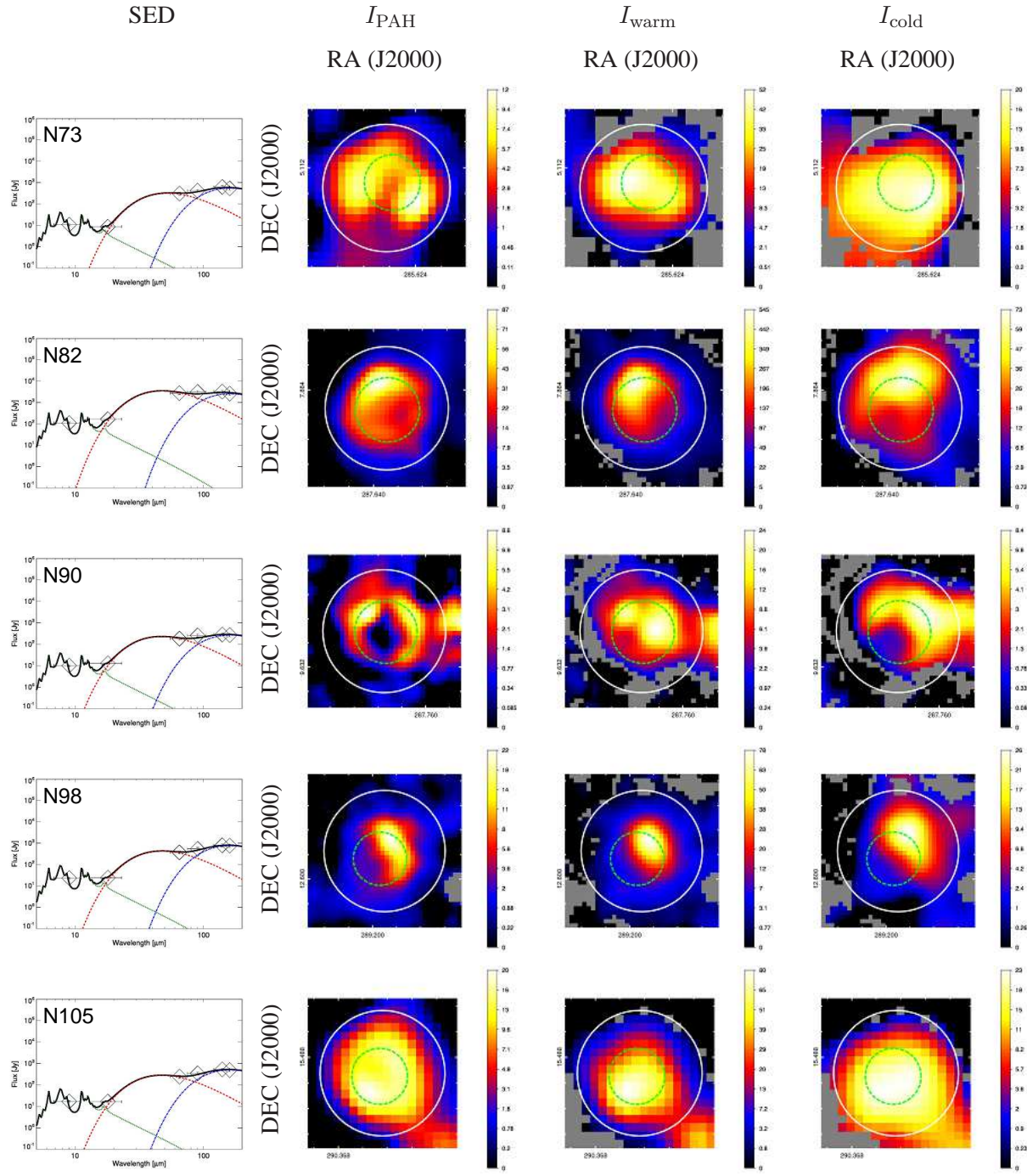


Fig. 3. Continued.

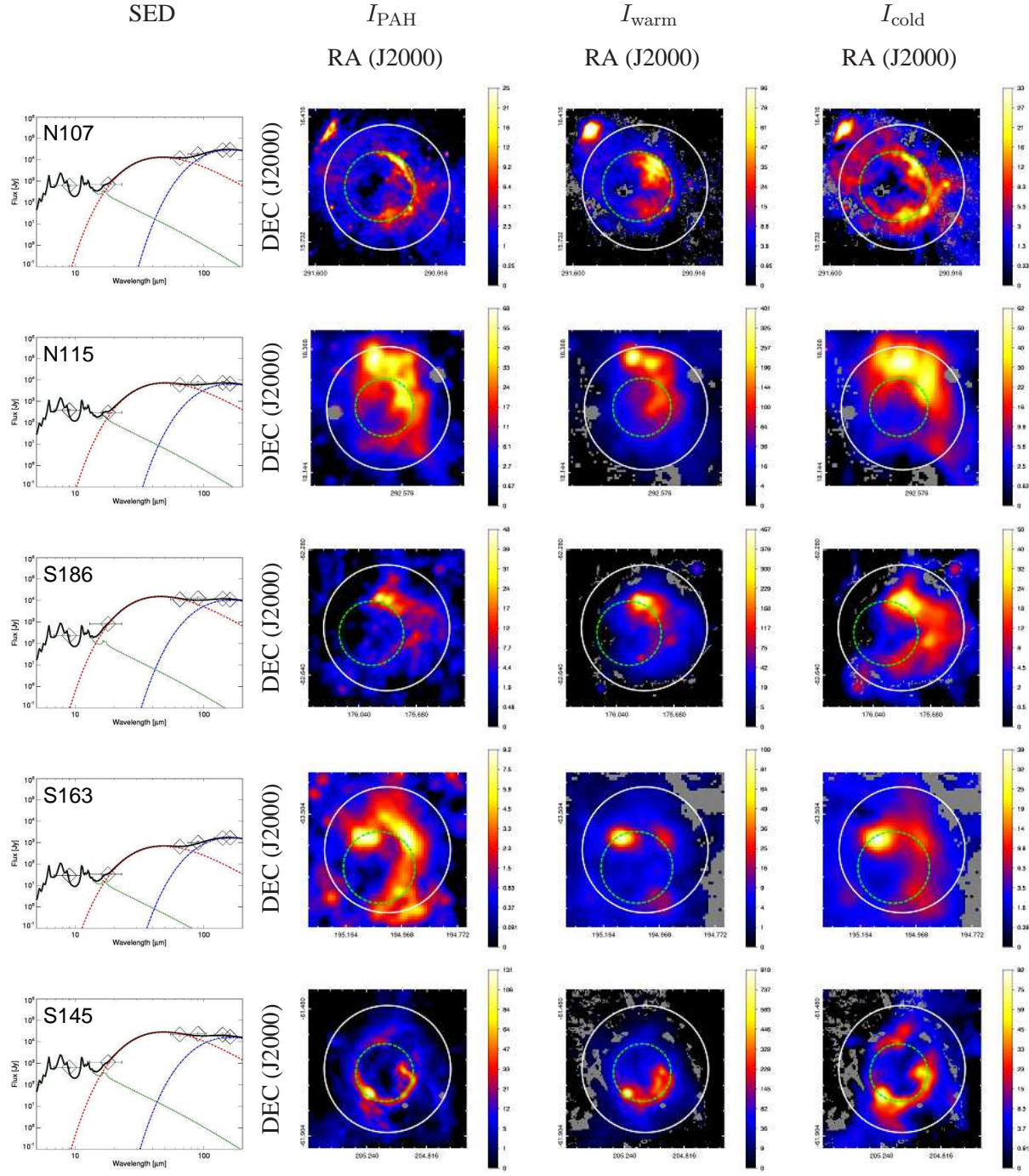


Fig. 3. Continued.

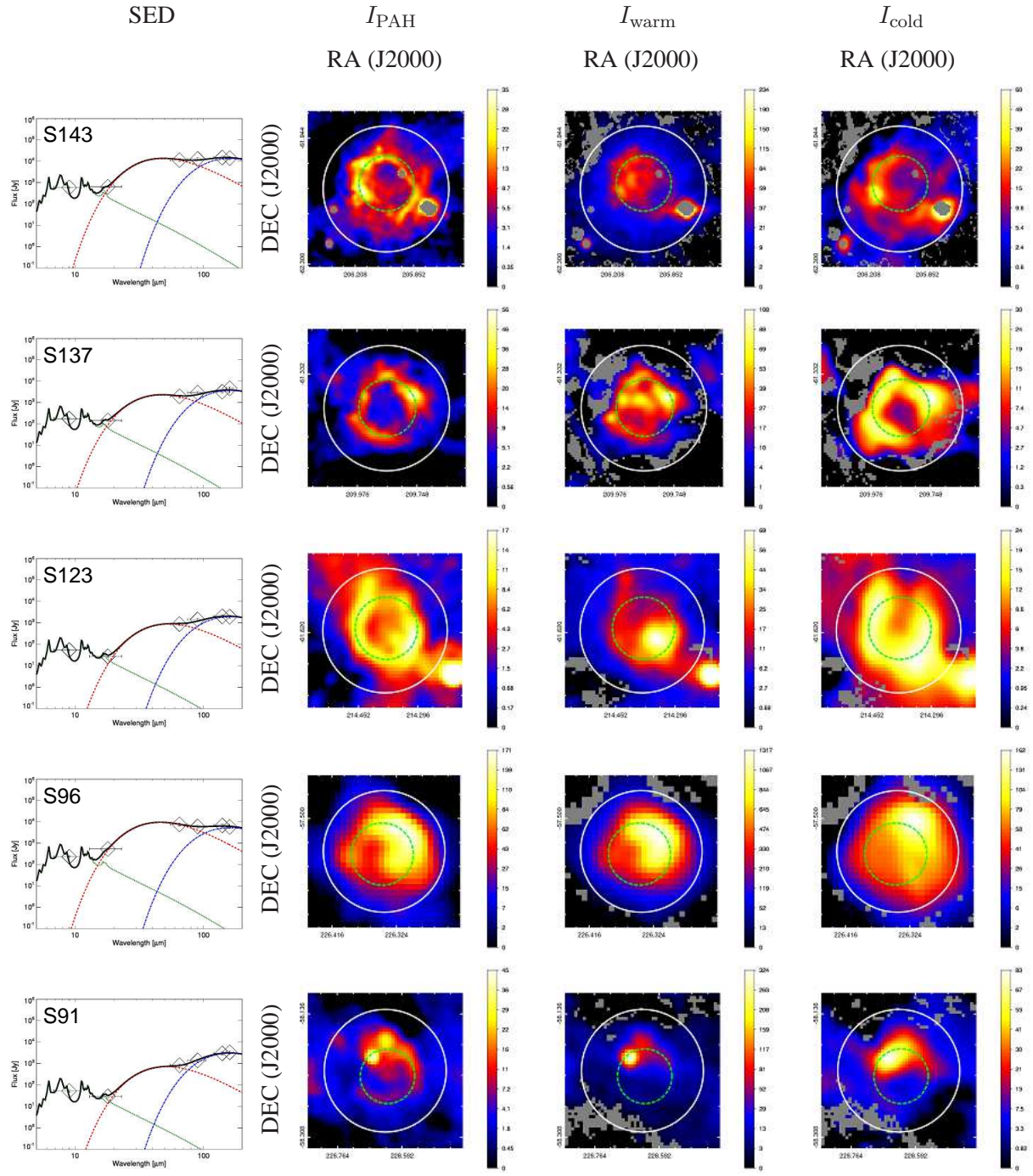


Fig. 3. Continued.

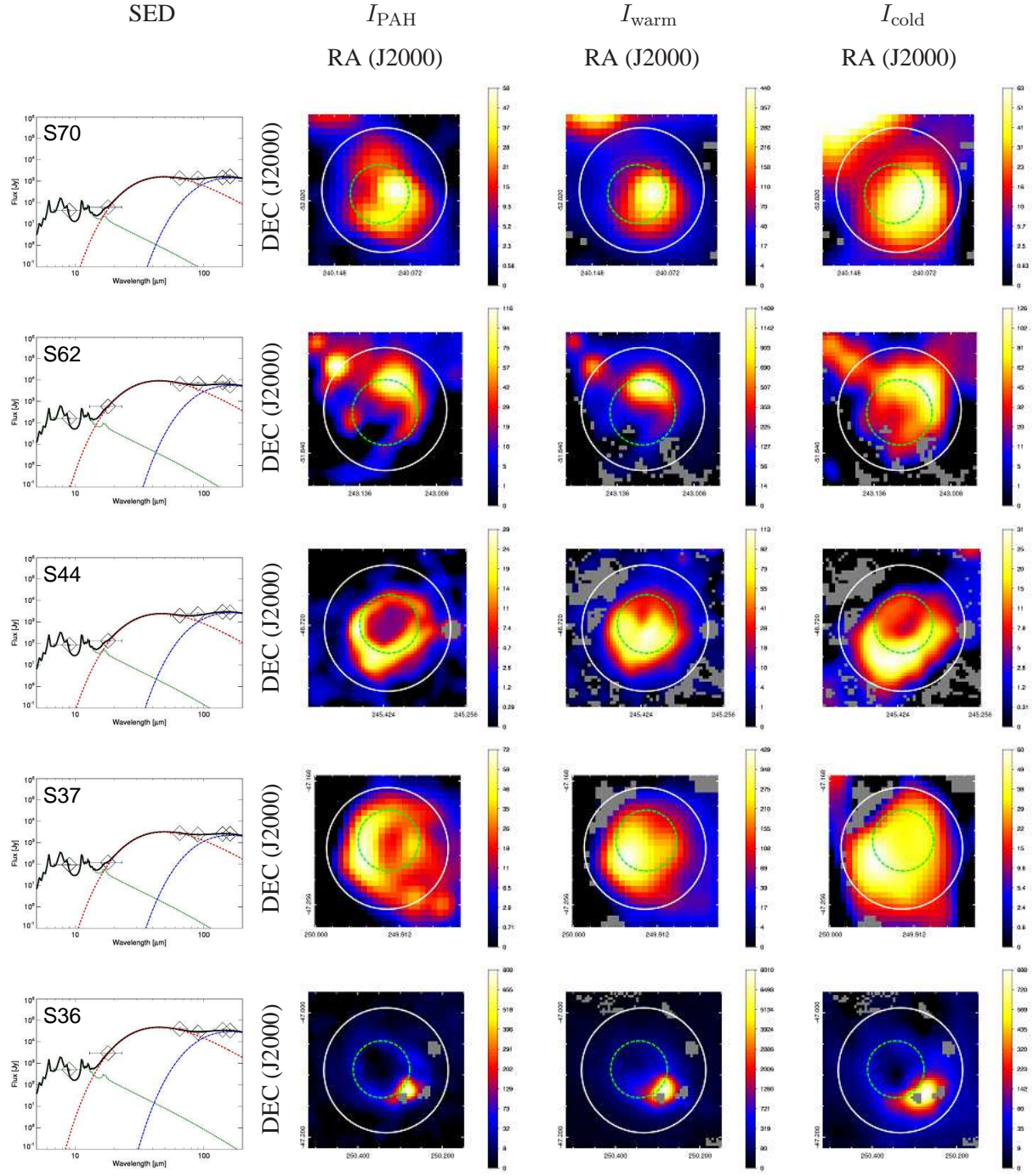


Fig. 3. Continued.

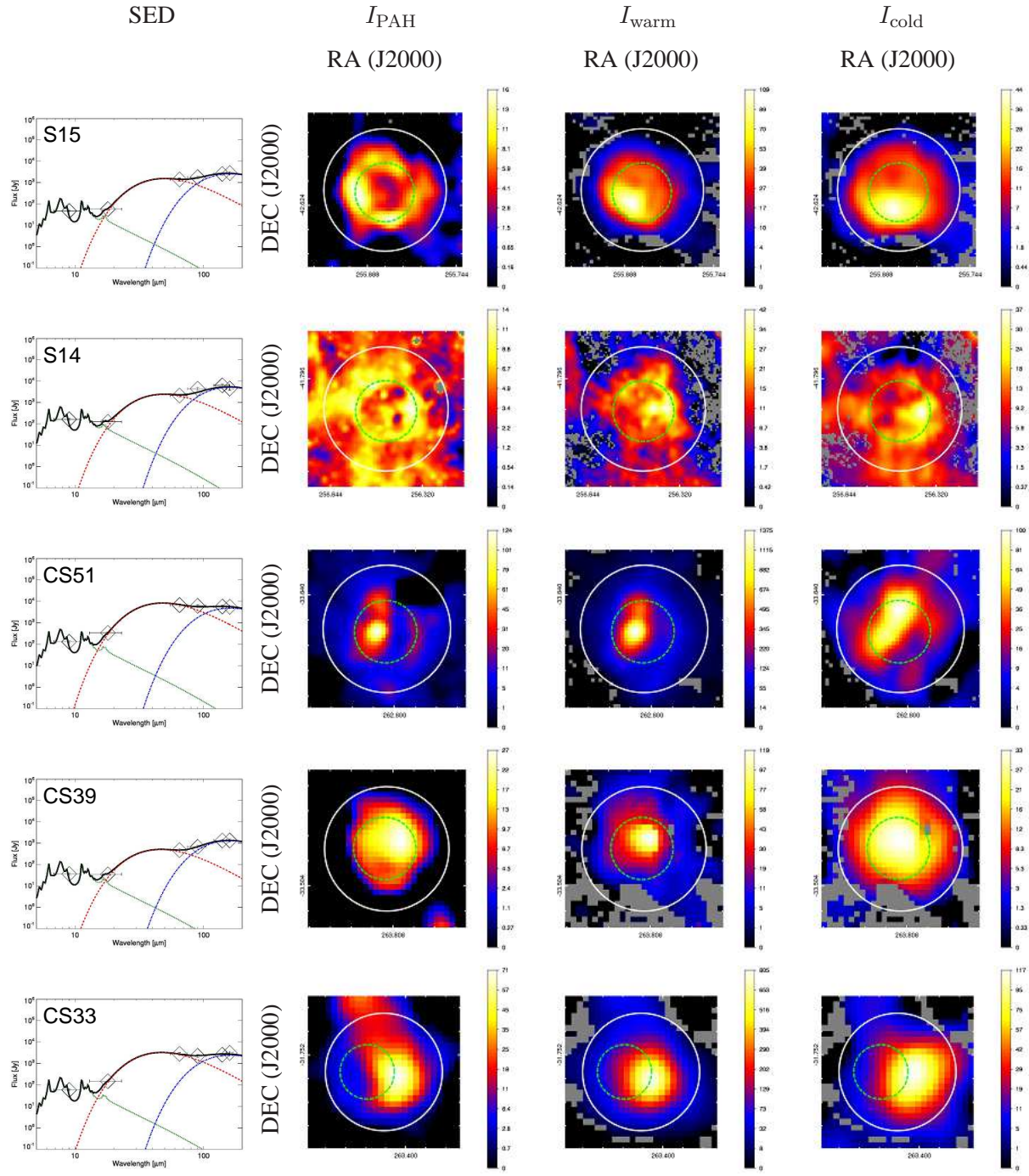


Fig. 3. Continued.

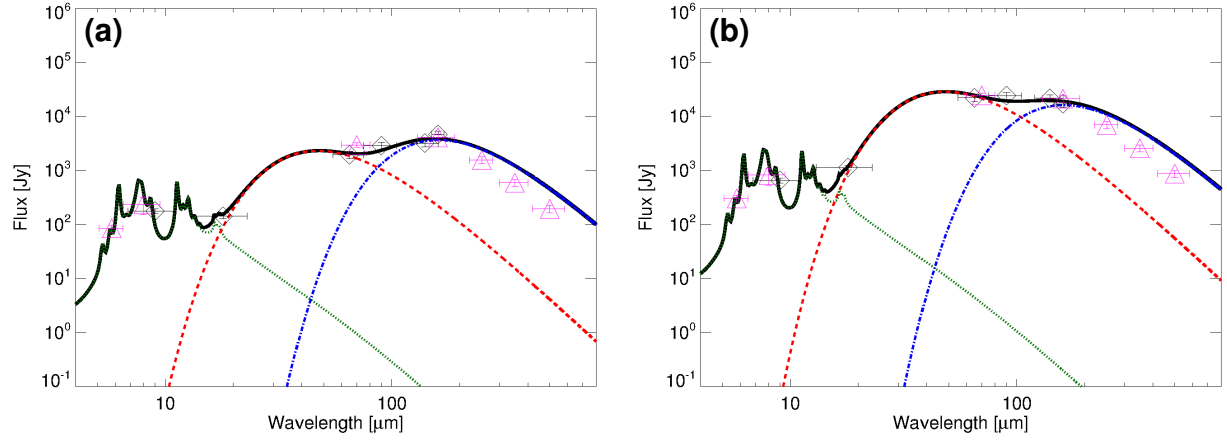


Fig. 4. Global SEDs of two typical examples of (a) closed bubble S137 and (b) broken bubble S145. Diamonds represent the AKARI photometric data points, while triangles represent the Spitzer and the Herschel photometric data points. The black solid curve indicates the result of fitting to the AKARI data alone. The green dotted, the red dashed and the blue dash-dotted represent the PAH, warm and cold dust components, respectively.

Table 1: Summary of the central positions and radii of the Galactic IR bubbles estimated from the circular fitting, and the morphological types based on our quantitative classification. The central positions and radii given in Churchwell et al. (2006) and (2007), and distances to the bubbles are also listed.

Name	l_{Ch} [deg]	b_{Ch} [deg]	R_{Ch} [']	D [kpc]	D ref.	l [deg]	b [deg]	R [']	Type**
CN15	0.562	-0.843	0.71	1.2 ± 0.5	Gen12	0.564	-0.842	0.85	B
CN17	0.593	-0.846	0.84	1.2 ± 0.5	Gen12	0.586	-0.840	0.75	
CN24	1.163	-0.097	1.92	11.2 ± 1.9	Hou14	1.150	-0.091	1.42	B
CN39	3.320	-0.029	0.34	13.8 ± 2.3	Hou14	3.320	-0.029	0.25	
CN43	3.651	-0.117	0.77	14.5 ± 2.5	Hou14	3.650	-0.119	0.74	C
CN58	4.386	0.073	0.86	14.2 ± 1.9	Hou14	4.386	0.073	0.81	C
CN63	4.563	-0.120	1.77	12.0 ± 0.7	Hou14	4.563	-0.126	1.87	
CN64	5.191	-0.282	0.72	15.4 ± 2.3	Hou14	5.191	-0.282	0.71	B
CN65	5.480	-0.238	0.41	12.0 ± 0.6	Hou14	5.481	-0.237	0.39	C
CN66	5.491	-0.237	0.57	12.0 ± 0.6	Hou14	5.492	-0.234	0.60	
CN71	5.894	-0.463	5.45	1.3 ± 0.1	Hou14	5.883	-0.472	5.23	
CN73	6.056	-0.128	1.83	1.3 ± 0.1	Hou14	6.060	-0.130	1.87	B
CN77	6.143	-0.639	1.06	12.5 ± 0.7	Hou14	6.138	-0.641	0.91	C
CN88	7.004	-0.295	2.37	2.7 ± 0.8	Hou14	7.001	-0.294	2.61	B
CN89	7.011	-0.254	0.30	2.7 ± 0.8	Hou14	7.012	-0.254	0.31	C
CN90	7.020	-0.187	1.76	2.7 ± 0.8	Hou14	7.021	-0.193	2.11	
CN98	7.368	-0.115	0.28	2.7 ± 0.8	Hou14	7.367	-0.115	0.26	
CN99	7.409	0.684	3.25	12.8 ± 0.6	Hou14	7.411	0.689	3.51	B
CN101	7.458	0.770	0.96	12.8 ± 0.6	Hou14	7.466	0.775	0.86	B
CN108	8.124	-0.465	6.06	4.9	Wat09	8.128	-0.483	7.15	C
CN111	8.312	-0.083	1.70	5.0 ± 0.3	Hou14	8.314	-0.084	1.70	C
CN113	8.351	-0.319	0.15	4.5 ± 0.4	Hou14	8.350	-0.319	0.11	C
CN114	8.361	-0.296	1.34	4.5 ± 0.4	Hou14	8.361	-0.296	1.34	
CN120	8.662	-0.342	0.27	4.6 ± 0.4	Hou14	8.661	-0.343	0.24	C
CN123	8.865	-0.328	0.86	4.4 ± 0.4	Hou14	8.868	-0.330	0.91	
CN135	9.612	0.196	0.34	5.2 ± 0.6	Hou14	9.613	0.196	0.32	C
CN138	9.833	-0.711	1.07	4.3 ± 0.6	Wat09	9.834	-0.709	1.07	C
CN139	9.939	-0.748	3.34	4.3 ± 0.7	Chu07	9.937	-0.746	3.14	C
CN142	9.996	-0.032	0.59	11.6 ± 0.3	Hou14	9.996	-0.030	0.51	C
CN145	10.187	-0.398	0.23	3.4 ± 0.3	Hou14	10.187	-0.398	0.27	
N1	10.231	-0.305	0.98	2.0*	Deh10	10.230	-0.305	1.00	
CN148	10.316	-0.131	1.41	2.2 ± 0.3	Dew15	10.316	-0.140	1.55	
N2	10.747	-0.468	6.95	8.4 ± 3.5	Chu06	10.749	-0.468	6.81	B
N4	11.892	0.748	2.01	3.4	Wat10	11.892	0.750	2.01	C

Continued.

Name	l_{Ch} [deg]	b_{Ch} [deg]	R_{Ch} [']	D [kpc]	D ref.	l [deg]	b [deg]	R [']	Type
N6	12.512	-0.609	5.83	4.1*	Deh10	12.522	-0.625	6.18	B
N10	13.188	0.039	1.22	4.6	Deh10	13.188	0.040	1.49	
N11	13.218	0.082	1.32	3.8	Wat10	13.225	0.085	1.11	
N12	13.727	-0.015	4.61	4.4*	Deh10	13.724	-0.018	4.98	C
N13	13.900	-0.014	0.49	3.4*	Deh10	13.899	-0.014	0.48	C
N14	14.002	-0.135	1.22	3.1	Wat10	14.004	-0.142	1.00	C
N16	15.017	0.056	2.48	13.7	Deh10	15.009	0.053	2.33	B
N18	16.679	-0.366	7.25	12.4	Deh10	16.684	-0.356	6.67	
N20	17.917	-0.687	1.12	12.8	Deh10	17.919	-0.686	1.14	C
N23	18.679	-0.237	0.45	11.5 \pm 1.2	Pav12	18.679	-0.236	0.47	B
N24	19.000	-0.326	7.96	4.6	Deh10	18.933	-0.307	10.67	B
N25	19.507	-0.191	0.75	12.8	Deh10	19.503	-0.189	0.77	
N27	19.814	0.017	1.08	3.8 \pm 1.1*	Bea10	19.812	0.019	0.99	B
N29	23.055	0.559	2.72	2.2	Deh10	23.050	0.559	2.76	C
N30	23.115	0.564	1.07	2.6 \pm 0.8*	Bea10	23.116	0.564	1.13	
N31	23.843	0.097	0.74	7.8 \pm 0.8	Pav12	23.840	0.101	0.59	B
N32	23.905	0.070	0.42	13.1	Deh10	23.904	0.070	0.42	
N33	24.215	-0.044	0.42	10.4	Deh10	24.215	-0.043	0.41	B
N34	24.295	-0.170	1.09	11.7	Deh10	24.295	-0.170	1.11	C
N35	24.513	0.241	3.26	8.6	Deh10	24.496	0.221	3.19	C
N36	24.837	0.090	2.82	6.4	Deh10	24.837	0.096	2.54	B
N37	25.292	0.293	1.77	3.3	Wat10	25.282	0.292	2.12	B
N39	25.364	-0.160	1.99	5.8	Wat10	25.362	-0.149	2.47	B
N40	25.369	-0.365	1.23	11.3	Deh10	25.367	-0.364	1.13	
N42	26.329	-0.071	0.61	5.9*	Deh10	26.329	-0.071	0.62	C
N43	26.597	0.098	0.65	9.0	Deh10	26.594	0.094	0.53	
N44	26.821	0.382	1.13	5.0*	Deh10	26.822	0.382	1.08	C
N45	26.991	-0.053	1.47	10.2	Deh10	26.993	-0.053	1.54	
N46	27.310	-0.110	1.38	5.6	Deh10	27.310	-0.109	1.38	B
N47	28.025	-0.031	2.24	7.3	Wat10	28.030	-0.044	2.82	B
N48	28.322	0.154	0.99	7.3	Wat10	28.324	0.153	0.91	
N49	28.827	-0.229	1.32	5.5	Deh10	28.828	-0.230	1.32	C
N50	29.001	0.097	1.70	10.6	Deh10	29.000	0.093	1.63	B
N51	29.158	-0.262	1.96	3.4	Wat10	29.154	-0.263	2.08	C
N52	30.749	-0.019	2.04	5.7	Wat10	30.736	-0.018	2.32	B
N53	31.157	-0.145	0.84	11.6	Deh10	31.157	-0.144	0.86	B
N54	31.164	0.292	1.78	3.0	Wat10	31.164	0.295	2.03	B

Continued.

Name	l_{Ch} [deg]	b_{Ch} [deg]	R_{Ch} [']	D [kpc]	D ref.	l [deg]	b [deg]	R [']	Type
N56	32.583	0.002	1.12	9.4	Deh10	32.579	0.001	1.19	C
N57	32.763	-0.150	0.32	2.1*	Deh10	32.762	-0.149	0.32	
N58	32.990	0.040	0.20	8.6	Deh10	32.990	0.040	0.19	C
N59	33.071	-0.075	6.68	5.6	Deh10	33.093	-0.068	7.62	C
N62	34.334	0.216	1.52	3.9	Wat10	34.336	0.218	1.49	B
N64	34.760	-0.669	4.80	3.2	Deh10	34.755	-0.669	4.61	
N65	35.000	0.332	2.15	3.1	Wat10	35.001	0.332	2.24	
N66	35.259	0.119	0.47	11.4	Deh10	35.260	0.120	0.44	B
N69	36.187	0.648	9.30	4.9	Deh10	36.240	0.660	7.81	B
N70	37.751	-0.112	0.57	10.4	Deh10	37.751	-0.112	0.59	C
N71	38.290	0.007	7.57	3.5*	Rah10	38.290	-0.008	8.18	B
N72	38.352	-0.133	1.00	1.5	Wat10	38.353	-0.132	1.00	B
N73	38.739	-0.137	0.93	9.2	Deh10	38.738	-0.141	1.06	B
N75	38.928	-0.387	0.70	2.8*	Deh10	38.928	-0.387	0.69	
N77	40.421	-0.056	1.29	5.0	Wat10	40.422	-0.055	1.24	B
N78	41.229	0.170	0.33	1.5*	Deh10	41.229	0.170	0.33	
N79	41.514	0.030	1.26	2.8	Wat10	41.514	0.029	1.33	C
N80	41.930	0.031	1.82	1.4	Wat10	41.932	0.037	1.82	C
N81	42.003	-0.512	8.95	8.1	Deh10	41.994	-0.518	8.41	
N82	42.102	-0.623	1.68	5.2	Wat10	42.103	-0.623	1.61	C
N83	42.113	-0.442	0.33	9.2	Deh10	42.112	-0.443	0.36	C
N84	42.831	-0.161	1.16	1.1	Wat10	42.833	-0.157	1.07	
N89	43.739	0.114	1.02	5.5	Wat10	43.739	0.114	1.00	
N90	43.774	0.059	1.74	3.1	Wat10	43.775	0.058	1.71	C
N91	44.211	0.050	5.08	8.1	Deh10	44.215	0.041	5.31	
N92	44.333	-0.839	1.94	3.7	Wat10	44.336	-0.829	1.55	
N95	45.393	-0.717	2.02	4.4	Wat10	45.377	-0.716	1.21	C
N96	46.947	0.368	0.42	16.2	Deh10	46.946	0.371	0.34	
N98	47.027	0.219	1.56	4.6	Wat10	47.032	0.227	1.78	C
N101	49.197	-0.358	1.17	5.1	Wat10	49.195	-0.359	1.19	B
N104	50.041	-0.273	0.81	5.3 ± 1.6	Hou14	50.040	-0.276	0.84	C
N105	50.077	0.569	0.84	10.6 ± 1.1	Pav12	50.078	0.571	0.94	C
N106	50.785	0.168	0.41	5.6 ± 1.3	Hou14	50.786	0.168	0.43	C
N107	50.972	0.078	11.39	$4.7 \pm 0.8^*$	Chu06	50.949	0.112	10.25	B
N109	51.982	0.562	14.83	10.7 ± 0.9	Rod12	52.007	0.547	16.61	B
N110	52.159	0.710	0.63	9.6 ± 1.0	Pav12	52.161	0.710	0.60	C
N111	52.204	0.750	1.06	9.2 ± 0.5	Hou14	52.206	0.749	0.95	

Continued.

Name	l_{Ch} [deg]	b_{Ch} [deg]	R_{Ch} [']	D [kpc]	D ref.	l [deg]	b [deg]	R [']	Type
N113	52.229	0.737	0.57	10.7 \pm 0.9	Rod12	52.230	0.738	0.67	C
N114	52.250	0.703	1.57	9.3 \pm 0.5	Hou14	52.250	0.704	1.60	
N115	53.556	-0.014	3.17	2.7	Wat10	53.551	-0.009	3.36	C
N116	54.091	-0.088	0.82	6.9 \pm 0.6	Hou14	54.094	-0.089	0.98	
N117	54.112	-0.064	1.66	5.1	Wat10	54.107	-0.068	1.93	C
N120	55.266	0.249	1.37	1.9 \pm 0.6*	Bea10	55.268	0.250	1.34	C
N122	56.077	-0.184	0.58	4.7 \pm 0.5	Pav12	56.077	-0.180	0.53	
N123	57.539	-0.284	1.38	2.6	Wat10	57.534	-0.281	1.24	C
N124	58.605	0.638	1.74	3.2	Wat10	58.607	0.632	1.43	B
N125	58.764	0.655	0.80	4.3 \pm 1.8	Hou14	58.765	0.653	0.77	
N126	59.606	0.330	1.87	6.3	Wat10	59.601	0.319	1.98	
N127	60.648	-0.057	3.34	0.9	Wat10	60.649	-0.061	3.27	B
N130	62.370	-0.540	1.05	3.0	Wat10	62.376	-0.543	1.37	B
N131	63.084	-0.395	6.55	8.6 \pm 1.0	Zha13	63.084	-0.410	6.16	B
N133	63.159	0.451	1.64	2.1	Wat10	63.159	0.449	1.67	C
N134	64.134	-0.466	0.56	3.7 \pm 1.1	Chu06	64.136	-0.469	0.66	
S186	295.223	-0.665	5.54	3.6	Chu06	295.177	-0.661	5.43	B
S181	298.210	-0.315	1.49	4.0	Chu06	298.218	-0.315	1.79	C
S163	303.905	-0.732	3.34	11.4 \pm 0.6	Hou14	303.893	-0.704	2.94	B
S156	305.263	0.214	1.89	4.9 \pm 1.1	Chu06	305.261	0.215	1.93	C
S155	305.263	-0.002	0.47	6.4 \pm 0.8	Hou14	305.264	-0.002	0.48	C
S150	305.533	0.357	1.06	4.0 \pm 1.1	Hou14	305.534	0.357	1.10	C
S149	305.553	0.010	0.45	4.9 \pm 0.7	Chu06	305.552	0.011	0.43	
S145	308.709	0.627	5.78	5.3 \pm 0.9	Chu06	308.701	0.641	6.36	B
S144	308.749	0.549	0.86	4.6 \pm 1.1	Hou14	308.749	0.549	0.83	
S143	309.052	0.172	4.68	5.3 \pm 1.1	Chu06	309.050	0.157	5.34	C
S141	309.552	-0.719	1.46	3.9 \pm 1.3*	Chu06	309.552	-0.721	1.46	C
S138	310.909	-0.361	0.99	12.8 \pm 0.6	Hou14	310.911	-0.358	0.95	B
S137	310.980	0.411	3.12	5.1 \pm 1.1*	Chu06	310.981	0.410	3.43	C
S136	311.189	0.751	0.62	5.5 \pm 0.9	Chu06	311.189	0.752	0.68	C
S135	311.474	0.403	0.34	5.5 \pm 1.6	Hou14	311.474	0.404	0.35	
S134	311.484	0.363	0.60	5.7 \pm 0.3	Chu06	311.484	0.362	0.58	
S133	311.487	0.395	2.03	5.6 \pm 0.3	Chu06	311.487	0.398	2.03	C
S132	311.495	0.416	0.18	5.5 \pm 1.6	Hou14	311.494	0.416	0.18	C
S123	312.975	-0.433	2.32	3.9 \pm 1.4*	Chu06	312.976	-0.436	2.32	C
S116	314.219	0.474	4.18	5.9 \pm 0.9	Chu06	314.237	0.477	3.85	C
S115	315.979	-0.182	0.94	11.2 \pm 0.5	Hou14	315.979	-0.181	0.94	C

Continued.

Name	l_{Ch} [deg]	b_{Ch} [deg]	R_{Ch} [']	D [kpc]	D ref.	l [deg]	b [deg]	R [']	Type
S104	317.988	-0.749	1.73	$2.7 \pm 0.7^*$	Chu06	317.995	-0.750	2.01	
S96	320.164	0.793	1.43	$2.6 \pm 0.7^*$	Chu06	320.164	0.795	1.40	C
S92	320.578	0.203	6.38	8.9 ± 0.5	Hou14	320.595	0.163	5.49	
S91	320.861	-0.422	2.29	3.0 ± 0.4	Hou14	320.868	-0.417	2.56	B
S84	323.915	0.032	0.35	9.9 ± 0.4	Hou14	323.914	0.030	0.41	C
S76	326.924	-0.021	4.94	$3.4 \pm 0.6^*$	Chu06	326.927	-0.021	5.14	
S74	327.525	-0.848	1.33	2.6 ± 0.5	Hou14	327.527	-0.848	1.29	B
S73	327.552	-0.807	3.46	2.6 ± 0.5	Hou14	327.547	-0.814	3.88	
S71	327.990	-0.103	1.07	7.2 ± 0.6	Chu06	327.986	-0.109	1.07	C
S70	329.276	0.108	1.07	9.8 ± 0.3	Hou14	329.275	0.112	1.13	B
S67	330.675	-0.389	0.96	$4.9 \pm 0.5^*$	Chu06	330.675	-0.388	0.92	B
S66	330.781	-0.414	5.63	3.7 ± 0.3	Hou14	330.785	-0.414	6.31	
S65	330.789	-0.454	0.51	3.7 ± 0.3	Hou14	330.790	-0.454	0.50	C
S64	331.010	-0.156	2.86	$3.8 \pm 0.5^*$	Chu06	331.005	-0.148	3.03	
S62	331.316	-0.359	2.02	$4.4 \pm 0.5^*$	Chu06	331.318	-0.356	1.90	B
S54	332.311	-0.565	1.20	11.3 ± 0.3	Hou14	332.314	-0.565	1.08	
S51	332.673	-0.618	1.48	3.8 ± 0.5	Hou14	332.666	-0.615	1.68	
S44	334.523	0.823	2.36	$4.6 \pm 0.5^*$	Chu06	334.520	0.818	2.55	C
S41	336.483	-0.214	3.28	5.1	Wat10	336.484	-0.216	3.35	
S37	337.692	-0.339	1.30	3.5	Rah10	337.688	-0.343	1.30	C
S36	337.971	-0.474	2.73	$4.0 \pm 0.5^*$	Chu06	337.965	-0.469	3.00	B
S34	338.120	-0.189	0.47	11.9 ± 0.3	Hou14	338.120	-0.188	0.50	
S29	338.901	0.609	2.63	$3.3 \pm 0.6^*$	Chu06	338.906	0.612	2.52	
S24	341.205	-0.229	0.40	3.7 ± 0.8	Cap14	341.205	-0.230	0.42	C
S23	341.281	-0.349	1.94	3.3	Wat10	341.280	-0.346	2.06	
S20	342.045	0.396	1.25	1.0*	Chu06	342.045	0.386	1.53	
S18	342.075	0.434	1.26	4.2 ± 0.3	Hou14	342.075	0.433	1.34	C
S17	343.482	-0.044	1.89	2.9	Wat10	343.480	-0.048	1.81	C
S16	343.521	-0.004	0.35	13.2 ± 0.5	Hou14	343.521	-0.004	0.34	C
S15	343.914	-0.649	2.10	$3.1 \pm 0.7^*$	Chu06	343.916	-0.647	2.18	C
S14	344.756	-0.554	4.78	2.9	Wat10	344.761	-0.551	4.88	C
S11	345.480	0.399	2.43	2.0	Wat10	345.482	0.400	2.33	
S8	347.401	0.265	1.67	6.3 ± 0.3	Chu06	347.397	0.261	1.64	C
S7	348.258	0.483	4.45	1.3	Deh09	348.259	0.483	4.45	B
S1	349.811	-0.602	4.51	$3.6 \pm 0.9^*$	Chu06	349.814	-0.605	4.33	B
CS100	350.674	0.836	0.54	1.7 ± 0.3	Hou14	350.673	0.834	0.49	B
CS98	350.710	0.999	0.40	1.7 ± 0.3	Hou14	350.712	0.998	0.41	C

Continued.

Name	l_{Ch} [deg]	b_{Ch} [deg]	R_{Ch} [']	D [kpc]	D ref.	l [deg]	b [deg]	R [']	Type
CS93	351.030	0.154	0.81	17.7 ± 2.3	Hou14	351.027	0.154	0.81	B
CS84	351.476	-0.460	0.65	13.2 ± 0.7	Hou14	351.471	-0.458	0.55	
CS82	351.597	0.157	0.61	11.6 ± 0.4	Hou14	351.595	0.157	0.60	C
CS81	351.646	0.165	1.35	11.6 ± 0.4	Hou14	351.646	0.165	1.31	B
CS80	351.663	0.159	0.60	11.6 ± 0.4	Hou14	351.662	0.159	0.59	C
CS79	351.675	0.516	3.35	1.7 ± 0.3	Hou14	351.675	0.522	3.62	
CS72	352.235	-0.152	0.38	5.0	Hou14	352.234	-0.152	0.38	B
CS71	352.393	-0.065	0.86	5.0	Hou14	352.393	-0.065	0.82	C
CS62	353.113	0.337	2.01	1.9 ± 0.4	Hou14	353.096	0.330	2.85	B
CS60	353.220	-0.260	0.87	2.6 ± 1.1	Hou14	353.220	-0.258	0.92	C
CS57	353.354	-0.138	1.65	6.2	Wat09	353.354	-0.140	1.78	C
CS55	353.417	-0.375	0.78	3.8 ± 2.4	Chu07	353.411	-0.378	0.69	B
CS51	354.182	-0.053	2.13	5.3 ± 0.7	Chu07	354.184	-0.050	2.17	C
CS45	354.674	0.245	0.17	10.6 ± 0.2	Hou14	354.673	0.244	0.22	C
CS40	354.937	0.331	0.30	8.5	Chu07	354.938	0.329	0.28	
CS39	354.978	-0.532	1.43	16.8 ± 3.6	Hou14	354.977	-0.531	1.43	C
CS33	356.241	0.667	1.16	9.5 ± 0.1	Hou14	356.235	0.677	1.25	B
CS2	359.740	-0.411	1.86	1.5 ± 0.2	Hou14	359.742	-0.412	2.05	B

References: Bea10: Beaumont & Williams (2010); Cap14: Cappa et al. (2014); Chu06: Churchwell et al. (2006); Chu07: Churchwell et al. (2007); Deh09: Deharveng et al. (2009); Deh10: Deharveng et al. (2010); Dew15: Dewangan et al. (2015); Gen12: Gennaro et al. (2012); Hou14: Hou & Gao (2014); Pav12: Pavel & Clemens (2012); Rah10: Rahman & Murray (2010); Rod12: Rodríguez-Esnard et al. (2012); Wat09: Watson et al. (2009); Wat10: Watson et al. (2010); Zha13: Zhang et al. (2013). *: The nearer kinematic distance is adopted. **: C is a closed type, while B is a broken type. The others are unclassified.

Table 2: Summary of the flux densities obtained by the circular ($< 2R$) aperture photometry.

Name	Flux 9 μm [Jy]	Flux 18 μm [Jy]	Flux 65 μm [Jy]	Flux 90 μm [Jy]	Flux 140 μm [Jy]	Flux 160 μm [Jy]	Notes
CN15	$(1.15 \pm 0.01) \times 10^2$	$(3.69 \pm 0.03) \times 10^2$	$(8.7 \pm 0.2) \times 10^3$	$(4.6 \pm 0.1) \times 10^3$	$(5.9 \pm 0.2) \times 10^3$	$(7.8 \pm 0.3) \times 10^3$	
CN17	$(4.94 \pm 0.01) \times 10^1$	$(1.099 \pm 0.001) \times 10^2$	$(1.926 \pm 0.005) \times 10^3$	$(1.85 \pm 0.01) \times 10^3$	$(2.04 \pm 0.02) \times 10^3$	$(1.78 \pm 0.02) \times 10^3$	sc
CN24	$(1.311 \pm 0.007) \times 10^2$	$(5.77 \pm 0.01) \times 10^2$	$(7.07 \pm 0.06) \times 10^3$	$(4.32 \pm 0.06) \times 10^3$	$(6.0 \pm 0.2) \times 10^3$	$(7.0 \pm 0.3) \times 10^3$	
CN39	$(2.94 \pm 0.03) \times 10^0$	$(5.98 \pm 0.06) \times 10^0$	$(7.2 \pm 0.4) \times 10^1$	$(5.6 \pm 0.3) \times 10^1$	$(3.9 \pm 0.2) \times 10^1$	$(5.0 \pm 0.3) \times 10^1$	sc
CN43	$(5.2 \pm 0.2) \times 10^0$	$(1.22 \pm 0.02) \times 10^1$	$(4.2 \pm 0.1) \times 10^2$	$(4.4 \pm 0.1) \times 10^2$	$(4.9 \pm 0.2) \times 10^2$	$(7.2 \pm 0.2) \times 10^2$	
CN58	$(1.800 \pm 0.008) \times 10^1$	$(2.939 \pm 0.007) \times 10^1$	$(8.15 \pm 0.03) \times 10^2$	$(9.64 \pm 0.04) \times 10^2$	$(1.63 \pm 0.02) \times 10^3$	$(1.32 \pm 0.01) \times 10^3$	sc
CN63	$(4.22 \pm 0.02) \times 10^1$	$(4.96 \pm 0.03) \times 10^1$	$(1.23 \pm 0.02) \times 10^3$	$(1.37 \pm 0.02) \times 10^3$	$(2.66 \pm 0.02) \times 10^3$	$(2.03 \pm 0.03) \times 10^3$	sc
CN64	$(6.01 \pm 0.07) \times 10^0$	$(1.974 \pm 0.007) \times 10^1$	$(3.31 \pm 0.04) \times 10^2$	$(3.71 \pm 0.04) \times 10^2$	$(3.4 \pm 0.1) \times 10^2$	$(3.58 \pm 0.08) \times 10^2$	sc
CN65	$(1.41 \pm 0.02) \times 10^1$	$(9.62 \pm 0.06) \times 10^1$	$(6.1 \pm 0.5) \times 10^2$	$(3.4 \pm 0.3) \times 10^2$	$(3.1 \pm 0.3) \times 10^2$	$(4.0 \pm 0.4) \times 10^2$	
CN66	$(1.83 \pm 0.04) \times 10^1$	$(7.6 \pm 0.2) \times 10^1$	$(9.6 \pm 0.5) \times 10^2$	$(6.6 \pm 0.5) \times 10^2$	$(8.1 \pm 0.4) \times 10^2$	$(1.17 \pm 0.06) \times 10^3$	
CN71	$(1.365 \pm 0.001) \times 10^3$	$(3.270 \pm 0.001) \times 10^3$	$(7.175 \pm 0.003) \times 10^4$	$(5.235 \pm 0.004) \times 10^4$	$(6.57 \pm 0.01) \times 10^4$	$(6.51 \pm 0.02) \times 10^4$	sc
CN73	$(1.14 \pm 0.05) \times 10^1$	$(1.463 \pm 0.007) \times 10^2$	$(2.27 \pm 0.05) \times 10^3$	$(1.93 \pm 0.06) \times 10^3$	$(1.62 \pm 0.08) \times 10^3$	$(1.49 \pm 0.08) \times 10^3$	
CN77	$(7.68 \pm 0.06) \times 10^1$	$(9.8 \pm 0.2) \times 10^1$	$(2.14 \pm 0.07) \times 10^3$	$(1.61 \pm 0.04) \times 10^3$	$(1.97 \pm 0.04) \times 10^3$	$(3.18 \pm 0.06) \times 10^3$	
CN88	$(2.82 \pm 0.02) \times 10^2$	$(5.27 \pm 0.02) \times 10^2$	$(6.5 \pm 0.1) \times 10^3$	$(6.5 \pm 0.1) \times 10^3$	$(4.8 \pm 0.2) \times 10^3$	$(5.3 \pm 0.2) \times 10^3$	
CN89	$(5.1 \pm 0.6) \times 10^0$	$(5.3 \pm 0.8) \times 10^0$	$(2.1 \pm 0.2) \times 10^2$	$(1.0 \pm 0.1) \times 10^2$	$(6.0 \pm 0.5) \times 10^1$	$(1.1 \pm 0.1) \times 10^2$	
CN90	$(1.37 \pm 0.02) \times 10^2$	$(2.37 \pm 0.02) \times 10^2$	$(3.4 \pm 0.1) \times 10^3$	$(3.19 \pm 0.09) \times 10^3$	$(3.14 \pm 0.08) \times 10^3$	$(3.6 \pm 0.1) \times 10^3$	
CN98	$(2.85 \pm 0.04) \times 10^0$	$(3.10 \pm 0.04) \times 10^0$	$(2.9 \pm 0.1) \times 10^1$	$(1.7 \pm 0.1) \times 10^1$	$(1.9 \pm 0.2) \times 10^1$	$(4.3 \pm 0.3) \times 10^1$	sc
CN99	$(1.087 \pm 0.005) \times 10^2$	$(2.788 \pm 0.004) \times 10^2$	$(4.51 \pm 0.02) \times 10^3$	$(5.42 \pm 0.03) \times 10^3$	$(5.43 \pm 0.06) \times 10^3$	$(5.26 \pm 0.06) \times 10^3$	
CN101	$(2.5 \pm 0.1) \times 10^0$	$(9.3 \pm 0.3) \times 10^0$	$(1.5 \pm 0.1) \times 10^2$	$(1.3 \pm 0.1) \times 10^2$	$(1.2 \pm 0.1) \times 10^2$	$(7.8 \pm 1.4) \times 10^1$	
CN108	$(6.835 \pm 0.006) \times 10^2$	$(6.750 \pm 0.007) \times 10^2$	$(1.420 \pm 0.002) \times 10^4$	$(2.447 \pm 0.002) \times 10^4$	$(4.003 \pm 0.006) \times 10^4$	$(4.231 \pm 0.007) \times 10^4$	sc
CN111	$(6.20 \pm 0.02) \times 10^1$	$(6.50 \pm 0.02) \times 10^1$	$(1.23 \pm 0.01) \times 10^3$	$(1.641 \pm 0.008) \times 10^3$	$(2.06 \pm 0.02) \times 10^3$	$(2.13 \pm 0.02) \times 10^3$	sc
CN113	$(2.05 \pm 0.01) \times 10^1$	$(2.41 \pm 0.02) \times 10^1$	$(4.6 \pm 0.2) \times 10^2$	$(2.4 \pm 0.1) \times 10^2$	$(2.7 \pm 0.2) \times 10^2$	$(8.9 \pm 1.0) \times 10^1$	sc
CN114	$(7.40 \pm 0.09) \times 10^1$	$(9.4 \pm 0.1) \times 10^1$	$(2.1 \pm 0.1) \times 10^3$	$(1.9 \pm 0.1) \times 10^3$	$(1.9 \pm 0.1) \times 10^3$	$(2.5 \pm 0.1) \times 10^3$	
CN120	$(2.108 \pm 0.004) \times 10^1$	$(6.65 \pm 0.01) \times 10^1$	$(1.20 \pm 0.03) \times 10^3$	$(6.8 \pm 0.1) \times 10^2$	$(7.6 \pm 0.4) \times 10^2$	$(9.0 \pm 0.3) \times 10^2$	sc
CN123	$(3.066 \pm 0.008) \times 10^1$	$(4.57 \pm 0.01) \times 10^1$	$(7.56 \pm 0.04) \times 10^2$	$(7.73 \pm 0.03) \times 10^2$	$(9.0 \pm 0.1) \times 10^2$	$(8.79 \pm 0.08) \times 10^2$	sc
CN135	$(3.314 \pm 0.007) \times 10^1$	$(1.279 \pm 0.001) \times 10^2$	$(3.0 \pm 0.2) \times 10^3$	$(1.3 \pm 0.1) \times 10^3$	$(8.2 \pm 0.7) \times 10^2$	$(1.65 \pm 0.06) \times 10^3$	sc
CN138	$(1.191 \pm 0.005) \times 10^1$	$(1.02 \pm 0.01) \times 10^1$	$(3.55 \pm 0.02) \times 10^2$	$(4.90 \pm 0.02) \times 10^2$	$(7.25 \pm 0.05) \times 10^2$	$(8.8 \pm 0.1) \times 10^2$	sc
CN139	$(2.387 \pm 0.006) \times 10^2$	$(4.096 \pm 0.006) \times 10^2$	$(6.32 \pm 0.02) \times 10^3$	$(7.01 \pm 0.03) \times 10^3$	$(7.58 \pm 0.08) \times 10^3$	$(9.01 \pm 0.08) \times 10^3$	
CN142	$(3.99 \pm 0.05) \times 10^0$	$(5.57 \pm 0.05) \times 10^0$	$(2.24 \pm 0.07) \times 10^2$	$(2.16 \pm 0.09) \times 10^2$	$(2.2 \pm 0.1) \times 10^2$	$(2.2 \pm 0.2) \times 10^2$	
CN145	$(1.25 \pm 0.02) \times 10^1$	$(2.66 \pm 0.03) \times 10^1$	$(7.6 \pm 0.2) \times 10^2$	$(2.6 \pm 0.2) \times 10^2$	$(4.3 \pm 0.3) \times 10^2$	$(6.0 \pm 0.4) \times 10^2$	sc
N1	$(4.59 \pm 0.02) \times 10^1$	$(1.128 \pm 0.002) \times 10^2$	$(3.07 \pm 0.01) \times 10^3$	$(2.459 \pm 0.009) \times 10^3$	$(2.64 \pm 0.01) \times 10^3$	$(2.65 \pm 0.01) \times 10^3$	sc
CN148	$(2.547 \pm 0.008) \times 10^2$	$(1.726 \pm 0.001) \times 10^3$	$(2.115 \pm 0.009) \times 10^4$	$(1.105 \pm 0.008) \times 10^4$	$(1.26 \pm 0.02) \times 10^4$	$(1.69 \pm 0.02) \times 10^4$	

Continued.

Name	Flux 9 μm [Jy]	Flux 18 μm [Jy]	Flux 65 μm [Jy]	Flux 90 μm [Jy]	Flux 140 μm [Jy]	Flux 160 μm [Jy]	Notes
N2	$(4.90 \pm 0.01) \times 10^2$	$(1.020 \pm 0.001) \times 10^3$	$(3.421 \pm 0.007) \times 10^4$	$(3.25 \pm 0.01) \times 10^4$	$(3.00 \pm 0.03) \times 10^4$	$(5.04 \pm 0.03) \times 10^4$	
N4	$(1.307 \pm 0.006) \times 10^2$	$(1.654 \pm 0.005) \times 10^2$	$(2.88 \pm 0.04) \times 10^3$	$(3.10 \pm 0.04) \times 10^3$	$(3.18 \pm 0.05) \times 10^3$	$(3.90 \pm 0.05) \times 10^3$	
N6	$(1.432 \pm 0.005) \times 10^2$	$(1.272 \pm 0.005) \times 10^2$	$(3.06 \pm 0.02) \times 10^3$	$(2.96 \pm 0.02) \times 10^3$	$(1.92 \pm 0.05) \times 10^3$	$(2.85 \pm 0.06) \times 10^3$	sc
N10	$(1.195 \pm 0.002) \times 10^2$	$(4.111 \pm 0.002) \times 10^2$	$(5.682 \pm 0.008) \times 10^3$	$(4.38 \pm 0.02) \times 10^3$	$(6.86 \pm 0.03) \times 10^3$	$(7.71 \pm 0.05) \times 10^3$	sc
N11	$(4.38 \pm 0.02) \times 10^1$	$(5.13 \pm 0.02) \times 10^1$	$(1.149 \pm 0.004) \times 10^3$	$(1.299 \pm 0.008) \times 10^3$	$(1.91 \pm 0.02) \times 10^3$	$(1.91 \pm 0.04) \times 10^3$	sc
N12	$(2.31 \pm 0.02) \times 10^2$	$(2.44 \pm 0.03) \times 10^2$	$(4.7 \pm 0.2) \times 10^3$	$(6.6 \pm 0.2) \times 10^3$	$(7.9 \pm 0.3) \times 10^3$	$(5.4 \pm 0.4) \times 10^3$	
N13	$(2.01 \pm 0.05) \times 10^0$	$(3.72 \pm 0.08) \times 10^0$	$(1.27 \pm 0.07) \times 10^2$	$(1.11 \pm 0.08) \times 10^2$	$(1.2 \pm 0.1) \times 10^2$	$(1.6 \pm 0.2) \times 10^2$	
N14	$(1.34 \pm 0.01) \times 10^2$	$(3.14 \pm 0.01) \times 10^2$	$(5.0 \pm 0.1) \times 10^3$	$(2.90 \pm 0.07) \times 10^3$	$(3.91 \pm 0.09) \times 10^3$	$(4.3 \pm 0.1) \times 10^3$	
N16	$(2.18 \pm 0.03) \times 10^1$	$(1.65 \pm 0.04) \times 10^1$	$(7.5 \pm 0.1) \times 10^2$	$(1.06 \pm 0.03) \times 10^3$	$(1.16 \pm 0.08) \times 10^3$	$(5.8 \pm 1.0) \times 10^2$	
N18	$(2.27 \pm 0.02) \times 10^2$	$(5.52 \pm 0.02) \times 10^2$	$(2.6 \pm 0.1) \times 10^3$	$(3.7 \pm 0.2) \times 10^3$	$(1.58 \pm 0.04) \times 10^4$	$(1.81 \pm 0.05) \times 10^4$	
N20	$(2.17 \pm 0.01) \times 10^1$	$(1.98 \pm 0.01) \times 10^1$	$(2.09 \pm 0.04) \times 10^2$	$(2.42 \pm 0.08) \times 10^2$	$(2.7 \pm 0.3) \times 10^2$	$(2.2 \pm 0.4) \times 10^2$	
N23	$(6.12 \pm 0.05) \times 10^0$	$(1.141 \pm 0.006) \times 10^1$	$(2.26 \pm 0.07) \times 10^2$	$(1.75 \pm 0.08) \times 10^2$	$(1.9 \pm 0.2) \times 10^2$	$(1.7 \pm 0.3) \times 10^2$	
N24	$(2.748 \pm 0.004) \times 10^3$	$(3.868 \pm 0.005) \times 10^3$	$(8.30 \pm 0.03) \times 10^4$	$(9.50 \pm 0.04) \times 10^4$	$(1.273 \pm 0.009) \times 10^5$	$(1.330 \pm 0.008) \times 10^5$	
N25	$(1.16 \pm 0.02) \times 10^1$	$(4.6 \pm 0.2) \times 10^0$	$(1.9 \pm 0.1) \times 10^2$	$(2.7 \pm 0.2) \times 10^2$	$(3.6 \pm 0.2) \times 10^2$	$(6.2 \pm 0.3) \times 10^2$	
N27	$(6.6 \pm 0.1) \times 10^0$	$(5.7 \pm 0.1) \times 10^0$	$(1.55 \pm 0.04) \times 10^2$	$(2.34 \pm 0.06) \times 10^2$	$(3.73 \pm 0.06) \times 10^2$	$(2.7 \pm 0.2) \times 10^2$	sc
N29	$(6.7 \pm 0.3) \times 10^1$	$(1.15 \pm 0.02) \times 10^2$	$(1.58 \pm 0.03) \times 10^3$	$(1.96 \pm 0.04) \times 10^3$	$(1.79 \pm 0.07) \times 10^3$	$(2.42 \pm 0.09) \times 10^3$	
N30	$(2.84 \pm 0.01) \times 10^1$	$(5.33 \pm 0.02) \times 10^1$	$(5.03 \pm 0.09) \times 10^2$	$(6.19 \pm 0.08) \times 10^2$	$(4.99 \pm 0.08) \times 10^2$	$(4.6 \pm 0.1) \times 10^2$	sc
N31	$(1.4 \pm 0.1) \times 10^0$	$(3.2 \pm 0.1) \times 10^0$	$(9.3 \pm 0.4) \times 10^1$	$(7.2 \pm 0.6) \times 10^1$	$(6.7 \pm 0.9) \times 10^1$	$(1.8 \pm 0.4) \times 10^1$	
N32	$(7.72 \pm 0.05) \times 10^0$	$(1.666 \pm 0.006) \times 10^1$	$(2.04 \pm 0.05) \times 10^2$	$(1.51 \pm 0.04) \times 10^2$	$(2.01 \pm 0.07) \times 10^2$	$(1.11 \pm 0.06) \times 10^2$	sc
N33	$(5.4 \pm 0.1) \times 10^0$	$(1.188 \pm 0.008) \times 10^1$	$(2.1 \pm 0.1) \times 10^2$	$(1.6 \pm 0.1) \times 10^2$	$(1.8 \pm 0.2) \times 10^2$	$(2.0 \pm 0.4) \times 10^2$	
N34	$(2.77 \pm 0.03) \times 10^1$	$(4.04 \pm 0.03) \times 10^1$	$(6.9 \pm 0.3) \times 10^2$	$(5.8 \pm 0.3) \times 10^2$	$(4.5 \pm 0.9) \times 10^2$	$(4.0 \pm 1.1) \times 10^2$	
N35	$(2.86 \pm 0.01) \times 10^2$	$(7.66 \pm 0.02) \times 10^2$	$(1.70 \pm 0.01) \times 10^4$	$(1.48 \pm 0.02) \times 10^4$	$(1.39 \pm 0.03) \times 10^4$	$(1.26 \pm 0.04) \times 10^4$	
N36	$(1.41 \pm 0.01) \times 10^2$	$(8.28 \pm 0.02) \times 10^2$	$(1.13 \pm 0.01) \times 10^4$	$(1.25 \pm 0.02) \times 10^4$	$(1.90 \pm 0.02) \times 10^4$	$(2.81 \pm 0.02) \times 10^4$	
N37	$(9.68 \pm 0.06) \times 10^1$	$(3.042 \pm 0.006) \times 10^2$	$(1.47 \pm 0.03) \times 10^3$	$(2.52 \pm 0.03) \times 10^3$	$(1.78 \pm 0.06) \times 10^3$	$(2.05 \pm 0.07) \times 10^3$	
N39	$(5.57 \pm 0.02) \times 10^2$	$(3.038 \pm 0.002) \times 10^3$	$(2.90 \pm 0.01) \times 10^4$	$(1.90 \pm 0.01) \times 10^4$	$(1.87 \pm 0.02) \times 10^4$	$(1.87 \pm 0.02) \times 10^4$	
N40	$(1.51 \pm 0.03) \times 10^1$	$(5.22 \pm 0.06) \times 10^1$	$(8.5 \pm 0.3) \times 10^2$	$(7.8 \pm 0.3) \times 10^2$	$(5.6 \pm 0.4) \times 10^2$	$(8.7 \pm 0.5) \times 10^2$	
N42	$(8.2 \pm 0.1) \times 10^0$	$(9.91 \pm 0.08) \times 10^0$	$(3.22 \pm 0.07) \times 10^2$	$(3.0 \pm 0.1) \times 10^2$	$(4.7 \pm 0.3) \times 10^2$	$(4.7 \pm 0.4) \times 10^2$	
N43	$(6.74 \pm 0.07) \times 10^0$	$(1.030 \pm 0.007) \times 10^1$	$(3.05 \pm 0.06) \times 10^2$	$(2.16 \pm 0.06) \times 10^2$	$(3.2 \pm 0.1) \times 10^2$	$(3.7 \pm 0.2) \times 10^2$	sc
N44	$(9.3 \pm 0.2) \times 10^0$	$(8.8 \pm 0.2) \times 10^0$	$(1.74 \pm 0.04) \times 10^2$	$(1.88 \pm 0.05) \times 10^2$	$(4.9 \pm 0.2) \times 10^2$	$(5.4 \pm 0.2) \times 10^2$	
N45	$(4.31 \pm 0.02) \times 10^1$	$(7.26 \pm 0.02) \times 10^1$	$(1.178 \pm 0.009) \times 10^3$	$(1.194 \pm 0.007) \times 10^3$	$(1.27 \pm 0.02) \times 10^3$	$(1.11 \pm 0.03) \times 10^3$	sc
N46	$(7.3 \pm 0.2) \times 10^0$	$(1.73 \pm 0.03) \times 10^1$	$(2.8 \pm 0.2) \times 10^2$	$(3.0 \pm 0.2) \times 10^2$	$(1.7 \pm 0.5) \times 10^2$	$(3.9 \pm 0.5) \times 10^2$	
N47	$(3.73 \pm 0.03) \times 10^1$	$(8.07 \pm 0.04) \times 10^1$	$(1.58 \pm 0.02) \times 10^3$	$(2.64 \pm 0.03) \times 10^3$	$(6.44 \pm 0.09) \times 10^3$	$(7.03 \pm 0.09) \times 10^3$	sc
N48	$(1.13 \pm 0.01) \times 10^1$	$(8.5 \pm 0.1) \times 10^0$	$(3.06 \pm 0.03) \times 10^2$	$(3.76 \pm 0.02) \times 10^2$	$(6.4 \pm 0.2) \times 10^2$	$(5.8 \pm 0.1) \times 10^2$	sc
N49	$(4.70 \pm 0.03) \times 10^1$	$(9.61 \pm 0.02) \times 10^1$	$(1.93 \pm 0.01) \times 10^3$	$(2.03 \pm 0.02) \times 10^3$	$(3.25 \pm 0.06) \times 10^3$	$(2.79 \pm 0.07) \times 10^3$	

Continued.

Name	Flux 9 μm [Jy]	Flux 18 μm [Jy]	Flux 65 μm [Jy]	Flux 90 μm [Jy]	Flux 140 μm [Jy]	Flux 160 μm [Jy]	Notes
N50	$(1.08 \pm 0.04) \times 10^1$	$(2.05 \pm 0.03) \times 10^1$	$(7.2 \pm 0.1) \times 10^2$	$(7.7 \pm 0.3) \times 10^2$	$(6.1 \pm 0.7) \times 10^2$	$(3.9 \pm 0.8) \times 10^2$	
N51	$(3.87 \pm 0.02) \times 10^1$	$(2.56 \pm 0.03) \times 10^1$	$(6.90 \pm 0.05) \times 10^2$	$(1.035 \pm 0.002) \times 10^3$	$(4.5 \pm 0.2) \times 10^2$	$(5.7 \pm 0.3) \times 10^2$	sc
N52	$(7.10 \pm 0.02) \times 10^2$	$(4.799 \pm 0.004) \times 10^3$	$(7.26 \pm 0.04) \times 10^4$	$(4.06 \pm 0.03) \times 10^4$	$(5.11 \pm 0.06) \times 10^4$	$(5.87 \pm 0.07) \times 10^4$	
N53	$(1.13 \pm 0.01) \times 10^1$	$(1.58 \pm 0.04) \times 10^1$	$(4.0 \pm 0.2) \times 10^2$	$(3.4 \pm 0.2) \times 10^2$	$(4.9 \pm 0.3) \times 10^2$	$(5.8 \pm 0.4) \times 10^2$	
N54	$(4.28 \pm 0.03) \times 10^1$	$(5.77 \pm 0.03) \times 10^1$	$(1.14 \pm 0.01) \times 10^3$	$(1.10 \pm 0.01) \times 10^3$	$(1.23 \pm 0.05) \times 10^3$	$(5.7 \pm 0.6) \times 10^2$	
N56	$(1.32 \pm 0.03) \times 10^1$	$(1.05 \pm 0.02) \times 10^1$	$(1.37 \pm 0.06) \times 10^2$	$(2.15 \pm 0.08) \times 10^2$	$(5.7 \pm 0.3) \times 10^2$	$(6.5 \pm 0.3) \times 10^2$	
N57	$(1.12 \pm 0.03) \times 10^0$	$(1.43 \pm 0.03) \times 10^0$	$(1.42 \pm 0.08) \times 10^1$	$(3.5 \pm 0.1) \times 10^1$	$(4.5 \pm 0.4) \times 10^1$	$(5.9 \pm 0.4) \times 10^1$	sc
N58	$(4.44 \pm 0.04) \times 10^0$	$(1.311 \pm 0.004) \times 10^1$	$(3.7 \pm 0.1) \times 10^2$	$(2.6 \pm 0.1) \times 10^2$	$(2.1 \pm 0.1) \times 10^2$	$(2.6 \pm 0.1) \times 10^2$	
N59	$(4.98 \pm 0.02) \times 10^2$	$(5.54 \pm 0.02) \times 10^2$	$(1.00 \pm 0.01) \times 10^4$	$(1.66 \pm 0.02) \times 10^4$	$(2.73 \pm 0.04) \times 10^4$	$(2.53 \pm 0.04) \times 10^4$	
N62	$(3.02 \pm 0.01) \times 10^1$	$(3.96 \pm 0.01) \times 10^1$	$(8.10 \pm 0.06) \times 10^2$	$(1.046 \pm 0.008) \times 10^3$	$(1.23 \pm 0.02) \times 10^3$	$(1.26 \pm 0.02) \times 10^3$	sc
N64	$(6.73 \pm 0.09) \times 10^1$	$(1.047 \pm 0.009) \times 10^2$	$(2.29 \pm 0.03) \times 10^3$	$(3.56 \pm 0.05) \times 10^3$	$(6.06 \pm 0.09) \times 10^3$	$(6.2 \pm 0.1) \times 10^3$	
N65	$(5.34 \pm 0.04) \times 10^1$	$(5.25 \pm 0.03) \times 10^1$	$(2.65 \pm 0.02) \times 10^3$	$(3.15 \pm 0.03) \times 10^3$	$(4.90 \pm 0.06) \times 10^3$	$(4.36 \pm 0.07) \times 10^3$	
N66	$(1.71 \pm 0.03) \times 10^0$	$(1.49 \pm 0.04) \times 10^0$	$(3.1 \pm 0.2) \times 10^1$	$(4.7 \pm 0.2) \times 10^1$	$(6.8 \pm 0.8) \times 10^1$	$(7.2 \pm 1.3) \times 10^1$	
N69	$(1.671 \pm 0.007) \times 10^2$	$(2.028 \pm 0.007) \times 10^2$	$(2.73 \pm 0.01) \times 10^3$	$(5.47 \pm 0.02) \times 10^3$	$(1.324 \pm 0.007) \times 10^4$	$(1.333 \pm 0.008) \times 10^4$	
N70	$(4.03 \pm 0.08) \times 10^0$	$(1.444 \pm 0.006) \times 10^1$	$(3.2 \pm 0.1) \times 10^2$	$(3.1 \pm 0.1) \times 10^2$	$(2.6 \pm 0.3) \times 10^2$	$(3.4 \pm 0.3) \times 10^2$	
N71	$(4.278 \pm 0.009) \times 10^2$	$(4.085 \pm 0.009) \times 10^2$	$(1.199 \pm 0.003) \times 10^4$	$(2.198 \pm 0.007) \times 10^4$	$(4.16 \pm 0.02) \times 10^4$	$(4.73 \pm 0.02) \times 10^4$	sc
N72	$(9.96 \pm 0.05) \times 10^0$	$(7.49 \pm 0.07) \times 10^0$	$(1.48 \pm 0.05) \times 10^2$	$(3.70 \pm 0.02) \times 10^2$	$(1.1 \pm 0.2) \times 10^2$	$(2.9 \pm 0.1) \times 10^2$	sc
N73	$(1.065 \pm 0.008) \times 10^1$	$(8.64 \pm 0.08) \times 10^0$	$(3.07 \pm 0.03) \times 10^2$	$(4.19 \pm 0.05) \times 10^2$	$(6.3 \pm 0.2) \times 10^2$	$(5.4 \pm 0.3) \times 10^2$	
N75	$(1.83 \pm 0.07) \times 10^1$	$(1.69 \pm 0.05) \times 10^1$	$(3.8 \pm 0.3) \times 10^2$	$(3.8 \pm 0.4) \times 10^2$	$(4.4 \pm 0.5) \times 10^2$	$(3.6 \pm 0.6) \times 10^2$	
N77	$(1.218 \pm 0.005) \times 10^1$	$(8.15 \pm 0.06) \times 10^0$	$(1.37 \pm 0.01) \times 10^2$	$(1.72 \pm 0.01) \times 10^2$	$(2.63 \pm 0.03) \times 10^2$	$(2.35 \pm 0.03) \times 10^2$	sc
N78	$(1.56 \pm 0.03) \times 10^0$	$(1.61 \pm 0.03) \times 10^0$	$(1.8 \pm 0.1) \times 10^1$	$(2.1 \pm 0.1) \times 10^1$	$(2.6 \pm 0.2) \times 10^1$	$(3.0 \pm 0.4) \times 10^1$	
N79	$(1.696 \pm 0.009) \times 10^1$	$(2.93 \pm 0.01) \times 10^1$	$(6.29 \pm 0.07) \times 10^2$	$(7.95 \pm 0.08) \times 10^2$	$(9.8 \pm 0.2) \times 10^2$	$(7.5 \pm 0.3) \times 10^2$	
N80	$(3.2 \pm 0.2) \times 10^0$	$(8.7 \pm 0.2) \times 10^0$	$(1.88 \pm 0.05) \times 10^2$	$(2.02 \pm 0.06) \times 10^2$	$(3.0 \pm 0.2) \times 10^2$	$(2.3 \pm 0.3) \times 10^2$	
N81	$(3.363 \pm 0.004) \times 10^2$	$(3.928 \pm 0.006) \times 10^2$	$(6.751 \pm 0.009) \times 10^3$	$(1.406 \pm 0.001) \times 10^4$	$(3.167 \pm 0.004) \times 10^4$	$(3.280 \pm 0.005) \times 10^4$	sc
N82	$(1.105 \pm 0.002) \times 10^2$	$(1.657 \pm 0.002) \times 10^2$	$(2.76 \pm 0.01) \times 10^3$	$(3.15 \pm 0.01) \times 10^3$	$(3.29 \pm 0.04) \times 10^3$	$(2.60 \pm 0.04) \times 10^3$	
N83	$(7.03 \pm 0.05) \times 10^0$	$(2.255 \pm 0.007) \times 10^1$	$(1.61 \pm 0.06) \times 10^2$	$(1.42 \pm 0.08) \times 10^2$	$(8.1 \pm 0.9) \times 10^1$	$(9.8 \pm 1.0) \times 10^1$	
N84	$(2.918 \pm 0.007) \times 10^1$	$(2.378 \pm 0.008) \times 10^1$	$(5.45 \pm 0.02) \times 10^2$	$(6.50 \pm 0.03) \times 10^2$	$(7.10 \pm 0.09) \times 10^2$	$(7.7 \pm 0.1) \times 10^2$	sc
N89	$(6.50 \pm 0.06) \times 10^0$	$(6.99 \pm 0.07) \times 10^0$	$(9.8 \pm 0.2) \times 10^1$	$(1.57 \pm 0.02) \times 10^2$	$(2.06 \pm 0.04) \times 10^2$	$(1.77 \pm 0.04) \times 10^2$	sc
N90	$(1.02 \pm 0.02) \times 10^1$	$(1.30 \pm 0.02) \times 10^1$	$(1.83 \pm 0.06) \times 10^2$	$(2.57 \pm 0.09) \times 10^2$	$(2.8 \pm 0.1) \times 10^2$	$(2.7 \pm 0.1) \times 10^2$	
N91	$(1.461 \pm 0.004) \times 10^2$	$(1.546 \pm 0.005) \times 10^2$	$(2.235 \pm 0.009) \times 10^3$	$(3.38 \pm 0.02) \times 10^3$	$(5.40 \pm 0.04) \times 10^3$	$(4.37 \pm 0.04) \times 10^3$	sc
N92	$(4.14 \pm 0.02) \times 10^1$	$(2.58 \pm 0.02) \times 10^1$	$(4.73 \pm 0.03) \times 10^2$	$(7.29 \pm 0.04) \times 10^2$	$(9.8 \pm 0.1) \times 10^2$	$(8.9 \pm 0.1) \times 10^2$	
N95	$(2.12 \pm 0.01) \times 10^1$	$(3.42 \pm 0.01) \times 10^1$	$(4.02 \pm 0.05) \times 10^2$	$(5.05 \pm 0.06) \times 10^2$	$(6.6 \pm 0.1) \times 10^2$	$(5.8 \pm 0.2) \times 10^2$	
N96	$(1.71 \pm 0.02) \times 10^0$	$(3.95 \pm 0.03) \times 10^0$	$(2.85 \pm 0.05) \times 10^1$	$(3.7 \pm 0.1) \times 10^1$	$(3.2 \pm 0.1) \times 10^1$	$(3.3 \pm 0.1) \times 10^1$	sc
N98	$(2.34 \pm 0.02) \times 10^1$	$(2.42 \pm 0.02) \times 10^1$	$(3.74 \pm 0.03) \times 10^2$	$(5.48 \pm 0.05) \times 10^2$	$(7.9 \pm 0.1) \times 10^2$	$(7.6 \pm 0.1) \times 10^2$	

Continued.

Name	Flux 9 μm [Jy]	Flux 18 μm [Jy]	Flux 65 μm [Jy]	Flux 90 μm [Jy]	Flux 140 μm [Jy]	Flux 160 μm [Jy]	Notes
N101	$(1.454 \pm 0.009) \times 10^2$	$(7.14 \pm 0.01) \times 10^2$	$(1.19 \pm 0.01) \times 10^4$	$(5.8 \pm 0.1) \times 10^3$	$(4.2 \pm 0.2) \times 10^3$	$(5.2 \pm 0.2) \times 10^3$	
N104	$(9.46 \pm 0.09) \times 10^0$	$(6.71 \pm 0.08) \times 10^0$	$(1.06 \pm 0.03) \times 10^2$	$(2.22 \pm 0.03) \times 10^2$	$(2.79 \pm 0.06) \times 10^2$	$(2.14 \pm 0.07) \times 10^2$	
N105	$(1.70 \pm 0.01) \times 10^1$	$(1.67 \pm 0.01) \times 10^1$	$(2.45 \pm 0.08) \times 10^2$	$(3.5 \pm 0.1) \times 10^2$	$(5.3 \pm 0.2) \times 10^2$	$(4.9 \pm 0.2) \times 10^2$	
N106	$(3.48 \pm 0.05) \times 10^0$	$(2.3 \pm 0.1) \times 10^0$	$(4.5 \pm 0.3) \times 10^1$	$(5.7 \pm 0.6) \times 10^1$	$(7.2 \pm 0.7) \times 10^1$	$(4.4 \pm 1.1) \times 10^1$	
N107	$(6.241 \pm 0.007) \times 10^2$	$(7.20 \pm 0.01) \times 10^2$	$(1.182 \pm 0.002) \times 10^4$	$(1.831 \pm 0.003) \times 10^4$	$(2.894 \pm 0.008) \times 10^4$	$(2.969 \pm 0.007) \times 10^4$	sc
N109	$(6.09 \pm 0.03) \times 10^2$	$(3.97 \pm 0.03) \times 10^2$	$(1.004 \pm 0.007) \times 10^4$	$(1.57 \pm 0.01) \times 10^4$	$(2.68 \pm 0.03) \times 10^4$	$(2.52 \pm 0.03) \times 10^4$	
N110	$(7.26 \pm 0.04) \times 10^0$	$(5.66 \pm 0.04) \times 10^0$	$(7.5 \pm 0.1) \times 10^1$	$(1.28 \pm 0.01) \times 10^2$	$(1.25 \pm 0.02) \times 10^2$	$(2.16 \pm 0.03) \times 10^2$	sc
N111	$(3.009 \pm 0.009) \times 10^1$	$(5.810 \pm 0.006) \times 10^1$	$(7.801 \pm 0.009) \times 10^2$	$(9.03 \pm 0.02) \times 10^2$	$(8.58 \pm 0.08) \times 10^2$	$(8.85 \pm 0.08) \times 10^2$	sc
N113	$(1.45 \pm 0.03) \times 10^1$	$(3.48 \pm 0.06) \times 10^1$	$(4.1 \pm 0.2) \times 10^2$	$(4.0 \pm 0.2) \times 10^2$	$(3.9 \pm 0.2) \times 10^2$	$(3.7 \pm 0.2) \times 10^2$	
N114	$(4.33 \pm 0.04) \times 10^1$	$(7.71 \pm 0.05) \times 10^1$	$(9.4 \pm 0.3) \times 10^2$	$(1.06 \pm 0.04) \times 10^3$	$(1.42 \pm 0.04) \times 10^3$	$(1.38 \pm 0.05) \times 10^3$	
N115	$(3.869 \pm 0.005) \times 10^2$	$(3.042 \pm 0.004) \times 10^2$	$(6.02 \pm 0.02) \times 10^3$	$(7.71 \pm 0.02) \times 10^3$	$(7.43 \pm 0.04) \times 10^3$	$(6.77 \pm 0.04) \times 10^3$	
N116	$(3.488 \pm 0.008) \times 10^1$	$(7.894 \pm 0.007) \times 10^1$	$(1.195 \pm 0.004) \times 10^3$	$(1.323 \pm 0.005) \times 10^3$	$(1.313 \pm 0.005) \times 10^3$	$(8.89 \pm 0.08) \times 10^2$	sc
N117	$(1.025 \pm 0.003) \times 10^2$	$(1.591 \pm 0.003) \times 10^2$	$(2.71 \pm 0.02) \times 10^3$	$(3.42 \pm 0.02) \times 10^3$	$(4.01 \pm 0.02) \times 10^3$	$(3.15 \pm 0.02) \times 10^3$	
N120	$(3.40 \pm 0.09) \times 10^0$	$(4.2 \pm 0.1) \times 10^0$	$(5.4 \pm 0.3) \times 10^1$	$(5.8 \pm 0.4) \times 10^1$	$(1.20 \pm 0.09) \times 10^2$	$(8.8 \pm 1.0) \times 10^1$	
N122	$(8.58 \pm 0.05) \times 10^0$	$(8.52 \pm 0.04) \times 10^0$	$(1.14 \pm 0.01) \times 10^2$	$(1.30 \pm 0.02) \times 10^2$	$(1.18 \pm 0.02) \times 10^2$	$(8.5 \pm 0.2) \times 10^1$	sc
N123	$(3.173 \pm 0.008) \times 10^1$	$(7.23 \pm 0.01) \times 10^1$	$(8.13 \pm 0.03) \times 10^2$	$(8.03 \pm 0.05) \times 10^2$	$(7.33 \pm 0.09) \times 10^2$	$(6.1 \pm 0.1) \times 10^2$	
N124	$(1.129 \pm 0.008) \times 10^1$	$(7.2 \pm 0.1) \times 10^0$	$(8.9 \pm 0.1) \times 10^1$	$(1.38 \pm 0.02) \times 10^2$	$(2.88 \pm 0.06) \times 10^2$	$(2.73 \pm 0.06) \times 10^2$	
N125	$(1.607 \pm 0.003) \times 10^1$	$(3.121 \pm 0.005) \times 10^1$	$(3.69 \pm 0.01) \times 10^2$	$(4.95 \pm 0.02) \times 10^2$	$(2.52 \pm 0.05) \times 10^2$	$(4.06 \pm 0.04) \times 10^2$	sc
N126	$(1.17 \pm 0.02) \times 10^1$	$(1.04 \pm 0.01) \times 10^1$	$(8.0 \pm 0.3) \times 10^1$	$(1.00 \pm 0.03) \times 10^2$	$(9.4 \pm 0.7) \times 10^1$	$(1.17 \pm 0.08) \times 10^2$	
N127	$(1.90 \pm 0.02) \times 10^1$	$(1.68 \pm 0.03) \times 10^1$	$(1.76 \pm 0.02) \times 10^2$	$(2.71 \pm 0.02) \times 10^2$	$(6.40 \pm 0.04) \times 10^2$	$(6.45 \pm 0.07) \times 10^2$	sc
N130	$(3.92 \pm 0.06) \times 10^0$	$(2.3 \pm 0.1) \times 10^0$	$(2.6 \pm 0.1) \times 10^1$	$(4.53 \pm 0.06) \times 10^1$	$(1.20 \pm 0.02) \times 10^2$	$(1.03 \pm 0.03) \times 10^2$	
N131	$(1.70 \pm 0.03) \times 10^1$	$(1.51 \pm 0.05) \times 10^1$	$(5.58 \pm 0.08) \times 10^2$	$(6.7 \pm 0.1) \times 10^2$	$(9.8 \pm 0.2) \times 10^2$	$(1.02 \pm 0.02) \times 10^3$	
N133	$(1.177 \pm 0.006) \times 10^2$	$(2.504 \pm 0.005) \times 10^2$	$(3.57 \pm 0.03) \times 10^3$	$(3.36 \pm 0.04) \times 10^3$	$(3.01 \pm 0.05) \times 10^3$	$(2.34 \pm 0.06) \times 10^3$	
N134	$(6.80 \pm 0.01) \times 10^1$	$(1.188 \pm 0.001) \times 10^2$	$(2.03 \pm 0.02) \times 10^3$	$(1.37 \pm 0.02) \times 10^3$	$(9.4 \pm 0.1) \times 10^2$	$(8.3 \pm 0.1) \times 10^2$	sc
S186	$(2.308 \pm 0.004) \times 10^2$	$(8.302 \pm 0.005) \times 10^2$	$(1.140 \pm 0.002) \times 10^4$	$(1.290 \pm 0.003) \times 10^4$	$(1.225 \pm 0.006) \times 10^4$	$(1.100 \pm 0.006) \times 10^4$	
S181	$(5.097 \pm 0.002) \times 10^2$	$(3.458 \pm 0.001) \times 10^3$	$(2.452 \pm 0.003) \times 10^4$	$(1.416 \pm 0.003) \times 10^4$	$(1.031 \pm 0.002) \times 10^4$	$(8.21 \pm 0.02) \times 10^3$	sc
S163	$(2.92 \pm 0.02) \times 10^1$	$(3.34 \pm 0.02) \times 10^1$	$(6.54 \pm 0.06) \times 10^2$	$(1.02 \pm 0.01) \times 10^3$	$(1.68 \pm 0.03) \times 10^3$	$(1.71 \pm 0.03) \times 10^3$	
S156	$(5.02 \pm 0.04) \times 10^2$	$(3.31 \pm 0.02) \times 10^3$	$(2.5 \pm 0.1) \times 10^4$	$(1.39 \pm 0.06) \times 10^4$	$(9.6 \pm 0.6) \times 10^3$	$(3.1 \pm 0.4) \times 10^3$	
S155	$(7.16 \pm 0.03) \times 10^1$	$(3.372 \pm 0.006) \times 10^2$	$(3.25 \pm 0.07) \times 10^3$	$(1.17 \pm 0.04) \times 10^3$	$(1.30 \pm 0.07) \times 10^3$	$(1.29 \pm 0.08) \times 10^3$	sc
S150	$(6.52 \pm 0.04) \times 10^1$	$(1.789 \pm 0.004) \times 10^2$	$(2.22 \pm 0.04) \times 10^3$	$(2.03 \pm 0.04) \times 10^3$	$(2.31 \pm 0.07) \times 10^3$	$(2.58 \pm 0.07) \times 10^3$	
S149	$(5.13 \pm 0.05) \times 10^1$	$(1.97 \pm 0.02) \times 10^2$	$(2.39 \pm 0.07) \times 10^3$	$(9.1 \pm 0.5) \times 10^2$	$(7.8 \pm 0.8) \times 10^2$	$(8.2 \pm 0.6) \times 10^2$	sc
S145	$(6.538 \pm 0.005) \times 10^2$	$(1.138 \pm 0.001) \times 10^3$	$(2.219 \pm 0.001) \times 10^4$	$(2.411 \pm 0.002) \times 10^4$	$(2.167 \pm 0.003) \times 10^4$	$(1.718 \pm 0.004) \times 10^4$	sc
S144	$(4.21 \pm 0.07) \times 10^1$	$(8.80 \pm 0.03) \times 10^1$	$(1.96 \pm 0.01) \times 10^3$	$(1.16 \pm 0.01) \times 10^3$	$(1.40 \pm 0.01) \times 10^3$	$(1.267 \pm 0.009) \times 10^3$	sc
S143	$(5.960 \pm 0.008) \times 10^2$	$(6.448 \pm 0.005) \times 10^2$	$(1.136 \pm 0.003) \times 10^4$	$(1.289 \pm 0.005) \times 10^4$	$(1.50 \pm 0.01) \times 10^4$	$(1.41 \pm 0.02) \times 10^4$	

Continued.

Name	Flux 9 μm [Jy]	Flux 18 μm [Jy]	Flux 65 μm [Jy]	Flux 90 μm [Jy]	Flux 140 μm [Jy]	Flux 160 μm [Jy]	Notes
S141	$(6.523 \pm 0.007) \times 10^1$	$(1.390 \pm 0.001) \times 10^2$	$(1.965 \pm 0.003) \times 10^3$	$(2.126 \pm 0.004) \times 10^3$	$(1.917 \pm 0.004) \times 10^3$	$(1.796 \pm 0.005) \times 10^3$	sc
S138	$(7.4 \pm 0.1) \times 10^0$	$(1.76 \pm 0.01) \times 10^1$	$(4.4 \pm 0.2) \times 10^2$	$(4.6 \pm 0.2) \times 10^2$	$(2.8 \pm 0.3) \times 10^2$	$(1.9 \pm 0.3) \times 10^2$	
S137	$(1.768 \pm 0.006) \times 10^2$	$(1.431 \pm 0.003) \times 10^2$	$(1.96 \pm 0.04) \times 10^3$	$(2.89 \pm 0.05) \times 10^3$	$(3.2 \pm 0.1) \times 10^3$	$(4.6 \pm 0.1) \times 10^3$	
S136	$(1.64 \pm 0.01) \times 10^1$	$(6.4 \pm 0.2) \times 10^0$	$(1.98 \pm 0.08) \times 10^2$	$(3.8 \pm 0.1) \times 10^2$	$(3.5 \pm 0.2) \times 10^2$	$(4.8 \pm 0.3) \times 10^2$	
S135	$(1.9 \pm 0.1) \times 10^0$	$(1.19 \pm 0.02) \times 10^1$	$(1.67 \pm 0.07) \times 10^2$	$(1.1 \pm 0.1) \times 10^2$	$(9.9 \pm 0.5) \times 10^1$	$(1.2 \pm 0.1) \times 10^2$	sc
S134	$(2.38 \pm 0.03) \times 10^1$	$(3.59 \pm 0.08) \times 10^1$	$(1.15 \pm 0.04) \times 10^3$	$(7.5 \pm 0.3) \times 10^2$	$(6.0 \pm 0.5) \times 10^2$	$(6.9 \pm 0.5) \times 10^2$	
S133	$(1.151 \pm 0.007) \times 10^2$	$(2.032 \pm 0.005) \times 10^2$	$(5.08 \pm 0.05) \times 10^3$	$(4.74 \pm 0.07) \times 10^3$	$(4.2 \pm 0.1) \times 10^3$	$(4.0 \pm 0.1) \times 10^3$	
S132	$(2.1 \pm 0.2) \times 10^0$	$(2.8 \pm 0.4) \times 10^0$	$(1.0 \pm 0.2) \times 10^2$	$(1.0 \pm 0.1) \times 10^2$	$(1.8 \pm 0.2) \times 10^2$	$(2.1 \pm 0.2) \times 10^2$	
S123	$(5.31 \pm 0.03) \times 10^1$	$(2.74 \pm 0.02) \times 10^1$	$(8.7 \pm 0.1) \times 10^2$	$(1.43 \pm 0.02) \times 10^3$	$(2.00 \pm 0.03) \times 10^3$	$(1.92 \pm 0.03) \times 10^3$	
S116	$(2.434 \pm 0.002) \times 10^2$	$(4.979 \pm 0.002) \times 10^2$	$(7.469 \pm 0.005) \times 10^3$	$(8.727 \pm 0.007) \times 10^3$	$(1.169 \pm 0.001) \times 10^4$	$(9.06 \pm 0.03) \times 10^3$	sc
S115	$(3.26 \pm 0.05) \times 10^0$	$(2.74 \pm 0.04) \times 10^0$	$(6.8 \pm 0.1) \times 10^1$	$(8.8 \pm 0.1) \times 10^1$	$(1.99 \pm 0.07) \times 10^2$	$(2.31 \pm 0.09) \times 10^2$	
S104	$(4.26 \pm 0.03) \times 10^1$	$(9.56 \pm 0.08) \times 10^1$	$(1.73 \pm 0.02) \times 10^3$	$(1.73 \pm 0.02) \times 10^3$	$(1.07 \pm 0.02) \times 10^3$	$(9.3 \pm 0.2) \times 10^2$	
S96	$(2.320 \pm 0.007) \times 10^2$	$(5.342 \pm 0.009) \times 10^2$	$(7.65 \pm 0.05) \times 10^3$	$(6.10 \pm 0.05) \times 10^3$	$(6.80 \pm 0.06) \times 10^3$	$(5.86 \pm 0.06) \times 10^3$	
S92	$(3.225 \pm 0.005) \times 10^2$	$(5.064 \pm 0.005) \times 10^2$	$(8.97 \pm 0.02) \times 10^3$	$(1.214 \pm 0.002) \times 10^4$	$(1.660 \pm 0.004) \times 10^4$	$(1.685 \pm 0.004) \times 10^4$	sc
S91	$(5.26 \pm 0.06) \times 10^1$	$(2.9 \pm 0.1) \times 10^1$	$(8.3 \pm 0.5) \times 10^2$	$(1.39 \pm 0.05) \times 10^3$	$(2.96 \pm 0.06) \times 10^3$	$(3.30 \pm 0.07) \times 10^3$	
S84	$(1.07 \pm 0.01) \times 10^1$	$(2.06 \pm 0.01) \times 10^1$	$(3.1 \pm 0.1) \times 10^2$	$(2.4 \pm 0.1) \times 10^2$	$(1.3 \pm 0.1) \times 10^2$	$(1.4 \pm 0.1) \times 10^2$	
S76	$(2.885 \pm 0.007) \times 10^2$	$(1.444 \pm 0.001) \times 10^3$	$(2.261 \pm 0.003) \times 10^4$	$(2.348 \pm 0.005) \times 10^4$	$(1.965 \pm 0.009) \times 10^4$	$(1.96 \pm 0.01) \times 10^4$	sc
S74	$(2.4 \pm 0.1) \times 10^1$	$(5.90 \pm 0.08) \times 10^1$	$(1.14 \pm 0.04) \times 10^3$	$(9.8 \pm 0.4) \times 10^2$	$(8.0 \pm 0.4) \times 10^2$	$(8.0 \pm 0.6) \times 10^2$	
S73	$(3.025 \pm 0.005) \times 10^2$	$(2.843 \pm 0.004) \times 10^2$	$(4.78 \pm 0.01) \times 10^3$	$(6.24 \pm 0.02) \times 10^3$	$(6.26 \pm 0.03) \times 10^3$	$(6.68 \pm 0.03) \times 10^3$	sc
S71	$(8.3 \pm 0.2) \times 10^1$	$(1.96 \pm 0.02) \times 10^2$	$(3.00 \pm 0.05) \times 10^3$	$(2.29 \pm 0.05) \times 10^3$	$(1.97 \pm 0.06) \times 10^3$	$(1.86 \pm 0.05) \times 10^3$	
S70	$(4.232 \pm 0.009) \times 10^1$	$(6.11 \pm 0.01) \times 10^1$	$(1.384 \pm 0.005) \times 10^3$	$(1.350 \pm 0.005) \times 10^3$	$(1.51 \pm 0.01) \times 10^3$	$(1.70 \pm 0.01) \times 10^3$	sc
S67	$(4.31 \pm 0.04) \times 10^1$	$(1.205 \pm 0.004) \times 10^2$	$(1.77 \pm 0.04) \times 10^3$	$(1.51 \pm 0.04) \times 10^3$	$(1.72 \pm 0.06) \times 10^3$	$(1.69 \pm 0.06) \times 10^3$	
S66	$(1.272 \pm 0.001) \times 10^3$	$(2.121 \pm 0.001) \times 10^3$	$(5.262 \pm 0.005) \times 10^4$	$(5.795 \pm 0.007) \times 10^4$	$(9.642 \pm 0.008) \times 10^4$	$(8.810 \pm 0.008) \times 10^4$	sc
S65	$(6.3 \pm 0.1) \times 10^0$	$(5.2 \pm 1.3) \times 10^{-1}$	$(8.4 \pm 0.8) \times 10^1$	$(8.5 \pm 0.6) \times 10^1$	$(3.1 \pm 1.0) \times 10^1$	$(3.8 \pm 0.9) \times 10^1$	
S64	$(2.039 \pm 0.007) \times 10^2$	$(6.387 \pm 0.006) \times 10^2$	$(3.064 \pm 0.002) \times 10^4$	$(2.276 \pm 0.002) \times 10^4$	$(2.340 \pm 0.008) \times 10^4$	$(2.711 \pm 0.009) \times 10^4$	sc
S62	$(1.62 \pm 0.01) \times 10^2$	$(5.80 \pm 0.01) \times 10^2$	$(6.67 \pm 0.07) \times 10^3$	$(6.8 \pm 0.1) \times 10^3$	$(7.8 \pm 0.1) \times 10^3$	$(5.4 \pm 0.1) \times 10^3$	
S54	$(5.49 \pm 0.02) \times 10^1$	$(6.76 \pm 0.01) \times 10^1$	$(1.132 \pm 0.006) \times 10^3$	$(1.21 \pm 0.01) \times 10^3$	$(1.52 \pm 0.02) \times 10^3$	$(1.50 \pm 0.03) \times 10^3$	sc
S51	$(3.08 \pm 0.02) \times 10^2$	$(1.433 \pm 0.006) \times 10^3$	$(1.97 \pm 0.03) \times 10^4$	$(1.18 \pm 0.02) \times 10^4$	$(1.43 \pm 0.02) \times 10^4$	$(1.69 \pm 0.02) \times 10^4$	
S44	$(8.72 \pm 0.03) \times 10^1$	$(1.329 \pm 0.003) \times 10^2$	$(1.975 \pm 0.006) \times 10^3$	$(2.357 \pm 0.009) \times 10^3$	$(2.97 \pm 0.03) \times 10^3$	$(2.81 \pm 0.04) \times 10^3$	
S41	$(3.990 \pm 0.009) \times 10^2$	$(1.156 \pm 0.001) \times 10^3$	$(2.556 \pm 0.008) \times 10^4$	$(2.147 \pm 0.008) \times 10^4$	$(2.01 \pm 0.02) \times 10^4$	$(2.83 \pm 0.02) \times 10^4$	sc
S37	$(9.43 \pm 0.04) \times 10^1$	$(1.209 \pm 0.003) \times 10^2$	$(2.83 \pm 0.02) \times 10^3$	$(2.44 \pm 0.03) \times 10^3$	$(2.58 \pm 0.04) \times 10^3$	$(2.64 \pm 0.05) \times 10^3$	
S36	$(5.17 \pm 0.01) \times 10^2$	$(2.971 \pm 0.002) \times 10^3$	$(4.053 \pm 0.006) \times 10^4$	$(2.729 \pm 0.009) \times 10^4$	$(3.64 \pm 0.02) \times 10^4$	$(3.37 \pm 0.02) \times 10^4$	
S34	$(4.75 \pm 0.05) \times 10^0$	$(3.03 \pm 0.02) \times 10^1$	$(4.9 \pm 0.1) \times 10^2$	$(2.73 \pm 0.04) \times 10^2$	$(4.1 \pm 0.1) \times 10^2$	$(5.8 \pm 0.2) \times 10^2$	sc
S29	$(3.856 \pm 0.004) \times 10^2$	$(1.148 \pm 0.001) \times 10^3$	$(1.230 \pm 0.002) \times 10^4$	$(1.601 \pm 0.004) \times 10^4$	$(1.593 \pm 0.005) \times 10^4$	$(1.848 \pm 0.004) \times 10^4$	sc

Continued.

Name	Flux 9 μm [Jy]	Flux 18 μm [Jy]	Flux 65 μm [Jy]	Flux 90 μm [Jy]	Flux 140 μm [Jy]	Flux 160 μm [Jy]	Notes
S24	$(2.01 \pm 0.03) \times 10^1$	$(5.96 \pm 0.06) \times 10^1$	$(7.2 \pm 0.5) \times 10^2$	$(3.7 \pm 0.4) \times 10^2$	$(4.3 \pm 0.6) \times 10^2$	$(4.9 \pm 0.8) \times 10^2$	
S23	$(8.41 \pm 0.03) \times 10^1$	$(1.326 \pm 0.003) \times 10^2$	$(3.395 \pm 0.010) \times 10^3$	$(3.69 \pm 0.01) \times 10^3$	$(4.80 \pm 0.04) \times 10^3$	$(5.66 \pm 0.04) \times 10^3$	sc
S20	$(3.56 \pm 0.03) \times 10^1$	$(1.439 \pm 0.005) \times 10^2$	$(1.71 \pm 0.03) \times 10^3$	$(1.51 \pm 0.04) \times 10^3$	$(1.74 \pm 0.06) \times 10^3$	$(1.36 \pm 0.07) \times 10^3$	
S18	$(5.39 \pm 0.01) \times 10^1$	$(1.695 \pm 0.001) \times 10^2$	$(2.542 \pm 0.002) \times 10^3$	$(2.383 \pm 0.005) \times 10^3$	$(3.29 \pm 0.02) \times 10^3$	$(3.44 \pm 0.02) \times 10^3$	sc
S17	$(4.21 \pm 0.01) \times 10^2$	$(1.364 \pm 0.001) \times 10^3$	$(1.73 \pm 0.01) \times 10^4$	$(1.14 \pm 0.01) \times 10^4$	$(1.26 \pm 0.01) \times 10^4$	$(1.47 \pm 0.02) \times 10^4$	
S16	$(1.36 \pm 0.02) \times 10^1$	$(1.83 \pm 0.02) \times 10^1$	$(4.0 \pm 0.2) \times 10^2$	$(3.3 \pm 0.2) \times 10^2$	$(4.4 \pm 0.1) \times 10^2$	$(5.7 \pm 0.2) \times 10^2$	sc
S15	$(4.72 \pm 0.02) \times 10^1$	$(5.73 \pm 0.02) \times 10^1$	$(1.412 \pm 0.008) \times 10^3$	$(1.81 \pm 0.01) \times 10^3$	$(2.55 \pm 0.04) \times 10^3$	$(2.80 \pm 0.05) \times 10^3$	
S14	$(1.645 \pm 0.007) \times 10^2$	$(1.247 \pm 0.008) \times 10^2$	$(2.14 \pm 0.02) \times 10^3$	$(4.44 \pm 0.04) \times 10^3$	$(6.35 \pm 0.09) \times 10^3$	$(4.5 \pm 0.1) \times 10^3$	
S11	$(1.76 \pm 0.01) \times 10^2$	$(4.52 \pm 0.04) \times 10^2$	$(1.20 \pm 0.03) \times 10^4$	$(1.00 \pm 0.02) \times 10^4$	$(1.55 \pm 0.03) \times 10^4$	$(1.55 \pm 0.03) \times 10^4$	
S8	$(4.82 \pm 0.05) \times 10^1$	$(5.74 \pm 0.06) \times 10^1$	$(1.70 \pm 0.05) \times 10^3$	$(1.89 \pm 0.05) \times 10^3$	$(2.28 \pm 0.07) \times 10^3$	$(2.42 \pm 0.09) \times 10^3$	
S7	$(5.406 \pm 0.005) \times 10^2$	$(7.872 \pm 0.006) \times 10^2$	$(1.205 \pm 0.001) \times 10^4$	$(1.614 \pm 0.001) \times 10^4$	$(2.208 \pm 0.003) \times 10^4$	$(2.383 \pm 0.005) \times 10^4$	sc
S1	$(3.84 \pm 0.03) \times 10^2$	$(1.385 \pm 0.002) \times 10^3$	$(1.926 \pm 0.004) \times 10^4$	$(1.676 \pm 0.007) \times 10^4$	$(1.39 \pm 0.02) \times 10^4$	$(1.47 \pm 0.02) \times 10^4$	
CS100	$(1.37 \pm 0.03) \times 10^1$	$(2.52 \pm 0.03) \times 10^1$	$(2.9 \pm 0.2) \times 10^2$	$(1.8 \pm 0.1) \times 10^2$	$(1.4 \pm 0.2) \times 10^2$	$(2.2 \pm 0.3) \times 10^2$	
CS98	$(1.22 \pm 0.02) \times 10^1$	$(6.2 \pm 0.2) \times 10^0$	$(1.3 \pm 0.2) \times 10^2$	$(1.1 \pm 0.1) \times 10^2$	$(1.1 \pm 0.2) \times 10^2$	$(8.2 \pm 2.1) \times 10^1$	
CS93	$(8.1 \pm 0.8) \times 10^{-1}$	$(1.5 \pm 0.1) \times 10^0$	$(5.8 \pm 0.2) \times 10^1$	$(5.1 \pm 0.2) \times 10^1$	$(1.12 \pm 0.05) \times 10^2$	$(2.67 \pm 0.09) \times 10^2$	sc
CS84	$(6.71 \pm 0.04) \times 10^1$	$(1.728 \pm 0.003) \times 10^2$	$(3.74 \pm 0.07) \times 10^3$	$(1.80 \pm 0.05) \times 10^3$	$(1.77 \pm 0.06) \times 10^3$	$(1.03 \pm 0.05) \times 10^3$	
CS82	$(4.5 \pm 0.2) \times 10^1$	$(3.7 \pm 0.1) \times 10^2$	$(3.1 \pm 0.4) \times 10^3$	$(1.3 \pm 0.2) \times 10^3$	$(1.3 \pm 0.2) \times 10^3$	$(1.2 \pm 0.2) \times 10^3$	
CS81	$(1.02 \pm 0.01) \times 10^2$	$(8.13 \pm 0.03) \times 10^2$	$(6.6 \pm 0.3) \times 10^3$	$(4.3 \pm 0.2) \times 10^3$	$(2.9 \pm 0.2) \times 10^3$	$(2.8 \pm 0.2) \times 10^3$	
CS80	$(8.89 \pm 0.06) \times 10^0$	$(2.16 \pm 0.01) \times 10^1$	$(3.8 \pm 0.1) \times 10^2$	$(3.8 \pm 0.2) \times 10^2$	$(2.6 \pm 0.1) \times 10^2$	$(2.5 \pm 0.1) \times 10^2$	sc
CS79	$(2.860 \pm 0.006) \times 10^2$	$(3.822 \pm 0.006) \times 10^2$	$(9.57 \pm 0.02) \times 10^3$	$(9.14 \pm 0.02) \times 10^3$	$(8.61 \pm 0.04) \times 10^3$	$(6.93 \pm 0.05) \times 10^3$	sc
CS72	$(4.43 \pm 0.07) \times 10^0$	$(3.08 \pm 0.07) \times 10^0$	$(1.43 \pm 0.09) \times 10^2$	$(1.39 \pm 0.09) \times 10^2$	$(1.4 \pm 0.2) \times 10^2$	$(1.2 \pm 0.2) \times 10^2$	
CS71	$(6.03 \pm 0.04) \times 10^1$	$(7.83 \pm 0.05) \times 10^1$	$(2.56 \pm 0.04) \times 10^3$	$(1.67 \pm 0.03) \times 10^3$	$(1.62 \pm 0.05) \times 10^3$	$(1.64 \pm 0.05) \times 10^3$	
CS62	$(1.45 \pm 0.03) \times 10^2$	$(1.740 \pm 0.003) \times 10^3$	$(9.5 \pm 0.2) \times 10^3$	$(7.2 \pm 0.2) \times 10^3$	$(2.8 \pm 0.3) \times 10^3$	$(3.3 \pm 0.3) \times 10^3$	
CS60	$(4.16 \pm 0.04) \times 10^1$	$(4.28 \pm 0.03) \times 10^1$	$(9.4 \pm 0.2) \times 10^2$	$(9.4 \pm 0.2) \times 10^2$	$(9.1 \pm 0.2) \times 10^2$	$(1.13 \pm 0.03) \times 10^3$	
CS57	$(1.260 \pm 0.006) \times 10^2$	$(2.122 \pm 0.006) \times 10^2$	$(5.07 \pm 0.06) \times 10^3$	$(4.96 \pm 0.08) \times 10^3$	$(4.2 \pm 0.1) \times 10^3$	$(4.8 \pm 0.1) \times 10^3$	
CS55	$(1.131 \pm 0.002) \times 10^2$	$(5.084 \pm 0.002) \times 10^2$	$(8.62 \pm 0.05) \times 10^3$	$(4.24 \pm 0.05) \times 10^3$	$(5.14 \pm 0.05) \times 10^3$	$(8.76 \pm 0.06) \times 10^3$	sc
CS51	$(1.311 \pm 0.003) \times 10^2$	$(3.363 \pm 0.003) \times 10^2$	$(6.72 \pm 0.02) \times 10^3$	$(6.19 \pm 0.03) \times 10^3$	$(5.78 \pm 0.04) \times 10^3$	$(5.59 \pm 0.06) \times 10^3$	
CS45	$(7.95 \pm 0.05) \times 10^0$	$(3.17 \pm 0.02) \times 10^1$	$(3.3 \pm 0.1) \times 10^2$	$(2.2 \pm 0.1) \times 10^2$	$(1.3 \pm 0.1) \times 10^2$	$(1.3 \pm 0.2) \times 10^2$	
CS40	$(5.05 \pm 0.05) \times 10^0$	$(1.632 \pm 0.005) \times 10^1$	$(1.77 \pm 0.06) \times 10^2$	$(1.6 \pm 0.1) \times 10^2$	$(8.9 \pm 0.4) \times 10^1$	$(6.5 \pm 0.5) \times 10^1$	sc
CS39	$(3.62 \pm 0.02) \times 10^1$	$(3.51 \pm 0.03) \times 10^1$	$(4.79 \pm 0.05) \times 10^2$	$(6.81 \pm 0.05) \times 10^2$	$(1.34 \pm 0.01) \times 10^3$	$(1.35 \pm 0.02) \times 10^3$	
CS33	$(5.80 \pm 0.04) \times 10^1$	$(1.506 \pm 0.003) \times 10^2$	$(2.81 \pm 0.02) \times 10^3$	$(2.29 \pm 0.02) \times 10^3$	$(2.56 \pm 0.03) \times 10^3$	$(3.14 \pm 0.04) \times 10^3$	
CS2	$(1.03 \pm 0.01) \times 10^2$	$(2.96 \pm 0.02) \times 10^2$	$(3.0 \pm 0.2) \times 10^3$	$(1.3 \pm 0.2) \times 10^3$	$(3.1 \pm 0.2) \times 10^3$	$(4.4 \pm 0.3) \times 10^3$	

sc: The background region to estimate the background level is modified from that automatically selected in the aperture photometry to avoid source contaminations.

Table 3: Summary of the luminosities obtained by the SED fitting.

Name	$\log(L_{\text{TIR}}/L_{\odot})$	$\log(L_{\text{PAH}}/L_{\odot})$	$\log(L_{\text{warm}}/L_{\odot})$	$\log(L_{\text{cold}}/L_{\odot})$
CN15	4.54 ± 0.31	3.37 ± 0.36	4.43 ± 0.40	3.72 ± 0.38
CN17	4.04 ± 0.29	3.02 ± 0.36	3.92 ± 0.38	3.23 ± 0.37
CN24	6.50 ± 0.17	5.37 ± 0.15	6.39 ± 0.22	5.67 ± 0.18
CN39	4.55 ± 0.16	3.76 ± 0.15	4.44 ± 0.21	3.23 ± 0.18
CN43	5.47 ± 0.16	4.20 ± 0.16	5.32 ± 0.22	4.86 ± 0.18
CN58	5.82 ± 0.13	4.77 ± 0.12	5.61 ± 0.20	5.30 ± 0.15
CN63	5.87 ± 0.10	4.95 ± 0.07	5.64 ± 0.17	5.31 ± 0.11
CN64	5.50 ± 0.16	4.31 ± 0.14	5.36 ± 0.20	4.85 ± 0.17
CN65	5.58 ± 0.14	4.47 ± 0.06	5.51 ± 0.17	4.43 ± 0.12
CN66	5.71 ± 0.13	4.58 ± 0.06	5.60 ± 0.17	4.90 ± 0.11
CN71	5.63 ± 0.13	4.53 ± 0.07	5.52 ± 0.17	4.80 ± 0.12
CN73	4.15 ± 0.14	2.53 ± 0.08	4.09 ± 0.16	3.16 ± 0.12
CN77	6.21 ± 0.11	5.31 ± 0.06	6.07 ± 0.17	5.39 ± 0.11
CN88	5.31 ± 0.23	4.47 ± 0.26	5.19 ± 0.30	4.32 ± 0.28
CN90	5.02 ± 0.22	4.16 ± 0.26	4.87 ± 0.30	4.16 ± 0.28
CN99	6.48 ± 0.12	5.41 ± 0.06	6.35 ± 0.16	5.74 ± 0.11
CN101	4.96 ± 0.14	3.78 ± 0.06	4.89 ± 0.16	3.89 ± 0.13
CN108	6.23 ± 0.11	5.32 ± 0.12	5.92 ± 0.20	5.82 ± 0.15
CN111	5.20 ± 0.10	4.39 ± 0.07	4.93 ± 0.17	4.68 ± 0.11
CN114	5.20 ± 0.12	4.34 ± 0.09	5.05 ± 0.18	4.40 ± 0.13
CN120	4.69 ± 0.14	3.60 ± 0.08	4.60 ± 0.17	3.66 ± 0.13
CN123	4.78 ± 0.12	3.91 ± 0.09	4.61 ± 0.18	4.06 ± 0.13
CN138	4.48 ± 0.12	3.52 ± 0.13	4.24 ± 0.21	3.98 ± 0.16
CN139	5.70 ± 0.15	4.80 ± 0.15	5.53 ± 0.21	4.98 ± 0.17
CN142	4.98 ± 0.12	3.88 ± 0.05	4.85 ± 0.16	4.23 ± 0.11
N1	4.61 ± 0.15	3.44 ± 0.12	4.49 ± 0.19	3.83 ± 0.15
CN148	5.53 ± 0.16	4.25 ± 0.13	5.45 ± 0.20	4.58 ± 0.16
N4	5.15 ± 0.13	4.34 ± 0.12	4.97 ± 0.19	4.40 ± 0.15
N6	5.56 ± 0.14	4.82 ± 0.12	5.39 ± 0.19	4.72 ± 0.16
N10	5.67 ± 0.14	4.57 ± 0.12	5.50 ± 0.20	5.05 ± 0.15

Continued.

Name	$\log(L_{\text{TIR}}/L_{\odot})$	$\log(L_{\text{PAH}}/L_{\odot})$	$\log(L_{\text{warm}}/L_{\odot})$	$\log(L_{\text{cold}}/L_{\odot})$
N11	4.87 ± 0.13	3.98 ± 0.12	4.59 ± 0.20	4.42 ± 0.15
N12	5.60 ± 0.13	4.81 ± 0.12	5.41 ± 0.19	4.88 ± 0.15
N13	3.68 ± 0.15	2.53 ± 0.12	3.55 ± 0.20	2.95 ± 0.16
N14	5.21 ± 0.15	4.27 ± 0.12	5.08 ± 0.20	4.35 ± 0.16
N20	5.27 ± 0.12	4.71 ± 0.12	5.04 ± 0.19	4.39 ± 0.16
N23	5.02 ± 0.13	4.07 ± 0.10	4.91 ± 0.17	4.13 ± 0.14
N24	6.85 ± 0.13	5.92 ± 0.12	6.66 ± 0.20	6.24 ± 0.15
N25	5.12 ± 0.11	4.44 ± 0.12	4.77 ± 0.22	4.66 ± 0.15
N27	4.12 ± 0.19	3.20 ± 0.26	3.76 ± 0.30	3.77 ± 0.27
N29	4.54 ± 0.13	3.67 ± 0.12	4.37 ± 0.19	3.80 ± 0.15
N30	4.25 ± 0.23	3.47 ± 0.27	4.10 ± 0.31	3.35 ± 0.29
N32	5.17 ± 0.15	4.28 ± 0.12	5.05 ± 0.19	4.22 ± 0.16
N33	4.91 ± 0.15	3.93 ± 0.12	4.79 ± 0.20	4.08 ± 0.16
N34	5.56 ± 0.15	4.74 ± 0.12	5.45 ± 0.19	4.48 ± 0.18
N35	6.64 ± 0.15	5.48 ± 0.12	6.54 ± 0.19	5.74 ± 0.16
N36	6.30 ± 0.14	4.92 ± 0.12	6.12 ± 0.20	5.76 ± 0.15
N39	6.59 ± 0.16	5.43 ± 0.12	6.51 ± 0.19	5.54 ± 0.16
N40	5.61 ± 0.16	4.44 ± 0.12	5.52 ± 0.19	4.68 ± 0.16
N42	4.59 ± 0.13	3.62 ± 0.12	4.40 ± 0.20	4.00 ± 0.15
N43	4.97 ± 0.14	3.96 ± 0.12	4.77 ± 0.20	4.40 ± 0.15
N44	4.30 ± 0.11	3.52 ± 0.12	3.97 ± 0.21	3.88 ± 0.15
N45	5.71 ± 0.14	4.81 ± 0.12	5.57 ± 0.19	4.87 ± 0.15
N47	5.73 ± 0.12	4.40 ± 0.12	5.42 ± 0.22	5.40 ± 0.15
N48	4.87 ± 0.12	3.93 ± 0.12	4.57 ± 0.20	4.45 ± 0.15
N49	5.36 ± 0.14	4.31 ± 0.12	5.19 ± 0.20	4.75 ± 0.15
N50	5.41 ± 0.16	4.24 ± 0.12	5.33 ± 0.19	4.42 ± 0.17
N52	6.87 ± 0.16	5.52 ± 0.12	6.79 ± 0.19	6.00 ± 0.16
N53	5.28 ± 0.13	4.34 ± 0.12	5.10 ± 0.20	4.63 ± 0.15
N56	4.89 ± 0.10	4.22 ± 0.12	4.44 ± 0.22	4.52 ± 0.15
N57	2.57 ± 0.11	1.69 ± 0.12	2.30 ± 0.21	2.09 ± 0.15
N58	4.37 ± 0.16	3.63 ± 0.12	4.26 ± 0.19	3.05 ± 0.16

Continued.

Name	$\log(L_{\text{TIR}}/L_{\odot})$	$\log(L_{\text{PAH}}/L_{\odot})$	$\log(L_{\text{warm}}/L_{\odot})$	$\log(L_{\text{cold}}/L_{\odot})$
N59	6.20 ± 0.11	5.35 ± 0.12	5.90 ± 0.20	5.75 ± 0.15
N62	4.69 ± 0.13	3.71 ± 0.12	4.56 ± 0.20	3.89 ± 0.15
N64	5.04 ± 0.12	4.00 ± 0.12	4.75 ± 0.20	4.63 ± 0.15
N65	4.95 ± 0.13	3.87 ± 0.12	4.73 ± 0.20	4.44 ± 0.15
N66	4.28 ± 0.12	3.50 ± 0.12	4.00 ± 0.20	3.78 ± 0.16
N69	5.62 ± 0.11	4.76 ± 0.12	5.18 ± 0.22	5.32 ± 0.15
N70	5.08 ± 0.15	3.80 ± 0.12	4.98 ± 0.19	4.27 ± 0.16
N71	5.65 ± 0.11	4.68 ± 0.12	5.31 ± 0.21	5.29 ± 0.15
N73	5.01 ± 0.12	4.11 ± 0.12	4.77 ± 0.20	4.50 ± 0.15
N75	4.07 ± 0.13	3.32 ± 0.12	3.89 ± 0.20	3.27 ± 0.16
N77	4.22 ± 0.11	3.62 ± 0.12	3.94 ± 0.20	3.58 ± 0.15
N78	2.25 ± 0.12	1.67 ± 0.12	2.01 ± 0.20	1.45 ± 0.16
N79	4.29 ± 0.14	3.28 ± 0.12	4.14 ± 0.19	3.61 ± 0.15
N80	3.14 ± 0.14	1.95 ± 0.12	3.00 ± 0.20	2.49 ± 0.16
N81	6.53 ± 0.11	5.56 ± 0.12	6.03 ± 0.22	6.29 ± 0.15
N82	5.50 ± 0.14	4.63 ± 0.12	5.35 ± 0.19	4.67 ± 0.15
N83	4.82 ± 0.15	3.93 ± 0.12	4.73 ± 0.19	3.60 ± 0.16
N84	3.45 ± 0.12	2.72 ± 0.12	3.21 ± 0.19	2.84 ± 0.15
N89	4.23 ± 0.12	3.48 ± 0.12	3.90 ± 0.20	3.79 ± 0.15
N90	3.93 ± 0.13	3.15 ± 0.12	3.72 ± 0.20	3.24 ± 0.15
N91	5.85 ± 0.12	5.11 ± 0.12	5.61 ± 0.20	5.23 ± 0.15
N92	4.52 ± 0.11	3.91 ± 0.12	4.22 ± 0.20	3.93 ± 0.15
N95	4.58 ± 0.13	3.77 ± 0.12	4.39 ± 0.20	3.89 ± 0.15
N96	4.58 ± 0.14	3.73 ± 0.12	4.42 ± 0.19	3.76 ± 0.15
N98	4.60 ± 0.12	3.85 ± 0.12	4.34 ± 0.20	4.04 ± 0.15
N101	5.96 ± 0.17	4.74 ± 0.12	5.90 ± 0.19	4.75 ± 0.16
N104	4.22 ± 0.18	3.59 ± 0.26	3.91 ± 0.31	3.67 ± 0.28
N105	5.15 ± 0.11	4.44 ± 0.10	4.88 ± 0.19	4.58 ± 0.13
N106	3.81 ± 0.16	3.20 ± 0.20	3.59 ± 0.26	2.99 ± 0.23
N107	6.11 ± 0.13	5.29 ± 0.15	5.83 ± 0.22	5.62 ± 0.18
N109	6.75 ± 0.09	6.00 ± 0.08	6.41 ± 0.18	6.30 ± 0.12

Continued.

Name	$\log(L_{\text{TIR}}/L_{\odot})$	$\log(L_{\text{PAH}}/L_{\odot})$	$\log(L_{\text{warm}}/L_{\odot})$	$\log(L_{\text{cold}}/L_{\odot})$
N111	5.48 ± 0.12	4.60 ± 0.07	5.33 ± 0.16	4.69 ± 0.11
N113	5.31 ± 0.13	4.38 ± 0.09	5.19 ± 0.17	4.41 ± 0.13
N114	5.58 ± 0.11	4.73 ± 0.07	5.40 ± 0.17	4.89 ± 0.11
N115	5.29 ± 0.12	4.61 ± 0.12	5.08 ± 0.19	4.50 ± 0.15
N116	5.35 ± 0.13	4.36 ± 0.09	5.23 ± 0.17	4.49 ± 0.13
N117	5.48 ± 0.13	4.58 ± 0.12	5.32 ± 0.19	4.76 ± 0.15
N120	2.98 ± 0.20	2.25 ± 0.28	2.74 ± 0.32	2.35 ± 0.29
N122	4.13 ± 0.12	3.49 ± 0.10	3.96 ± 0.18	3.10 ± 0.14
N123	4.39 ± 0.15	3.49 ± 0.12	4.27 ± 0.19	3.42 ± 0.15
N124	3.77 ± 0.10	3.22 ± 0.12	3.36 ± 0.21	3.28 ± 0.15
N126	4.31 ± 0.11	3.83 ± 0.12	4.04 ± 0.20	3.42 ± 0.15
N127	2.99 ± 0.10	2.39 ± 0.12	2.56 ± 0.21	2.57 ± 0.15
N130	3.23 ± 0.10	2.70 ± 0.12	2.75 ± 0.22	2.81 ± 0.15
N131	5.19 ± 0.12	4.26 ± 0.11	4.96 ± 0.19	4.67 ± 0.14
N133	4.81 ± 0.15	3.87 ± 0.12	4.70 ± 0.19	3.81 ± 0.16
N134	5.00 ± 0.24	4.13 ± 0.26	4.91 ± 0.30	3.79 ± 0.28
S186	5.79 ± 0.15	4.63 ± 0.12	5.68 ± 0.19	4.96 ± 0.15
S181	6.23 ± 0.17	5.08 ± 0.12	6.18 ± 0.19	4.84 ± 0.16
S163	5.62 ± 0.10	4.74 ± 0.06	5.32 ± 0.17	5.17 ± 0.11
S155	5.67 ± 0.16	4.64 ± 0.11	5.58 ± 0.19	4.66 ± 0.15
S150	5.17 ± 0.21	4.17 ± 0.24	5.04 ± 0.28	4.37 ± 0.26
S149	5.23 ± 0.17	4.26 ± 0.13	5.15 ± 0.20	3.92 ± 0.17
S145	6.40 ± 0.16	5.43 ± 0.15	6.24 ± 0.21	5.68 ± 0.18
S144	5.18 ± 0.21	4.21 ± 0.22	5.07 ± 0.27	4.22 ± 0.24
S143	6.14 ± 0.16	5.38 ± 0.19	5.95 ± 0.24	5.41 ± 0.21
S141	5.10 ± 0.24	4.16 ± 0.29	4.97 ± 0.33	4.26 ± 0.31
S138	5.39 ± 0.13	4.24 ± 0.06	5.33 ± 0.16	4.22 ± 0.14
S137	5.44 ± 0.14	4.82 ± 0.19	5.16 ± 0.25	4.81 ± 0.21
S136	4.45 ± 0.12	3.86 ± 0.15	4.11 ± 0.23	3.91 ± 0.17
S135	4.15 ± 0.25	3.12 ± 0.25	4.08 ± 0.29	2.91 ± 0.27
S134	5.03 ± 0.13	4.04 ± 0.06	4.94 ± 0.16	4.01 ± 0.13

Continued.

Name	$\log(L_{\text{TIR}}/L_{\odot})$	$\log(L_{\text{PAH}}/L_{\odot})$	$\log(L_{\text{warm}}/L_{\odot})$	$\log(L_{\text{cold}}/L_{\odot})$
S133	5.74 ± 0.12	4.72 ± 0.06	5.63 ± 0.16	4.86 ± 0.12
S132	3.26 ± 0.20	2.53 ± 0.25	3.06 ± 0.32	2.55 ± 0.27
S123	4.78 ± 0.21	4.07 ± 0.31	4.46 ± 0.35	4.30 ± 0.33
S116	6.06 ± 0.15	5.09 ± 0.14	5.89 ± 0.21	5.40 ± 0.17
S115	4.60 ± 0.09	3.77 ± 0.06	4.25 ± 0.18	4.22 ± 0.11
S104	4.67 ± 0.22	3.65 ± 0.23	4.59 ± 0.27	3.56 ± 0.25
S96	5.31 ± 0.22	4.35 ± 0.24	5.19 ± 0.28	4.39 ± 0.26
S92	6.48 ± 0.11	5.53 ± 0.06	6.27 ± 0.17	5.93 ± 0.11
S91	4.59 ± 0.11	3.82 ± 0.13	4.15 ± 0.22	4.25 ± 0.15
S84	5.06 ± 0.13	4.17 ± 0.06	4.97 ± 0.16	3.79 ± 0.13
S76	6.01 ± 0.17	4.69 ± 0.16	5.92 ± 0.21	5.16 ± 0.18
S74	4.44 ± 0.18	3.36 ± 0.16	4.35 ± 0.22	3.47 ± 0.19
S73	5.20 ± 0.14	4.43 ± 0.16	4.98 ± 0.22	4.58 ± 0.18
S71	5.76 ± 0.12	4.79 ± 0.07	5.67 ± 0.15	4.73 ± 0.11
S70	5.70 ± 0.11	4.76 ± 0.05	5.54 ± 0.16	4.98 ± 0.11
S67	5.22 ± 0.14	4.17 ± 0.10	5.10 ± 0.18	4.39 ± 0.14
S66	6.48 ± 0.12	5.43 ± 0.09	6.29 ± 0.18	5.91 ± 0.13
S64	6.11 ± 0.16	4.64 ± 0.12	6.02 ± 0.19	5.31 ± 0.16
S62	5.74 ± 0.14	4.66 ± 0.11	5.64 ± 0.18	4.86 ± 0.14
S54	5.88 ± 0.10	5.13 ± 0.05	5.64 ± 0.16	5.28 ± 0.10
S51	5.99 ± 0.16	4.81 ± 0.12	5.89 ± 0.19	5.10 ± 0.16
S44	5.27 ± 0.12	4.42 ± 0.10	5.09 ± 0.18	4.59 ± 0.14
S41	6.32 ± 0.15	5.10 ± 0.12	6.22 ± 0.19	5.47 ± 0.15
S37	5.10 ± 0.14	4.22 ± 0.12	4.95 ± 0.19	4.27 ± 0.15
S36	6.36 ± 0.15	5.07 ± 0.12	6.27 ± 0.19	5.51 ± 0.15
S34	5.32 ± 0.10	4.08 ± 0.04	5.20 ± 0.13	4.61 ± 0.09
S29	5.81 ± 0.16	4.79 ± 0.16	5.66 ± 0.22	5.10 ± 0.19
S24	4.53 ± 0.20	3.60 ± 0.19	4.43 ± 0.25	3.53 ± 0.23
S23	5.19 ± 0.13	4.12 ± 0.12	5.02 ± 0.20	4.56 ± 0.15
S20	3.84 ± 0.15	2.71 ± 0.12	3.75 ± 0.19	2.95 ± 0.15
S18	5.27 ± 0.11	4.13 ± 0.06	5.13 ± 0.14	4.59 ± 0.11

Continued.

Name	$\log(L_{\text{TIR}}/L_{\odot})$	$\log(L_{\text{PAH}}/L_{\odot})$	$\log(L_{\text{warm}}/L_{\odot})$	$\log(L_{\text{cold}}/L_{\odot})$
S17	5.73 ± 0.15	4.71 ± 0.12	5.63 ± 0.19	4.81 ± 0.15
S16	5.32 ± 0.11	4.52 ± 0.05	5.12 ± 0.17	4.61 ± 0.11
S15	4.75 ± 0.16	3.81 ± 0.20	4.52 ± 0.25	4.22 ± 0.22
S14	4.99 ± 0.11	4.30 ± 0.12	4.68 ± 0.20	4.47 ± 0.15
S11	5.21 ± 0.14	4.00 ± 0.12	5.05 ± 0.20	4.57 ± 0.15
S8	5.40 ± 0.09	4.44 ± 0.05	5.22 ± 0.14	4.76 ± 0.10
S7	4.98 ± 0.12	4.05 ± 0.12	4.76 ± 0.20	4.43 ± 0.15
S1	5.98 ± 0.22	4.85 ± 0.22	5.90 ± 0.27	5.02 ± 0.24
CS100	3.52 ± 0.17	2.76 ± 0.16	3.40 ± 0.22	2.41 ± 0.20
CS98	3.20 ± 0.14	2.71 ± 0.16	2.98 ± 0.23	2.15 ± 0.21
CS84	6.27 ± 0.13	5.23 ± 0.06	6.20 ± 0.16	4.96 ± 0.13
CS82	6.16 ± 0.15	4.94 ± 0.05	6.10 ± 0.17	4.94 ± 0.13
CS81	6.57 ± 0.14	5.30 ± 0.05	6.52 ± 0.15	5.27 ± 0.12
CS80	5.30 ± 0.13	4.28 ± 0.05	5.21 ± 0.15	4.25 ± 0.11
CS79	5.01 ± 0.16	4.10 ± 0.16	4.88 ± 0.22	4.13 ± 0.19
CS72	4.06 ± 0.14	3.20 ± 0.12	3.90 ± 0.20	3.27 ± 0.16
CS71	5.27 ± 0.15	4.34 ± 0.12	5.16 ± 0.19	4.33 ± 0.16
CS62	5.25 ± 0.22	3.99 ± 0.19	5.19 ± 0.24	4.03 ± 0.23
CS60	4.41 ± 0.26	3.62 ± 0.35	4.24 ± 0.38	3.62 ± 0.36
CS57	5.84 ± 0.14	4.84 ± 0.12	5.72 ± 0.19	4.99 ± 0.15
CS51	5.83 ± 0.15	4.72 ± 0.12	5.73 ± 0.19	4.96 ± 0.16
CS45	4.75 ± 0.13	3.99 ± 0.05	4.66 ± 0.15	3.15 ± 0.13
CS40	4.57 ± 0.16	3.60 ± 0.12	4.51 ± 0.19	2.93 ± 0.17
CS39	5.75 ± 0.14	5.02 ± 0.19	5.33 ± 0.25	5.38 ± 0.21
CS33	5.96 ± 0.12	4.87 ± 0.04	5.83 ± 0.16	5.17 ± 0.10

3 Results

3.1 Total luminosities of Galactic IR bubbles

Figure 5 shows the relation between L_{TIR} and the bubble radius, R (pc), calculated from R (arcmin) and the distance for all the 180 bubbles (i.e., 74 closed, 49 broken and 57 unclassified). The errors of L_{TIR} were estimated from those of the SED fitting and the distance uncertainties, while those of R were estimated from the systematic uncertainty of 11% in the circular fitting and the distance uncertainties. The L_{TIR} values of the bubbles range widely from 1×10^2 to $1 \times 10^7 L_{\odot}$, which correspond to the bolometric luminosity, L_{bol} , of a single B-type star to many O-type stars; for example, L_{bol} of a O9–O3 star ranges from 5×10^4 to $6 \times 10^5 L_{\odot}$ (Martins et al. 2005). The figure shows that L_{TIR} and R are tightly correlated with each other, where the correlation coefficient r_c is 0.78. L_{TIR} of all the bubbles follow a power-law relation with an index of ~ 3 .

Several previous works suggested that a shell structure of a bubble is created by expansion of HII regions (e.g., Hosokawa & Inutsuka 2005; 2006; Deharveng et al. 2010). The ionization front of an HII region, which delineates the inner edge of a shell, is described as a function of the total number of ionizing photons, Q , like,

$$Q = \frac{4}{3}\pi R_s^3 n_e n_p \alpha_B(T_e), \quad (2)$$

where R_s , n_e , n_p , T_e and α_B are the Strömgen radius, electron density, proton density, electron temperature and “case-B” recombination coefficient (Strömgen 1939; Osterbrock 1989). We calculated the relation between L_{bol} and R_s for O-type stars from Q and L_{bol} given in Martins et al. (2005), assuming $n_e = n_p = 100 \text{ cm}^{-3}$ and $T_e = 10^4 \text{ K}$ as typical values for HII regions. In figure 5, we plot the $L_{\text{bol}}-R_s$ relation thus calculated on the assumption that $R \sim R_s$ and $L_{\text{TIR}} \sim L_{\text{bol}}$. As can be seen in the figure, the $L_{\text{TIR}}-R$ relation observed for the sample bubbles, as a whole, is consistent with the calculated relation.

In figure 5, there is an overall similarity in the distributions in the $L_{\text{TIR}}-R$ plots between the closed and the broken bubbles, despite their large differences in the morphology. The L_{TIR} distribution of the broken bubbles seems to extend towards higher luminosities, as compared with that of the closed bubbles. This tendency is confirmed in the histograms of L_{TIR} in figure 6; in the highest luminosity bin, the fractional number of the broken bubbles is significantly larger than that of the closed bubbles. In figure 7, we show the deviations of the data points with respect to the power-law relation along R . Here R_{all} is the radius of the bubbles as a function of L_{TIR} , determined by fitting to the data points of all the bubbles with $L_{\text{TIR}} = aR^3$ (figure 5). In the figure, the broken bubbles are systematically shifted toward larger R/R_{all} , relative to the closed bubbles, especially those with high L_{TIR} ($> 10^5 L_{\odot}$). A Kolmogorov-Smirnov (K-S) test shows that the distributions of the two types are

statistically different with a 85% confidence level (K-S value $D\sqrt{nm/(n+m)}$ of 1.15, where D is a K-S statistic, and m and n are the numbers of the closed and the broken samples, respectively).

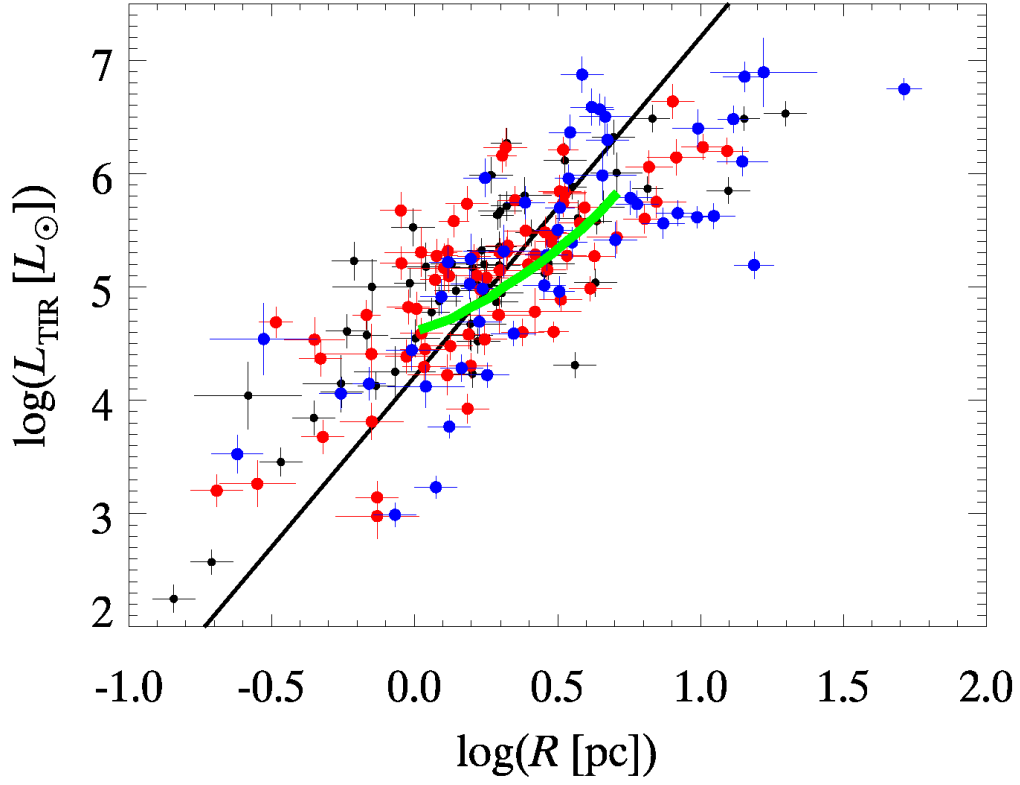


Fig. 5. Total IR luminosity (L_{TIR}) versus radius (R) for all the sample on a logarithmic scale. The red, the blue and the black circles represent the closed, the broken and the unclassified bubbles, respectively. The black line indicates the result of fitting to the data points of all the bubbles with $L_{\text{TIR}} = aR^3$. The green curve indicates the relation calculated for O-type stars (Martins et al. 2005) in HII regions with the density of 100 cm^{-3} and temperature of 10^4 K .

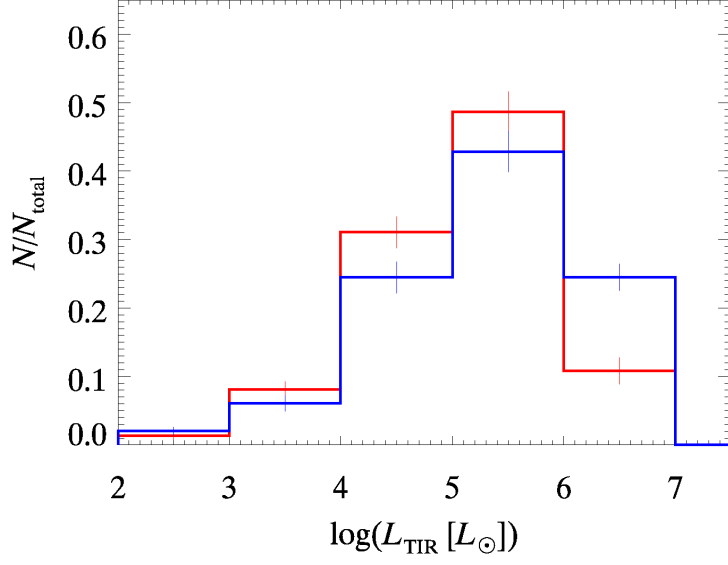


Fig. 6. Histograms of L_{TIR} . The histograms in the red and the blue line correspond to the closed bubbles and the broken bubbles, respectively. The vertical axis corresponds to the fraction of the number of the bubbles to the total for each type. Poisson errors are attached as bars.

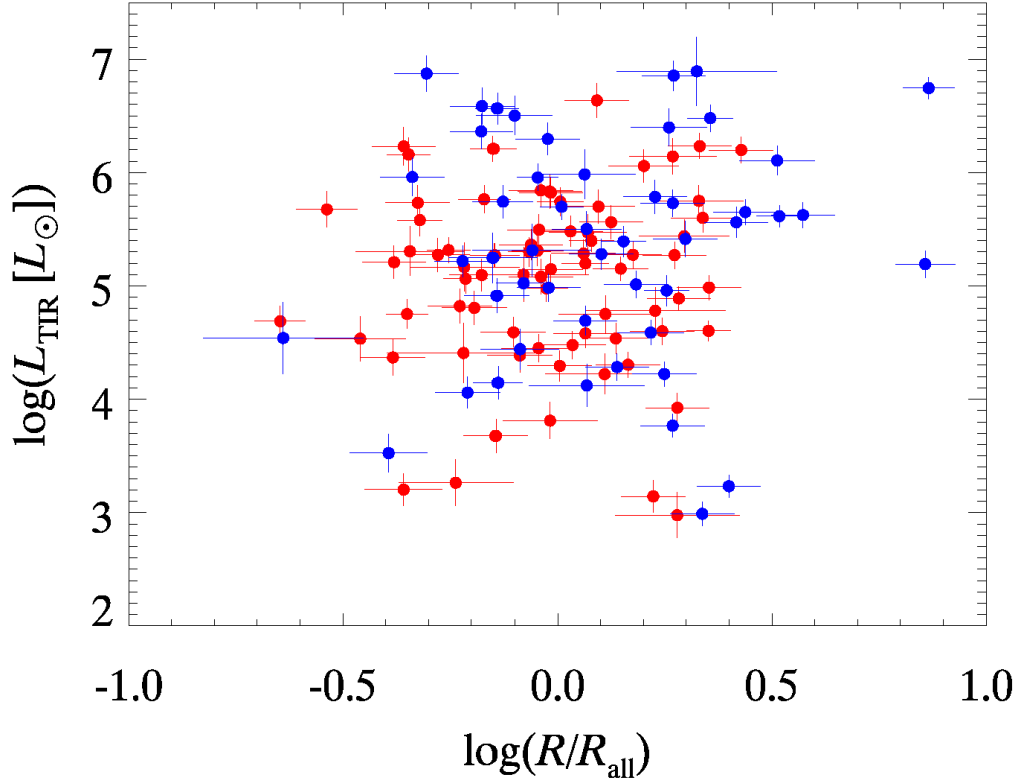


Fig. 7. L_{TIR} plotted against R/R_{all} for the closed and broken bubbles on a logarithmic scale, where R_{all} is the radius of the bubbles as a function of L_{TIR} , determined by fitting to the data points of all the bubbles with $L_{\text{TIR}} = aR^3$ (figure 5). The symbols are the same as those in figure 5.

3.2 Ratios of PAH to total luminosities of Galactic IR bubbles

Figure 8a shows the relation between the ratios of the PAH to total IR luminosities ($L_{\text{PAH}}/L_{\text{TIR}}$) and R for all the bubbles. $L_{\text{PAH}}/L_{\text{TIR}}$ and R are not significantly correlated with each other ($r_c = -0.11$). The result of the constant line fitting shows that $L_{\text{PAH}}/L_{\text{TIR}}$ is statistically constant with R for the closed bubbles ($\chi^2/\nu = 1.19$), while it is not for the broken bubbles ($\chi^2/\nu = 1.81$). A K-S test shows that the distributions of the two types are statistically different with a 90% confidence level (K-S value of 1.56). In particular, the figure reveals that the broken bubbles at radii larger than ~ 2.5 pc ($\log R \sim 0.4$) have systematically lower $L_{\text{PAH}}/L_{\text{TIR}}$ ratios.

Figure 8b shows the plot of $L_{\text{PAH}}/L_{\text{TIR}}$ against L_{TIR} for all the bubbles. In contrast to the plot of $L_{\text{PAH}}/L_{\text{TIR}}$ versus R in figure 8a, $L_{\text{PAH}}/L_{\text{TIR}}$ is significantly correlated with L_{TIR} ($r_c = -0.45$). The negative correlation of $L_{\text{PAH}}/L_{\text{TIR}}$ with L_{TIR} can be interpreted in a straightforward manner; the intense UV radiation indicated by high L_{TIR} would accelerate photodissociation of PAHs exposed to the UV (i.e., Smith et al. 2007; Bendo et al. 2008; Tielens 2008). On the other hand, no significant correlation of $L_{\text{PAH}}/L_{\text{TIR}}$ with R may be explained by considering that R does not strongly depend on L_{TIR} ($R \propto L_{\text{TIR}}^{1/3}$) and also that R depends on the gas density for a given L_{TIR} ($R \propto n^{-2/3}$; eq. 2). As can be seen in figure 5, R scatters in a range of ~ 1.5 orders of magnitude for a given L_{TIR} . This corresponds to a variation in the gas density by one order of magnitude, which will be caused by the initial conditions of the ambient ISM and/or the later expansion of an HII region. The lower $L_{\text{PAH}}/L_{\text{TIR}}$ observed for the broken bubbles at larger radii (figure 8a), and thus at higher L_{TIR} from figure 5, seems to strengthen the negative correlation for the broken bubbles in figure 8b.

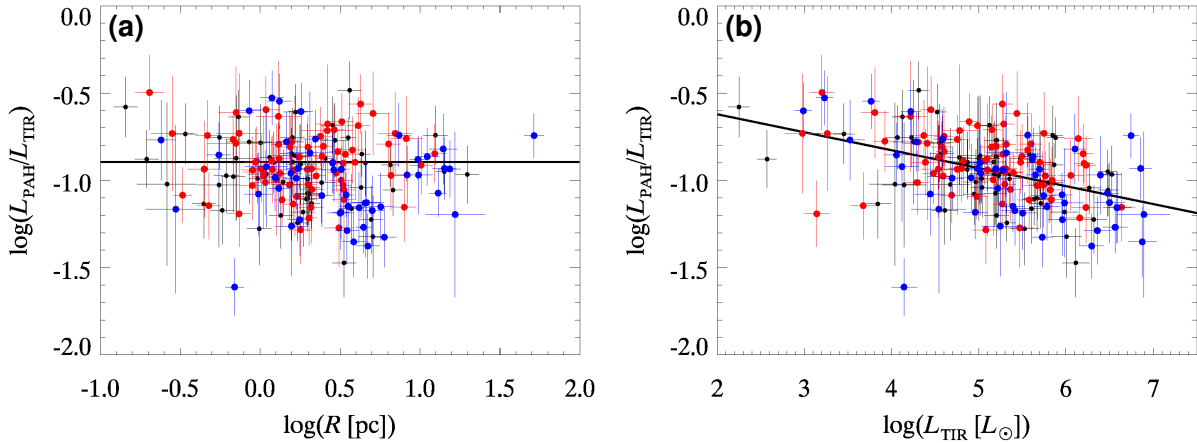


Fig. 8. Ratio of the PAH to the total IR luminosity ($L_{\text{PAH}}/L_{\text{TIR}}$) plotted against (a) R and (b) L_{TIR} for all the bubbles. The red, blue and black circles represent the closed, broken and unclassified bubbles, respectively. The line in panel (a) is the constant line fitted to the data points of the closed bubbles, while the line in panel (b) is the fitted line to the data points of all the bubbles.

Figures 9 and 10 show the $I_{\text{PAH}}/I_{\text{TIR}}$ ratio maps of 20 closed bubbles and 20 broken bubbles, respectively, which are the same sample as in figures 1 and 3. We masked the pixels where I_{TIR} has

surface brightness lower than 3 sigma of the background fluctuation above the averaged brightness at $(2-4) \times R$, in order to exclude statistically insignificant pixels. Comparing figure 10 with figure 9, we find that the whole areas of the broken bubbles tend to have lower $I_{\text{PAH}}/I_{\text{TIR}}$ ratios than the closed bubbles. The figures also show that $I_{\text{PAH}}/I_{\text{TIR}}$ ratios become lower inside the shells for both types.

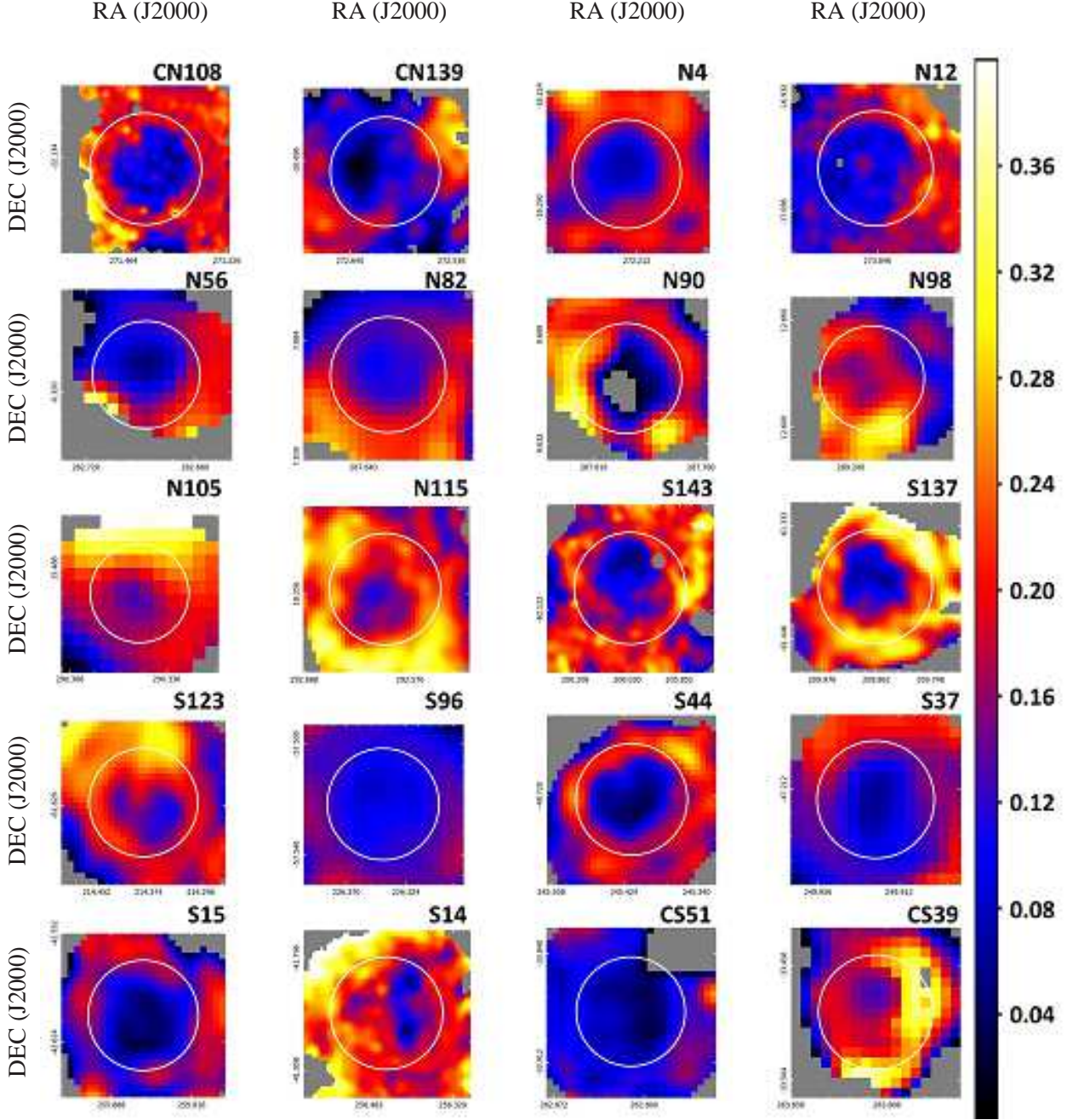


Fig. 9. $I_{\text{PAH}}/I_{\text{TIR}}$ ratio maps for the closed bubbles shown in figures 1 and 3. The white circles are the best-fit circles determined by the fitting to the Spitzer $8 \mu\text{m}$ images of the bubbles. The color levels are common among the bubbles.

In order to quantify the difference in the $I_{\text{PAH}}/I_{\text{TIR}}$ distribution between relatively large closed and broken bubbles, we calculated the radial profiles of $I_{\text{PAH}}/I_{\text{TIR}}$ in figure 11, where the $I_{\text{PAH}}/I_{\text{TIR}}$

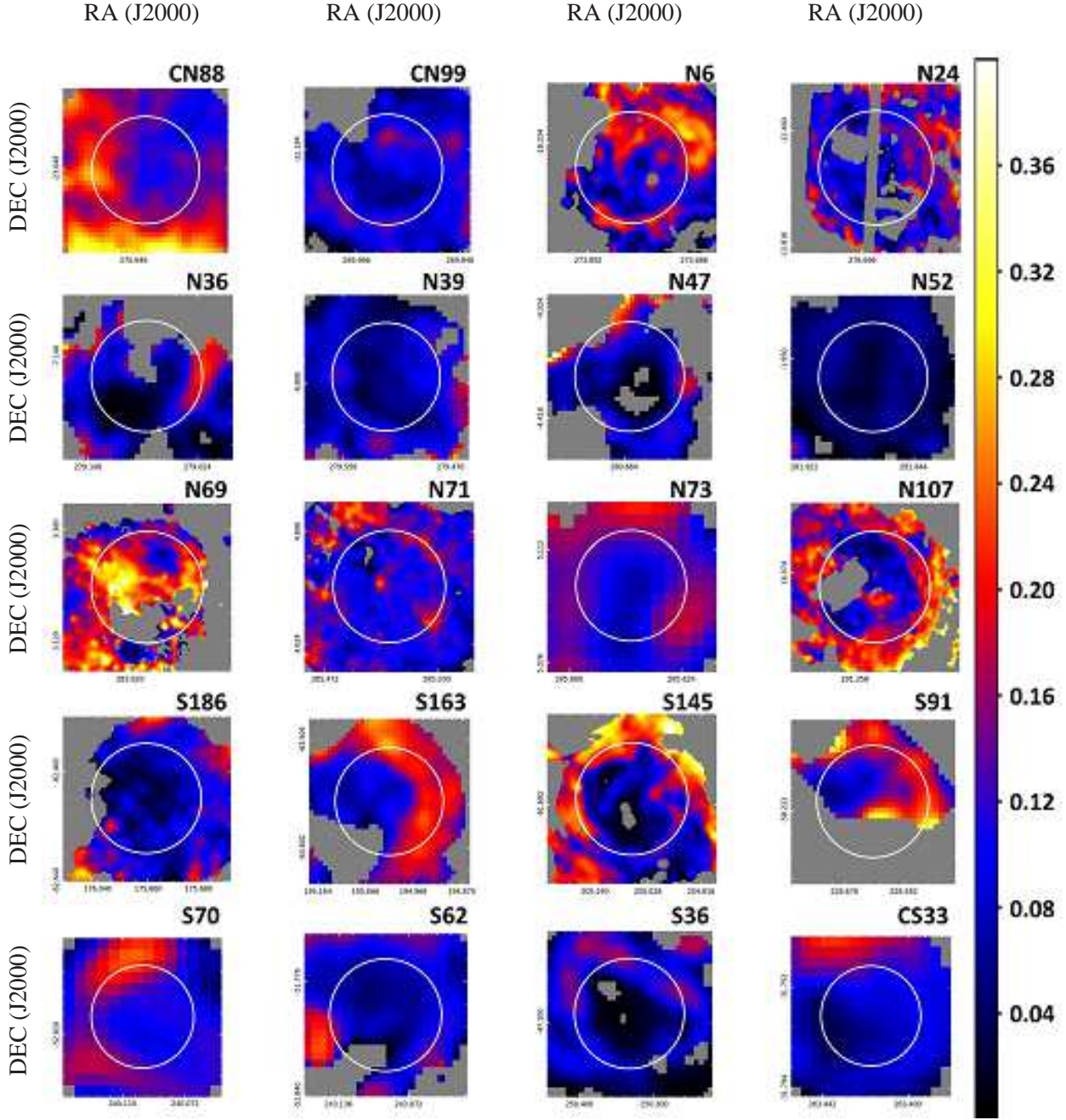


Fig. 10. Same as figure 9, but for the broken bubbles shown in figures 1 and 3.

values averaged over all the pixels within a certain radial position r are plotted against r/R . Here we selected the Galactic IR bubbles with $R > 2.5$ pc ($\log R > 0.4$). Almost every bubble in the figure shows that $I_{\text{PAH}}/I_{\text{TIR}}$ starts to increase at $r \sim R$ from the inner to outer direction, where PDRs are likely to dominate; this is reasonable since the PAH emission traces PDRs. The radial profiles of $I_{\text{PAH}}/I_{\text{TIR}}$ show a systematic difference in the absolute value between the closed and broken bubbles, although the profiles themselves are notably similar. This indicates that PAHs in the broken bubbles

are deficient in wide areas including the outside of the bubbles.

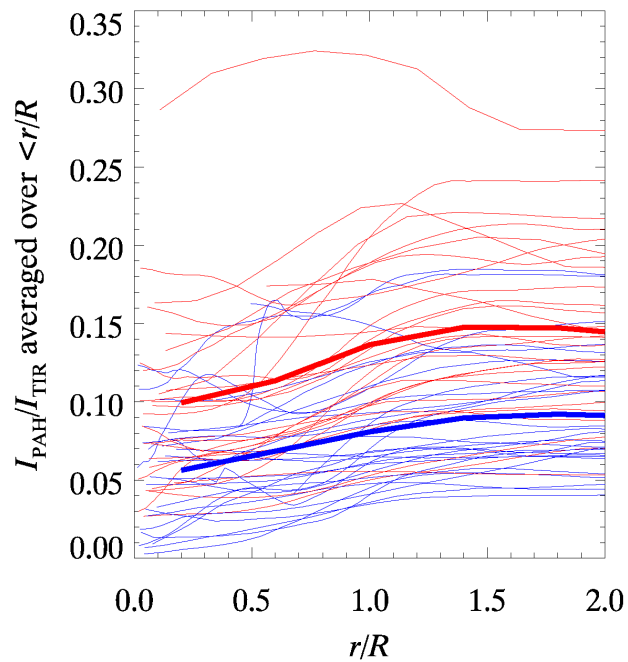


Fig. 11. Radial profiles of $I_{\text{PAH}}/I_{\text{TIR}}$ for the Galactic IR bubbles with $R > 2.5$ pc. The vertical axis shows the $I_{\text{PAH}}/I_{\text{TIR}}$ values averaged over all the pixels within r . The horizontal axis shows the radial positions normalized to R of each bubble. The red and the blue curves indicate the closed and broken bubbles, respectively, while the bold curves are their averages.

3.3 Ratios of warm dust to cold dust luminosities of Galactic IR bubbles

The left panels of figure 12 show the luminosity ratios, $L_{\text{warm}}/L_{\text{TIR}}$, $L_{\text{cold}}/L_{\text{TIR}}$ and $L_{\text{warm}}/L_{\text{cold}}$ plotted against R , while the right panels of figure 12 show those against L_{TIR} . From the top panels, we confirm that L_{warm} occupies a large fraction of L_{TIR} in most cases. In the middle and bottom panels, the luminosity ratios show some correlations with R , but not with L_{TIR} . In particular, $L_{\text{warm}}/L_{\text{cold}}$ and R are significantly correlated with each other ($r_c = -0.34$). By interpreting L_{warm} as emission of dust in HII regions, the negative correlation of $L_{\text{warm}}/L_{\text{cold}}$ with R may be reasonable; the dust more dilutes and less attenuates stellar UV photons as HII regions expand. On the other hand, no significant correlation of $L_{\text{warm}}/L_{\text{cold}}$ and L_{TIR} may be explained by considering that L_{warm} increases with L_{TIR} while L_{cold} does not necessarily because the latter depends on the conditions of the ambient ISM in parental clouds. Unlike $L_{\text{PAH}}/L_{\text{TIR}}$, there is no appreciable systematic difference between the closed and broken bubbles. Yet the brightness ratio maps of $I_{\text{warm}}/I_{\text{cold}}$ in figures 13 and 14, which are created in the same manner as the $I_{\text{PAH}}/I_{\text{TIR}}$ maps in figures 9 and 10, suggest a systematic difference between the closed and broken bubbles. The figures show that the $I_{\text{warm}}/I_{\text{cold}}$ distributions of the closed bubbles peak near the centers, while those of the broken bubbles tend to peak off the centers.

In order to quantify the difference in the $I_{\text{warm}}/I_{\text{cold}}$ distribution between the closed and broken bubbles, we calculated the second moment, I , with respect to the center for each bubble, as shown in figure 15, using the following equation:

$$I = \frac{\sum_i^n r_i^2 I_{\text{warm}}(x_i, y_i) / I_{\text{cold}}(x_i, y_i)}{R^2 \sum_i^n I_{\text{warm}}(x_i, y_i) / I_{\text{cold}}(x_i, y_i)}, \quad (3)$$

where (x_i, y_i) and r_i are the position of a pixel and the distance from the center to the pixel (i.e., $r_i = \sqrt{(x_i - l)^2 + (y_i - b)^2}$), respectively. In the calculation, we used the pixels with $r_i < R$ and higher brightness which occupy 30% of the total pixels at $r_i < R$. Since we require angular sizes large enough to spatially resolve the peak positions, we selected bubbles possessing angular radii larger than $90''$. As can be clearly seen in the figure, the broken bubbles tend to have larger I values than the closed bubbles, indicating that the positions of the heating sources associated with the broken bubbles are substantially offset from the bubble centers. Indeed a K-S test shows that the distributions of the two types are statistically different with a 85% confidence level (K-S value of 1.14). The averaged value of $I \sim 0.5$ for the broken bubbles corresponds to the peak offset of $\sim 0.7R$ from the bubble center, assuming the peak size of $1'.5$ in FWHM for a bubble of $3'$ in radius.

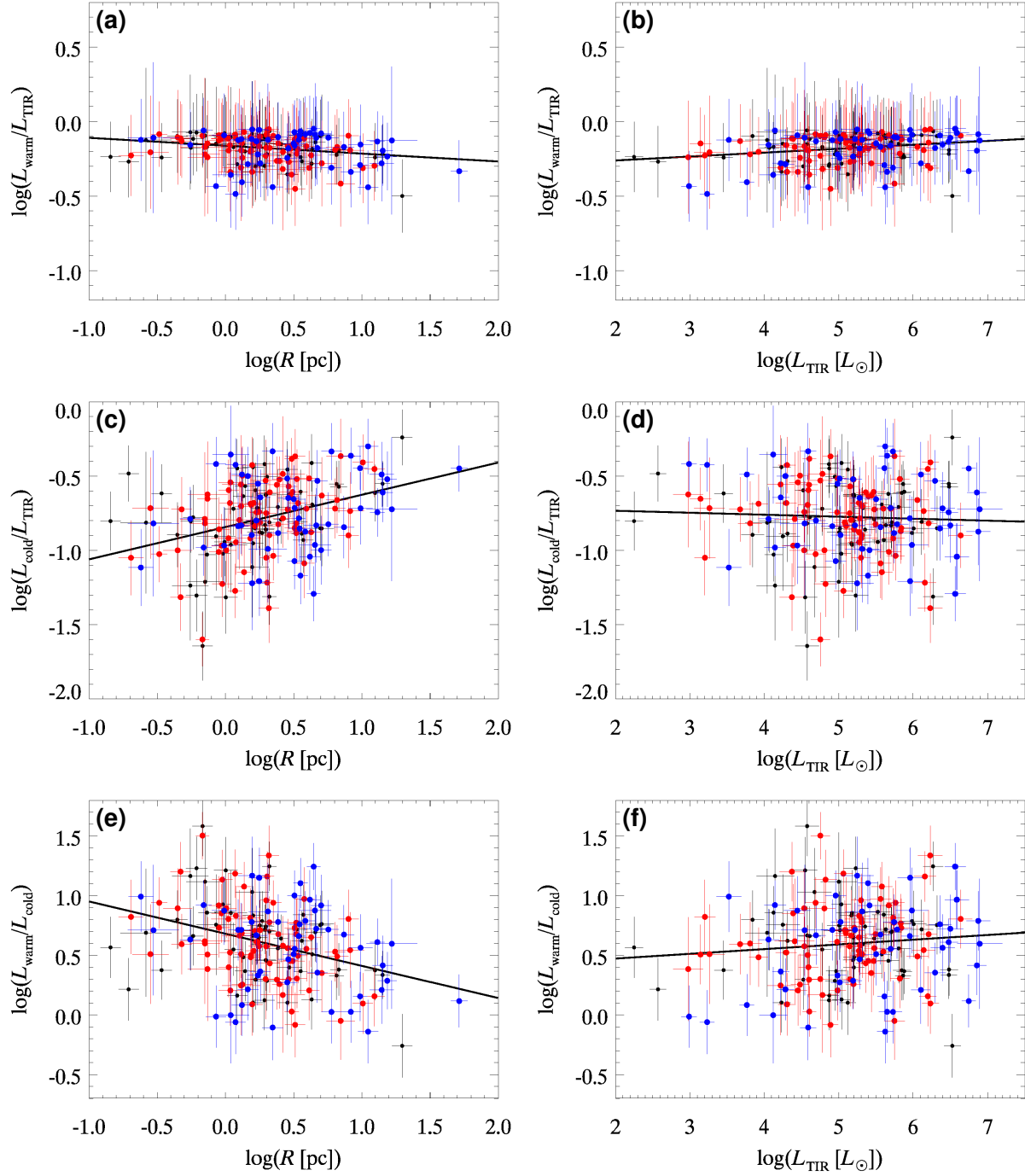


Fig. 12. Ratios of (a) the warm dust to the total IR luminosity ($L_{\text{warm}}/L_{\text{TIR}}$), (c) the cold dust to the total IR luminosity ($L_{\text{cold}}/L_{\text{TIR}}$), and (e) the warm dust to the cold dust luminosity ($L_{\text{warm}}/L_{\text{cold}}$) plotted against R , and the ratios of (b) $L_{\text{warm}}/L_{\text{TIR}}$, (d) $L_{\text{cold}}/L_{\text{TIR}}$, and (f) $L_{\text{warm}}/L_{\text{cold}}$ plotted against L_{TIR} . The symbols are the same as those in figure 8. The line fitted to the data points is shown in each panel.

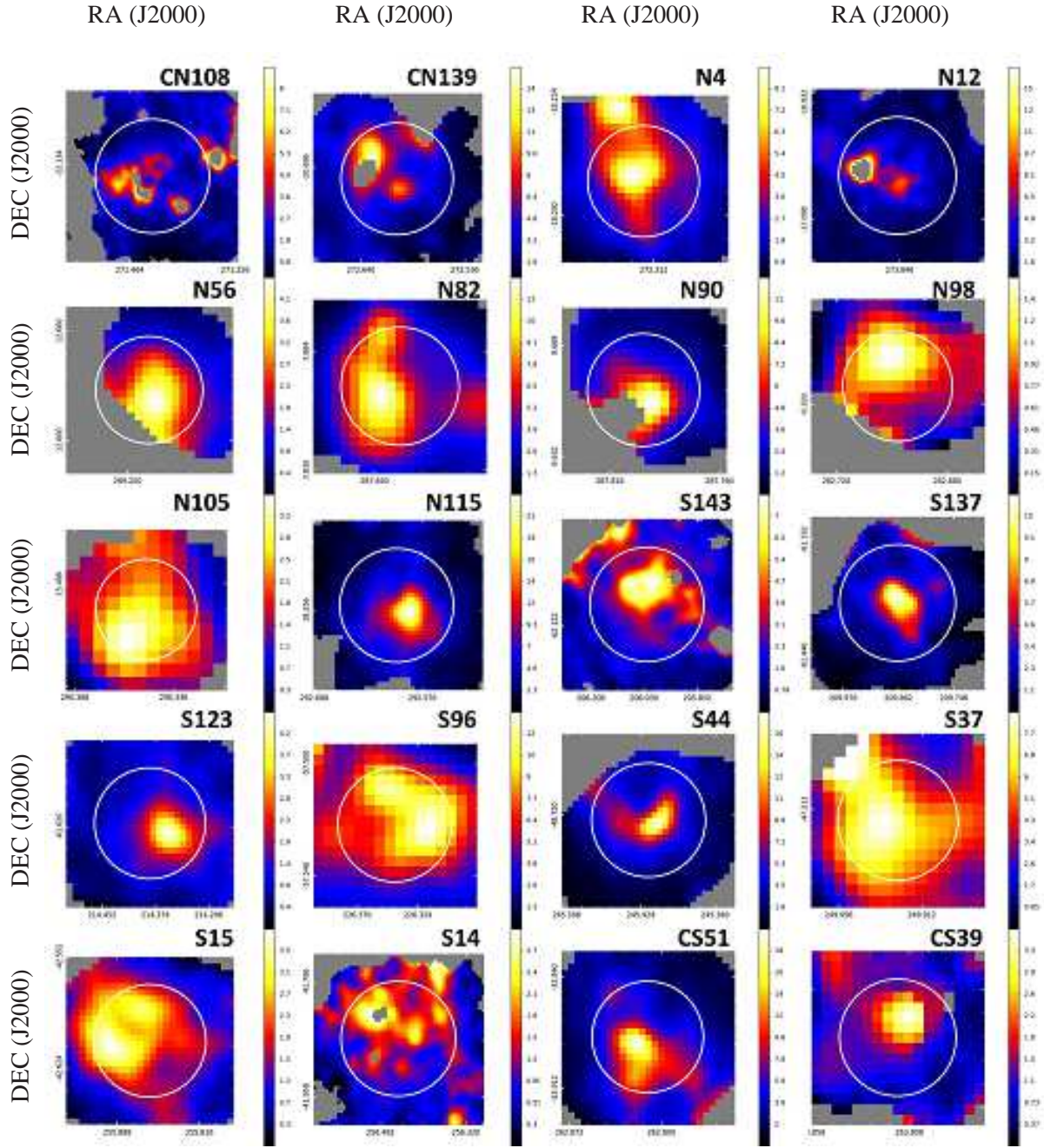


Fig. 13. Same as figure 9, but $I_{\text{warm}}/I_{\text{cold}}$ ratio maps for the closed bubbles. The color levels are given individually.

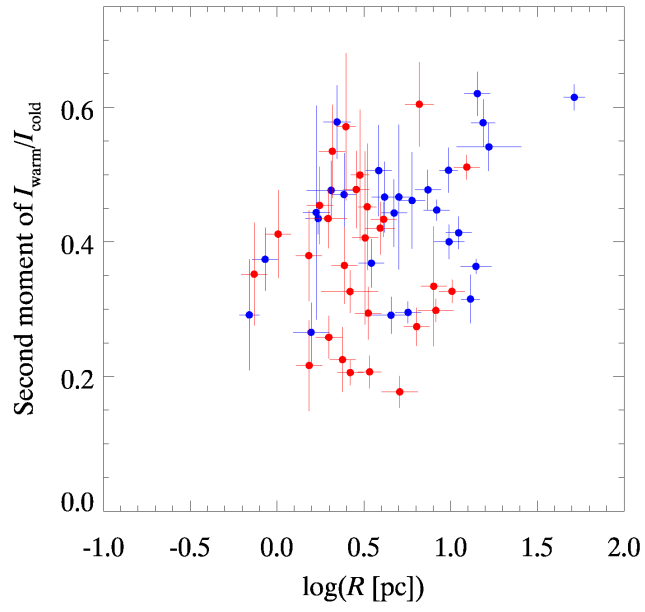


Fig. 15. Second moment of the $I_{\text{warm}}/I_{\text{cold}}$ distribution with respect to the center for the Galactic IR bubbles with the angular radii larger than $90''$. The symbols are the same as those in figure 5.

4 Discussion

Throughout the previous section, we show an overall similarity in the IR properties between the closed and broken bubbles. In particular, both types show a tight correlation of $L_{\text{TIR}} \propto R^3$ as expected from the conventional picture of the Strömgren sphere. The fractional luminosity of PAH emission ($L_{\text{PAH}}/L_{\text{TIR}}$) in the shells is relatively constant at ~ 0.1 , a value typical of star-forming regions (e.g., Smith et al. 2007; Kaneda et al. 2013). The color temperature of the dust emission peaks near the bubble centers, which reflects the presence of heating sources (i.e., massive stars) in the centers. Hence, in order to interpret the results for the majority of the Spitzer Galactic IR bubbles, there is no strong reason for considering pictures other than the Strömgren sphere as the origin of the bubbles. However bubbles with relatively large radii tend to exhibit some differences between the closed and broken types; the large broken bubbles show relatively high L_{TIR} (figure 7), low $I_{\text{PAH}}/I_{\text{TIR}}$ (figure 11) and large $I_{\text{warm}}/I_{\text{cold}}$ peak offsets (figure 15). We below discuss the implications of the differences for a massive star formation scenario.

The low $I_{\text{PAH}}/I_{\text{TIR}}$ and the large $I_{\text{warm}}/I_{\text{cold}}$ peak offsets can be explained by the formation of massive young stars at the edges of bubbles as a consequence of triggered star-formation such as “globule squeezing” and “collect and collapse” (e.g., Deharveng et al. 2010; Zavagno et al. 2010; Dirienzo et al. 2012; Anderson et al. 2015). Such second-generation massive young stars emit intense UV photons from inside the bubble shells, which may cause efficient destruction of PAHs in the shells. They will also contribute to increasing the total IR luminosities. However the enlargement of R may be difficult to be explained by triggered star-formation, because HII regions created by the second-generation young stars cannot substantially expand the original bubble structures. It may also be difficult to explain the systematic differences between broken and closed bubbles.

On the other hand, according to the “cloud-cloud collision” scenario, their bubble structures may be formed by parental clouds deformed as a result of collision, which will cause the relative increase in R . Broken bubble structures will be favorably observed, unless a head-on collision between clouds is viewed face-on. Their high L_{TIR} may suggest the efficient formation of massive stars through the collision process. The relative decrease in $I_{\text{PAH}}/I_{\text{TIR}}$ and the offset of heating sources can be explained by formation of massive stars on the boundary of the collided clouds.

Nonetheless we cannot distinguish the massive star-formation scenarios based on the AKARI results alone. For further discussions, we need additional observational data of the molecular clouds, ionizing gases and young star clusters associated with the bubbles. Our AKARI results, particularly on the large broken bubbles, will provide important observational clues to revealing the origin of the massive star-formation associated with the bubbles.

5 Summary

We have investigated the mid- and far-IR properties of the Spitzer Galactic IR bubbles using the AKARI all-sky survey data at wavelengths of 9, 18, 65, 90, 140 and 160 μm . For the 180 bubbles with known distances, we categorized them into 74 closed, 49 broken and 57 unclassified bubbles with our data analysis method. We obtained the spatial distributions and IR luminosities of the PAH, warm and cold dust components by decomposing AKARI 6-band local SEDs. As a result, the 180 sample bubbles show a wide range of the total IR luminosities corresponding to the bolometric luminosities of a single B-type star to many O-type stars. They exhibit a tight correlation between the radius and the total IR luminosity, following a power-law relation with an index of ~ 3 as expected from the conventional picture of the Strömgren sphere. Their fractional luminosities of the PAH emission decrease with the total IR luminosity, which is interpreted by selective destruction of PAHs exposed to the intense UV radiation. We also investigated other relations between the radius, luminosities and luminosity ratios, and found that there are overall similarities among the bubbles regardless of their morphological types. The exceptions are large broken bubbles; they indicate larger radii, higher total IR luminosities, lower fractional luminosities of the PAH emission, and dust heating sources located nearer to the shells. One possibility to explain the different properties is the “cloud-cloud collision” scenario for massive star-formation. Their bubble structures may have been formed by collided clouds, which caused the relative increase in the radius and total IR luminosity, PAH destruction, and formation of stars on the collision boundary.

Acknowledgments

This research is based on observations with AKARI, a JAXA project with the participation of ESA. The authors thank all the members of the AKARI project, particularly the all-sky survey data reduction team. This research has made use of the NASA/IPAC Infrared Science Archive, which is operated by the Jet Propulsion Laboratory, California Institute of Technology, under contract with the National Aeronautics and Space Administration. This research was supported by JSPS KAKENHI Grant Number 25247020.

References

- Anderson, L. D., et al. 2015, *ApJ*, 800, 101
- Beaumont, C. N., & Williams, J. P. 2010, *ApJ*, 709, 791
- Bendo, G. J., et al. 2008, *MNRAS*, 389, 629
- Benjamin, R. A., et al. 2003, *PASP*, 115, 953
- Cappa, C. E., Firpo, V., Romero, G. A., Rubio, M., & Vasquez, J. 2014, *RevMexAA*, vol. 27, Vol. 44, *RevMexAACS*, 15–15
- Churchwell, E., et al. 2006, *ApJ*, 649, 759
- Churchwell, E., et al. 2007, *ApJ*, 670, 428
- Deharveng, L., Zavagno, A., Schuller, F., Caplan, J., Pomarès, M., & De Breuck, C. 2009, *A&A*, 496, 177
- Deharveng, L., et al. 2010, *A&A*, 523, A6
- Dewangan, L. K., Ojha, D. K., Grave, J. M. C., & Mallick, K. K. 2015, *MNRAS*, 446, 2640
- Dirienzo, W. J., Indebetouw, R., Brogan, C., Cyganowski, C. J., Churchwell, E., & Friesen, R. K. 2012, *AJ*, 144, 173
- Doi, Y., et al. 2015, *PASJ*, 67, 50
- Draine, B. T., & Li, A. 2007, *ApJ*, 657, 810
- Elmegreen, B. G. 1998, *ASPCS*, Vol. 148, *Origins*, ed. C. E. Woodward, J. M. Shull, & H. A. Thronson, Jr., 150
- Fukui, Y., et al. 2014, *ApJ*, 780, 36
- Furukawa, N., Dawson, J. R., Ohama, A., Kawamura, A., Mizuno, N., Onishi, T., & Fukui, Y. 2009, *ApJL*, 696, L115
- Gennaro, M., et al. 2012, *A&A*, 542, A74
- Habe, A., & Ohta, K. 1992, *PASJ*, 44, 203
- Helfand, D. J., Becker, R. H., White, R. L., Fallon, A., & Tuttle, S. 2006, *AJ*, 131, 2525
- Hosokawa, T., & Inutsuka, S.-i. 2005, *ApJ*, 623, 917
- Hosokawa, T., & Inutsuka, S.-i. 2006, *ApJ*, 646, 240
- Hou, L. G., & Gao, X. Y. 2014, *MNRAS*, 438, 426
- Ishihara, D., et al. 2007, *PASJ*, 59, 443
- Kaneda, H., et al. 2013, *A&A*, 556, A92
- Loren, R. B. 1976, *ApJ*, 209, 466
- Martins, F., Schaerer, D., & Hillier, D. J. 2005, *A&A*, 436, 1049
- Murakami, H., et al. 2007, *PASJ*, 59, 369
- Ohama, A., et al. 2010, *ApJ*, 709, 975
- Onaka, T., et al. 2007, *PASJ*, 59, 401

- Osterbrock, D. E. 1989, *Astrophysics of gaseous nebulae and active galactic nuclei*
- Pavel, M. D., & Clemens, D. P. 2012, *ApJ*, 760, 150
- Rahman, M., & Murray, N. 2010, *ApJ*, 719, 1104
- Rodríguez-Esnard, T., Trinidad, M. A., & Migenes, V. 2012, *ApJ*, 761, 158
- Roman-Duval, J., Jackson, J. M., Heyer, M., Johnson, A., Rathborne, J., Shah, R., & Simon, R. 2009, *ApJ*, 699, 1153
- Schuller, F., et al. 2009, *A&A*, 504, 415
- Smith, J. D. T., et al. 2007, *ApJ*, 656, 770
- Stahler, S. W., Shu, F. H., & Taam, R. E. 1980, *ApJ*, 241, 637
- Stil, J. M., et al. 2006, *AJ*, 132, 1158
- Strömgren, B. 1939, *ApJ*, 89, 526
- Suzuki, T., Kaneda, H., & Onaka, T. 2013, *A&A*, 554, A8
- Takahira, K., Tasker, E. J., & Habe, A. 2014, *ApJ*, 792, 63
- Takita, S., et al. 2015, *PASJ*, 67, 51
- Tielens, A. G. G. M. 2008, *ARA&A*, 46, 289
- Torii, K., et al. 2011, *ApJ*, 738, 46
- Torii, K., et al. 2015, *ApJ*, 806, 7
- Watson, C., Corn, T., Churchwell, E. B., Babler, B. L., Povich, M. S., Meade, M. R., & Whitney, B. A. 2009, *ApJ*, 694, 546
- Watson, C., Hanspal, U., & Mengistu, A. 2010, *ApJ*, 716, 1478
- Werner, M. W., et al. 2004, *ApJS*, 154, 1
- Wolfire, M. G., & Cassinelli, J. P. 1987, *ApJ*, 319, 850
- Zavagno, A., et al. 2010, *A&A*, 518, L81
- Zhang, C.-P., Wang, J.-J., & Xu, J.-L. 2013, *A&A*, 550, A117